

**MICROSTRUCTURE AND MECHANICAL  
PROPERTIES OF Al-Si ALLOY PROCESSED BY  
MULTI-DIRECTIONAL FORGING**

**Thesis**

Submitted in partial fulfilment of the requirements for the degree of

**DOCTOR OF PHILOSOPHY**

by

**KUMARA B.**

**(Registration Number: 177031MT006)**



**DEPARTMENT OF METALLURGICAL AND MATERIALS  
ENGINEERING**

**NATIONAL INSTITUTE OF TECHNOLOGY KARNATAKA**

**SURATHKAL, MANGALORE-575025**

**December - 2023**

**MICROSTRUCTURE AND MECHANICAL  
PROPERTIES OF Al-Si ALLOY PROCESSED BY  
MULTI-DIRECTIONAL FORGING**

**Thesis**

Submitted in partial fulfilment of the requirements for the degree of

**DOCTOR OF PHILOSOPHY**

by

**KUMARA B.**

**(Registration Number: 177031MT006)**

**Under the Guidance of**

**Dr. PREETHAM KUMAR G. V.**

**Associate Professor**



**DEPARTMENT OF METALLURGICAL AND MATERIALS  
ENGINEERING  
NATIONAL INSTITUTE OF TECHNOLOGY KARNATAKA  
SURATHKAL, MANGALORE-575025**

**December - 2023**

## DECLARATION

*By the Ph.D. Research scholar*

I hereby declare that the Research Thesis entitled “**Microstructure and Mechanical Properties of Al-Si Alloy Processed by Multi-Directional Forging**” which is being submitted to the **National Institute of Technology Karnataka, Surathkal** in partial fulfilment of the requirements for the award of the Degree of **Doctor of Philosophy in Department of Metallurgical and Materials Engineering** is a bonafide report of the research work carried out by me. The material contained in this Research Thesis has not been submitted to any University or Institution for the award of any degree.

  
KUMARA B

Reg. No. 177031MT006

Department of Metallurgical and Materials Engineering

**Place: NITK-Surathkal, Mangalore**

**Date:** 20-12-2023

## CERTIFICATE

This is to certify that the Research Thesis entitled “**Microstructure and Mechanical Properties of Al-Si Alloy Processed by Multi-Directional Forging**” submitted by **Mr. KUMARA B. (Register Number: 177031MT006)** as the record of the research work carried out by him, is *accepted as the Research Thesis submission* in partial fulfilment of the requirements for the award of degree of **Doctor of Philosophy**.



Research Guide

**Dr. Preetham Kumar G V**

Associate Professor

Department of Metallurgical and Materials Engineering

NITK Surathkal, Mangalore



**Chairman-DRPC**

Department of Metallurgical and Materials Engineering

NITK Surathkal, Mangalore

**Chairman - DRPC**  
**Dept. of Metallurgical and Materials Engineering**  
**National Institute of Technology Karnataka, Surathkal**  
**Post Srinivasnagar, Mangaluru - 575 025**  
**Karnataka, India**

## **ACKNOWLEDGEMENT**

The research work, which is presented in this dissertation, is more of teamwork and I would like to thank many who have contributed their time and energy to the study.

First and foremost, I am grateful to my advisor Dr. Preetham Kumar G.V., Associate Professor, Department of Metallurgical and Materials Engineering, National Institute of Technology Karnataka, Surathkal (NITK) as he consistently kept me motivated and instilled good thoughts not only for research but for life as well. His constant and enthusiastic support throughout is the root cause for the research work to see its logical end.

I am also grateful to my research program assessment committee member Dr. Kumkum Banerjee, Associate Professor, Department of Metallurgical and Materials Engineering, NITK, Surathkal, and Dr. Sharnappa Joladarashi, Associate Professor, Department of Mechanical Engineering, NITK, Surathkal for their unbiased appreciation, support, and suggestions provided during the various discussions, which has certainly helped in the betterment of this research work.

I am thankful to Dr. Ravishankar K. S., Head & DRPC Chairman, Department of Metallurgical and Materials Engineering, NITK, Surathkal.

I express my sincere thanks to Dr. K Narayana Prabhu, Professor, Department of Metallurgical and Materials Engineering, NITK, Surathkal, and Dr. Ramesh M R, Associate Professor, Department of Mechanical Engineering, NITK, Surathkal for providing me the necessary facilities in the department.

I am thankful to get constant encouragement and support from all the Teaching staff of the Department of Metallurgical and Materials Engineering, NITK, Surathkal, during the entire research work. I would like to express my sincere thanks and gratitude to Applied Mechanics Department staff for their kind help, encouragement for the successful completion of this research work.

I specially thank to our technical staff Mr. Dinesha, Mr. Sathish, and Mr. Yashwanth. I extend my gratitude to Mrs. Sharmila Dinesh for helping with necessary documentation for journal papers and thesis. I also thank to our office staff Mrs. Vinaya Shettigar, Mr.

Sundara Shettigar, and Mr. Lokesh Naik for their kind support related to research work in the department.

A special thanks to my family. Words cannot express how grateful I am to my parents for all the sacrifices they made on my behalf. Their wishes gave me the endurance to sustain this far. I also acknowledge my relatives and well-wishers for their wholehearted encouragement and support.

Finally, I thank all those who directly or indirectly helped me to complete the research work.

**KUMARA B**

## ABSTRACT

In this present work, the effect of multi-directional room temperature forging on the mechanical and wear characteristics of Al-7.3Si and Al-12.1Si alloys with varying cumulative strains was investigated. Severe plastic deformation via multidirectional forging technique can be used to modify the mechanical properties. MDF can be applied to a relatively large sample that can be used for industrial applications. In the MDF process, strain per pass can be controlled by maintaining the height-to-width ratio, and thus, a wide range of metals and alloys can be deformed at room temperature. The Al-Si alloy ingots were melted in a furnace and then poured into a preheated metallic die to produce a cast sample of desired shape and dimension. Al-7.3Si alloys were machined to dimensions of 30 mm x 30 mm x 24 mm for MDF processing with an equivalent strain of 0.22. Similarly, Al-12.1Si alloys were machined to dimensions of 30 mm x 30 mm x 23 mm for MDF processing with an equivalent strain of 0.27. The machined samples were then subjected to solution heat treatment before being forged in order to change the morphology of shape-edged eutectic silicon of the as-cast sample. MDF successfully processed the Al-7.3Si and Al-12.1Si alloys for two and three cycles, respectively, with cumulative strains of 1.3 and 2.43 at room temperature. Optical microscopy, field emission scanning electron microscopy, and X-ray diffractometer were used to characterise the effect of MDF processing on Al-7.3Si and Al-12.1Si alloys. Microstructural observations showed that the coarse eutectic silicon particles were effectively broken into finer particles and uniformly redistributed. With increasing MDF cycles, the silicon particles fragmented into finer particles. According to XRD results, the peak broadening in the XRD pattern of MDF-processed sample is due to the combined effect of crystallite size and micro-strain. The hardness and tensile strength of MDF samples have significantly increased. The hardness and tensile strength of the as-cast Al-7.3Si alloy increased to 60% and 149%, respectively, after two cycles of MDF. Similarly, the hardness and tensile strength of the as-cast Al-12.1Si alloy increased to 50% and 98%, respectively, after three cycles. Scratch test was conducted to measure the scratch resistance of unprocessed and MDF-processed samples. Tests were performed at ambient temperature under a progressive load of 2–15 N over a 5 mm scratch distance at a speed of 1 mm/min. Dry sliding wear tests were

performed on a tribometer (pin-on-disc) under varying sliding speeds and loads at ambient temperatures. MDF-processed materials exhibited better scratch and wear resistance compared to as-cast materials. Furthermore, scratch and wear resistance increased with an increasing number of MDF cycles. Al-7.3Si alloy with two cycles and Al-12.1Si alloy with two and three cycles have shown maximum wear and scratch resistance. After MDF process, the wear mechanisms in both alloys shifted from adhesive and delamination wear to a combination of abrasive and a lesser amount of adhesion wear. Moreover, the degree of delamination significantly decreased after MDF process. Improvements in the mechanical and wear properties of MDF-processed samples can be attributed to the refinement and uniform distribution of eutectic silicon particles, as well as strain hardening of the aluminium phase.

Keywords: Al-Si alloys, Solution heat treatment, MDF, Microstructure, Mechanical properties, wear properties.

<b>CONTENTS</b>		<b>Page No.</b>
<b>ACKNOWLEDGEMENT</b>		<b>i</b>
<b>ABSTRACT</b>		<b>iii</b>
<b>CONTENTS</b>		<b>v</b>
<b>LIST OF FIGURES</b>		<b>ix</b>
<b>LIST OF TABLES</b>		<b>xv</b>
<b>NOMENCLATURE</b>		<b>xvii</b>
<b>CHAPTER 1: INTRODUCTION</b>		<b>1-5</b>
<b>CHAPTER 2: REVIEW OF LITERATURE</b>		<b>7-45</b>
2.1	Severe plastic deformation	7
2.2	Principles of Multi-Directional Forging	8
2.3	Process parameters of MDF process	9
2.3.1	Strain Imposed	9
2.3.2	Strain rate	10
2.3.3	Pressing temperature	10
2.3.4	Friction and lubrication	10
2.4	Merits and demerits of MDF	11
2.4.1	Merits	11
2.4.2	Demerits	11
2.5	Aluminium-Silicon Alloys	11
2.5.1	Hypoeutectic Al-Si alloys	13
2.5.2	Eutectic Al-Si alloys	14
2.5.3	Hypereutectic Al-Si alloys	14
2.6	Solution heat treatment	14
2.7	Influence of SPD on mechanical and microstructure properties of Al-Si alloy	15
2.8	Wear and wear mechanisms	32
2.8.1	Adhesive Wear	33
2.8.2	Abrasive Wear	34
2.8.3	Erosive wear	35
2.8.4	Fretting	36

	2.8.5 Corrosive and oxidation wear	36
	2.9 Wear study of SPD-processed Al-Si materials	37
	2.10 Summary of Literature Review	43
	2.11 Objectives of present work	44
<b>CHAPTER 3:</b>	<b>EXPERIMENTAL PROCEDURES</b>	<b>47-57</b>
	3.1 Materials	47
	3.2 Preparation of cast sample for MDF	48
	3.3 Multidirectional forging	49
	3.4 Material characterization	52
	3.4.1 Optical Microscopy	52
	3.4.2 Field emission scanning electron microscopy	52
	3.4.3 X-Ray Diffractometry	52
	3.5 Mechanical characteristic	52
	3.5.1 Microhardness measurement	52
	3.5.2 Tensile Testing	53
	3.5.3 Compression Testing	53
	3.5.4 Scratch Testing	54
	3.5.5 Wear testing	56
<b>CHAPTER 4:</b>	<b>RESULTS</b>	<b>59-106</b>
	4.1 Microstructural characterization	59
	4.1.1 Al-7.3Si alloys	59
	4.1.2 Al-12.1Si alloys	61
	4.2 X-ray diffraction analysis	70
	4.3 Mechanical Properties	73
	4.3.1 Microhardness	73
	4.3.2 Tensile properties	75
	4.3.3 Tensile-tested fracture surface	78
	4.3.4 Flow properties	83
	4.3.5 Scratch Testing	86
	4.4 Wear properties	92

	4.4.1	Wear mass loss	92
	4.4.2	Wear mechanisms	98
<b>CHAPTER 5:</b>	<b>DISCUSSION</b>		<b>107-112</b>
<b>CHAPTER 6:</b>	<b>CONCLUSIONS AND SCOPE OF FUTURE WORK</b>		<b>113-116</b>
	6.1	Conclusions	113
	6.2	Scope for the future work	116
	<b>LIST OF PUBLICATIONS</b>		<b>117</b>
	<b>REFERENCES</b>		<b>119</b>
<b>APPENDIX I:</b>	Multi-directional die design		131
<b>APPENDIX II:</b>	Casting Die Design		135
<b>APPENDIX III</b>	Microstructure of ingot and as-cast Al-7.3Si alloys		139
	Microstructure of ingot and as-cast Al-12.1Si alloys		138
<b>APPENDIX IV</b>	Mechanical property tables		141
<b>BIO-DATA</b>			147



## LIST OF FIGURES

<b>Fig. No.</b>	<b>Figure Caption</b>	<b>Page No.</b>
2.1	Schematic representation of MDF processing	8
2.2	MDF processing of the sample in top view	9
2.3	The binary Al-Si alloy phase diagram	12
2.4	Illustration of Abrasive adhesive wear mechanism	33
2.5	(a) Two-body abrasive wear; (b) Three-body abrasive wear	34
2.6	Illustration of Abrasive wear modes (a) ploughing mode (b) wedge forming mode (C) cutting mode	35
3.1	Photograph of Al-Si alloy ingot	47
3.2	Casting die with cast sample	48
3.3	Al-7.3Si and Al-12.1Si samples for MDF Processing	48
3.4	Three-dimensional schematic view of the MDF die	50
3.5	MDF die assembly	50
3.6	Hydraulic press with MDF set up	51
3.7	Fractured Al-7.3Si and Al-12.1Si alloys after seven and eleven passes through MDF at room temperature	51
3.8	Schematic diagram of the tensile test sample (Note: All dimensions are in mm)	53
3.9	Schematic diagram of the compression test sample (Note: All dimensions are in mm)	54
3.10	Schematic diagram of three scratch modes: (a) constant load, (b) progressive load, and (c) incremental load	55
3.11	a) photograph of scratch testing machine; (b) scratch testing machine with sample set up.	55
3.12	Photograph of pin on disc wear testing machine	57
4.1	Optical micrograph of Al-7.3Si samples: (a, b) as-cast; (c, d) solutionized	59

4.2	Optical micrograph of Al-7.3Si samples: (a, b) one cycle of MDF; (c, d) two cycles of MDF	60
4.3	Optical micrograph of Al-12Si alloys: (a, b) as-cast; (c, d) solutionized	61
4.4	Optical micrograph of Al-7.3Si samples: (a, b) one cycle of MDF; (c, d) two cycles of MDF	62
4.5	Optical micrograph of Al-12Si alloys: (a, b) after three cycles of MDF	63
4.6	FESEM micrograph of MDF processed Al-7.3Si with two cycles and Al-12.1Si alloy with three cycles of MDF.	63
4.7	Average silicon particle size of Al-7.3Si alloy under the different processing conditions	65
4.8	Average silicon particle size of Al-12.1Si alloy under the different processing conditions	65
4.9	Average number of Si particles of Al-7.3Si alloy under the different processing conditions	66
4.10	Average number of Si particles of Al-12.1Si alloy under the different processing conditions	66
4.11	SEM image and EDX of solutionized Al-7.3Si alloy	67
4.12	SEM image and EDX of solutionized Al-12.1Si alloy	67
4.13	Elemental mapping of two cycles of MDF processed Al-7.3Si alloy: a) SEM image; b) Al; c) Si; d) Mg; e) Fe; f) weight and atomic percentage of various elements	68
4.14	Elemental mapping of three cycles of MDF processed Al-12.1Si alloy: a) SEM image; b) Al; c) Si; d) Mg; e) Fe; f) Weight and atomic percentage of various elements	68
4.15	XRD patterns of Al-7.3Si alloy: (a) as-cast; (b) solutionized; (c) one cycle; and (d) two cycles	71
4.16	XRD patterns of Al-12Si alloy: (a) as-cast, (b) solutionized, (c) one cycle (d) two cycles (e)three cycles	72

4.17	Micro-hardness of the as-cast, solutionized and MDF-processed Al-7.3Si samples	74
4.18	Micro-hardness of the as-cast, solutionized and MDF-processed Al-12.1Si samples	74
4.19	Stress-strain curves of as-cast, solutionized, and MDF-processed Al-7.3Si alloy specimens	76
4.20	Strength-elongation bar chart of Al-7.3Si alloy in different processing conditions	76
4.21	Stress-strain curves of as-cast, solutionized, and MDF-processed Al-12.1Si alloy specimens	77
4.22	Strength-elongation bar chart of Al-12.1Si alloy in different processing conditions	77
4.23	SEM micrographs of the fracture surface of Al-7.3Si alloy: (a) as-cast, (b) solutionized	78
4.24	SEM micrographs of the fracture surface of Al-12.1Si alloy: (a) as-cast, (b) solutionized	79
4.25	SEM micrographs of the fracture surface of Al-7.3Si alloys: (a) one cycle; (b) two cycles	79
4.26	SEM micrographs of the fracture surface of Al-12.1Si alloys: (a) one cycle; (b) two cycles	79
4.27	SEM micrographs of the fracture surface of Al-12.1Si alloy with three-cycle	80
4.28	Compression true stress-strain graph of as-cast, solutionized, and MDF-processed Al-7.3Si alloy	84
4.29	Strength coefficient and strain hardening exponent of as-cast, solutionized, and MDF-processed Al-7.3Si alloys	84
4.30	Compression true stress-strain graph of as-cast, solutionized, and MDF-processed Al-12.1Si alloy	85
4.31	Strength coefficient and strain hardening exponent of as-cast, solutionized, and MDF-processed Al-12.1Si alloy	85

4.32	Scratch images of Al-7.3Si alloy in various processing conditions under progressive load scratch test (2–15 N)	86
4.33	Variation in scratch depth of Al-7.3Si alloy in various processing conditions under progressive load scratch test (2–15 N)	87
4.34	Scratch images of Al-12.1Si alloy in various processing conditions under progressive load scratch test (2–15 N)	87
4.35	Variation in scratch depth of Al-12.1Si alloy in various processing conditions under progressive load scratch test (2–15 N)	88
4.36	Traction force of Al-7.3Si alloy in various processing conditions under progressive load scratch test (2–15 N)	89
4.37	Traction force of Al-12.1Si alloy in various processing conditions under progressive load scratch test (2–15 N)	90
4.38	Coefficient of friction of Al-7.3Si alloy in various processing conditions under progressive load scratch test (2–15 N)	91
4.39	Coefficient of friction of Al-12Si alloy in various processing conditions under progressive load scratch test (2–15 N)	91
4.40	Wear mass loss of Al-7.3Si alloy under varying applied loads (19.61 N and 39.23 N) and a sliding velocity of 0.7 m/s	93
4.41	Wear mass loss of Al-12.1Si alloy under varying applied loads (19.61 N and 39.23 N) and a sliding velocity of 0.7 m/s	93
4.42	Wear mass loss of Al-7.3Si alloy under varying applied loads (19.61 N and 39.23 N) and a sliding velocity of 2.2 m/s	94
4.43	Wear mass loss of Al-12.1Si alloy under varying applied loads (19.61 N and 39.23 N) and a sliding velocity of 2.2 m/s	94
4.44	Coefficient of friction of Al-7.3Si alloy under varying applied loads (19.61 N and 39.23 N) and a sliding velocity of 0.7 m/s	96
4.45	Coefficient of friction of Al-12.1Si alloy under varying applied loads (19.61 N and 39.23 N) and a sliding velocity of 0.7 m/s	96
4.46	Coefficient of friction of Al-7.3Si alloy under varying applied loads (19.61 N and 39.23 N) and a sliding velocity of 2.2 m/s	97

4.47	Coefficient of friction of Al-12.1Si alloy under varying applied loads (19.61 N and 39.23 N) and a sliding velocity of 2.2 m/s	97
4.48	FE-SEM image of the worn surfaces of Al-7.3Si alloy under a load of 19.61 N and at a speed of 0.7 m/s: (a) cast, (b) one cycle, and (c) two cycles	98
4.49	FE-SEM image of the worn surfaces of Al-7.3Si alloy under a load of 39.23 N and at a speed of 0.7 m/s: (a) as-cast, (b) one cycle, and (c) two cycles	99
4.50	FE-SEM image of the worn surfaces of Al-7.3Si alloy under a load of 19.61 N and at a speed of 2.2 m/s: (a) cast, (b) one cycle, and (c) two cycles	100
4.51	FE-SEM image of the worn surfaces of Al-7.3Si alloy under a load of 39.23 N and at a speed of 2.2 m/s: (a) cast, (b) one cycle, and (c) two cycles	100
4.52	FE-SEM image of the worn surfaces of Al-12.1Si alloy under a load of 19.61 N and at a speed of 0.7 m/s: (a) cast, (b) one cycle, (c) two cycles, and three cycles	101
4.53	FE-SEM image of the worn surfaces of Al-12.1Si alloy under a load of 39.23 N and at a speed of 0.7 m/s: (a) cast, (b) one cycle, (c) two cycles, and three cycles	102
4.54	FE-SEM image of the worn surfaces of Al-12.1Si alloy under a load of 19.61 N and at a speed of 2.2 m/s: (a) cast, (b) one cycle, (c) two cycles, and three cycles.	103
4.55	FE-SEM image of the worn surfaces of Al-12.1Si alloy under a load of 39.23 N and at a speed of 2.2 m/s: (a) cast, (b) one cycle, (c) two cycles, and three cycles.	103
4.56	EDS analysis of the worn surfaces of three cycles of Al-7.3Si alloy at a speed of 0.7 m/s: a) Under 19.61 N load; b) Under 39.23 N load	104
4.57	EDS analysis of the worn surfaces of three cycles of Al-7.3Si alloy at a speed of 2.2 m/s: a) Under 19.61 N load; b) Under 39.23 N load	105

4.58	EDS analysis of the worn surfaces of three cycles of Al-12.1Si alloy at a speed of 2.2 m/s: a) Under 19.61 N load; b) Under 39.23 N load	105
4.59	EDS analysis of the worn surfaces of three cycles of Al-12.1Si alloy at a speed of 0.7 m/s: a) Under 19.61 N load; b) Under 39.23 N load	106
A1-1	Two-dimensional diagram of MDF base plate die in different views	130
A1-2	Two-dimensional diagram of MDF Plunger in all different views	131
A1-3	Two-dimensional diagram of MDF split sections (part 1) in different views	132
A1-4	Two-dimensional diagram of MDF split sections(part-2) in different views	133
A2-1	Two-dimensional diagram of Casting die split sections(part 1) in different views	134
A2-2	Two-dimensional diagram of Casting die split sections(part 2) in different views	135
A2-3	Schematic three-dimensional representation of the casting die	136
A3-1	Optical micrograph of Al-7.3Si samples (a, b) Ingot; (c, d) as-cast	137
A3-2	Optical micrograph of Al-12.1Si samples (a, b) Ingot; (c, d) as-cast	138

## LIST OF TABLES

<b>Table No.</b>	<b>Table Caption</b>	<b>Page No.</b>
2.1	Overview of SPD on mechanical and microstructure properties of Al-Si alloy.	24
2.2	Overview of SPD on mechanical and microstructure properties of Al-Si alloy.	40
3.1	Chemical composition of Al-7.3Si and Al-12.1Si alloys.	47
3.2	Wear test conditions	57
4.1	Summary of Silicon particle size of Al-7.3Si alloys in various conditions	69
4.2	Summary of Silicon particle size of Al-12.1Si alloys in various conditions	69
4.3	Microstructural parameters of the Al-7.3Si samples calculated from XRD patterns via Williamson-Hall method.	73
4.4	Microstructural parameters of the Al-12.1Si samples calculated from XRD patterns via Williamson-Hall method	73
4.5	Influence of various SPD on mechanical characteristics of Al-7.3Si alloys	81
4.6	Influence of various SPD on mechanical characteristics of Al-12.1Si alloys	82
A4-1	Summary of hardness and tensile strength of Al-7.3Si alloys in various conditions	138
A4-2	Summary of hardness and tensile strength of Al-12.1Si alloys in various conditions	138
A4-3	Summary of strength coefficient and strain hardening exponent of Al-7.3Si alloys in various conditions	139
A4-4	Summary of strength coefficient and strain hardening exponent of Al-12.1Si alloys in various conditions	139
A4-5	Summary of scratch depth of Al-7.3Si alloys in various conditions	139
A4-6	Summary of scratch depth of Al-7.3Si alloys in various conditions	140

A4-7	Summary of scratch traction force of Al-7.3Si alloys in various conditions	140
A4-8	Summary of scratch traction force of Al-12.1Si alloys in various conditions	140
A4-9	Summary of wear mass loss of Al-7.3Si alloys in various conditions	141
A4-10	Summary of wear mass loss of Al-12.1Si alloys in various conditions	141
A4-11	Summary of COF of Al-7.3Si alloys in various conditions	142
A4-12	Summary of COF of Al-12.1Si alloys in various conditions	142

## NOMENCLATURE

UFG	Ultrafine Grains
CG	Coarse Grains
SPD	Severe Plastic Deformation
MDF	Multi-Directional Forging
HPT	High-Pressure Torsion
ARB	Accumulative Roll Bonding
ECAP	Equal-channel angular pressing
ECAE	Equal-channel angular extrusion
RD-ECAP	Rotary-die equal-channel angular pressing
FSP	Friction stir processing
Al-Si	Aluminium-Silicon
RT	Room Temperature
OM	Optical Microscopy
SEM	Scanning Electron Microscopy
FESEM	Field emission scanning electron microscopy
EDS	Energy Dispersive Spectroscopy
XRD	X-Ray Diffraction
UTS	Ultimate tensile strength
UTM	Universal testing machine
Sr	Strontium
Na	Sodium
Al	Aluminium
Si	Silicon
Fe	Iron
Cu	Copper

Mn	Manganese
Mg	Magnesium
Zn	Zinc
Ni	Nickel
Ti	Titanium
Hv	Vickers hardness
μm	Micrometer
nm	Nanometer
SLM	Selective laser melting

## CHAPTER 1

### INTRODUCTION

Aluminium-silicon alloys are extensively employed in automobiles and aeronautical sectors due to their high strength-to-weight ratio, low thermal expansion, high corrosion resistance, and excellent casting characteristics (Haghdadi et al. 2016). These alloys are a good material option for engine parts such as pistons, cylinder blocks, manifolds, valves, and connecting rods (Akbari et al. 2017). Silicon plays a very essential role in increasing the overall wear resistance and strength of aluminium-silicon alloys due to their higher hardness. However, the microstructures of as-cast aluminium-silicon alloy play a major role in their service performance (Kori & Chandrashekharaiah 2007). The microstructures of as-cast aluminium-silicon alloys consist of aluminium dendrites (Al phase) and networks of large plates or needle-shaped Si particles. Mechanical and wear characteristics of aluminium-silicon alloys are influenced by various defects such as non-uniformly distributed sharp-edged coarse silicon particles, dendritic structure, and porosities (Akbari et al. 2017). The common problem in Al-Si castings is porosity. A pore is a type of stress concentrator that can cause microcrack initiation and propagation and cannot support external loads (Ye 2003). The lack of inter-dendritic feeding and/or the exsolution of dissolved gas from the molten metal are two common causes of microporosity. As the temperature rises, hydrogen becomes more soluble in Al-Si melts. Hydrogen atoms precipitate from the molten metal and turn into molecular hydrogen as the molten Al-Si alloy solidifies. If the Al-Si alloy solidifies more quickly than the molecular hydrogen, the molecular hydrogen escapes from the melt, leading to the formation of porosity. Porosity can reduce the ductility and workability of the alloy. According to Immanuel and Panigrahi (2015), the porosity and sharp-tipped Si particles in the aluminium-silicon alloy are stress risers, which lead to crack initiation.

The form, size, and distribution of silicon and porosities have a greater impact on the wear mechanical characteristic of Al-Si alloys (Alidokht et al. 2012). Also, refinement of eutectic Si together with aluminium phase is the essential step to improving the mechanical properties of this alloy. Heat treatment, some chemical modifiers (Sr and Na), and severe plastic deformation (SPD) can change the distribution state of the silicon particles in the aluminium-silicon alloys (Li et al. 2015 and Ma et al. 2005).

Hence, Al-Si alloys are ideal for examining how silicon particles affect tribological and mechanical characteristics. Modified and refined silicon phases can improve the mechanical characteristics of aluminium silicon alloys and thereby expand their applications. Some traditional procedures, such as altering solidification rates, adding alloying elements, and employing heat treatments, have been utilized to solve or minimise the above-mentioned defects. Traditional techniques have resulted in some improvements in their strength, ductility, and wear properties, but more improvements are required for better applications (Kucukomeroglu 2010). Furthermore, traditional processes could not completely eliminate casting defects such as porosity and inhomogeneous eutectic Si distribution (Mahmoud 2013). Silicon phases of Al-Si alloys can be refined via deformation techniques such as hot rolling and extrusion (Wu et al. 2019; Lin et al. 2019). Deformation process showed more effective refinement of Si particles compared to conventional refinement techniques such as chemical modifiers and heat treatment. However, severe plastic deformation (SPD) is frequently used to refine grains and increase the strength of Al alloys since it demonstrates a substantially higher degree of deformation than traditional plastic deformation (Valiev et al. 2000). SPD-processed Al-Si alloys exhibit better strength than those subjected to traditional rolling (Cheng et al. 2021).

Severe plastic deformation (SPD) processes include the introduction of a large plastic strain into a bulk metal to produce fine-grained metals. SPD belongs to "top-down" method, where a bulk solid with a relatively larger grain size is used to refine into a finer grain size. The "bottom-up" process involves assembling individual atoms or nanoparticulate solids to create bulk materials. Examples of this strategy involve electro-deposition, ball milling followed by consolidation and inert gas condensation. These methods are capable of producing samples with incredibly small grain sizes; however, they have drawbacks due to small size of the products, the possibility of processing contamination (such as from ball milling), and the fact that there is always at least a minimal amount of residual porosity (Valiev and Langdon 2006). The "top-down" method prevents the introduction of contaminants or porosity by employing bulk samples. There are already many potential methods for processing these bulk solids; however, each method depends on the application of heavy strain. The top-down

approach could be accomplished by conventional processing and severe plastic deformation (SPD) techniques. Traditional material processing techniques like cold rolling or drawing cannot subject the material to such high strains without failing. According to Zhilyaev and Langdon (2008), one distinctive aspect of SPD is that the larger strain is applied without significantly altering the overall dimensions of the workpiece. To develop a high plastic strain in the material, the specimen might be processed repeatedly using the same die. According to research by Kavosi et al. (2014), severe plastic deformation (SPD) greatly impacts mechanical characteristics of a wide range of metals and alloys. SPD-processed materials are used in aerospace and automobile sectors due to their better mechanical properties (Ramesh et al. 2019). Severe plastic deformation eliminates porosity in compacted samples and contaminants and can process large-sized workpieces (Valiev et al. 2000).

Severe plastic deformation processed material showed outstanding mechanical characteristics (Singh et al. 2016). SPD techniques are specifically regarded as the primary post-casting approach for obtaining better mechanical characteristics by refining the microstructure in aluminium-silicon alloys (Haghdadi et al. 2016). So far, some unique methods have been used on these kinds of alloys, including SPD. The sample can be processed repeatedly in SPD to impart a very high strain. Some of the important SPD techniques that apply high levels of plastic strain to metals and alloys include High-Pressure torsional (Zhilyaev and Langdon 2008), Multidirectional Forging (Salishchev et al. 1995), Equal Channel Angular Pressing (Valiev and Langdon 2006), and Accumulative Roll Bonding (Saito et al. 1998). Since these procedures subject the materials to extreme plastic deformation, it is usual to refer to all of these procedures as severe plastic deformation (SPD). Among various SPD methods, multidirectional forging can process relatively large samples that can be suitable for industrial use (Aoba et al. 2017). SPD techniques, such as multidirectional forging, involve the plastic deformation of materials under high hydrostatic pressure. During the MDF process, extremely high strains are applied to materials with the minimum distortion from their original shape. As samples can be repeatedly forged in MDF die without changing their cross-sectional dimensions, high strain can be maintained, resulting in impressive grain refinement. In addition, the MDF process is simple and

offers an economical approach for the production of bulk ultrafine-grained materials, which can be easily scaled up for industrial use.

**Thesis organisation** This study looked at the combined effects of solution heat treatment (solutionizing) and multidirectional forging (MDF) on mechanical and microstructure properties of Al-7.3Si and Al-12.1Si alloys at ambient temperature. Microstructural analysis of processed and unprocessed samples is investigated, and outcomes are correlated with the wear and mechanical characteristics. Different chapters are used to present the thesis. Following is a quick chapter-wise summary of the thesis:

**Chapter 1** gives brief introduction of aluminium-silicon alloy, its drawbacks and applications, the background of severe plastic deformation, and its importance in refinement materials have been described.

**Chapter 2** contains summary of many recent investigations on Al-Si alloys that have undergone severe plastic deformation (SPD), with an emphasis on changes in microstructure, mechanical properties, and wear properties. A detailed description of MDF processing and its advantages, principles, and experimental factors that affect the process is given. Objectives of the current research investigation are established using the gaps in the literature review.

**Chapter 3** explains the details of the material, the details of sample preparation, the MDF process setup, and its processing procedure. Details of the characterization techniques and equipment used to analyse the processed samples were described.

**Chapter 4** provides outcomes of solution heat-treated Al-7.3Si and Al-12.1Si alloys followed by MDF-processed at room temperature. Investigation of processed and unprocessed materials is derived from results obtained through microstructural characterization, mechanical testing, and wear testing.

**Chapter 5** describes the detailed analysis and elaborates on the discussion of results obtained to conclude the work. The effect of MDF processing on the microstructure, mechanical, and wear properties was analysed. Also, the effect of different wear parameters on wear properties was discussed.

**Chapter 6** presents the conclusions drawn based on the results obtained in this research work and the future scope of work is also enlisted. The appendix and the list of references are shown at the end of the dissertation.



## **CHAPTER 2**

### **REVIEW OF LITERATURE**

This chapter contains a comprehensive review of literature, with special reference to SPD and the parameters involved in MDF processing. Importance of aluminium-silicon alloys and implications of Si particles on wear and mechanical characteristics have been demonstrated. Effect of various SPDs on wear and mechanical behaviour of aluminium-silicon alloys is discussed to establish basis for present study. At the end of this chapter, the objectives of the current research are drawn based on gaps observed in the available literature after critical analysis.

#### **2.1 Severe plastic deformation**

The primary objective of severe plastic deformation is to create environmentally friendly, high-strength, and lightweight products. In traditional metal forming work, like extrusion, forging, and rolling, the structure is altered for enhanced mechanical properties; however, traditional metal forming produces lower limits of strain, which results in a lower refinement of the grain size. In traditional metal-forming work, the strain is less than two (Azushima et al. 2008). Drawing, rolling, and extrusion can create plastic strain greater than 2.0; however, diameter and thickness become incredibly thin and are not useful for structural work. Numerous SPDs have been built to apply extremely large strain to the bulk metal. To solve some of the limitations of traditional metal work, SPD processing techniques have been developed. According to Lowe and Valiev (2004), SPD has become a potential technique for developing ultrafine-grained materials with attractive characteristics. Materials processed by SPD have significantly greater hardness and good wear resistance. High-pressure torsion, Equal channel angular extrusion, multidirectional forging, twist extrusion, cyclic extrusion and compression, friction stir processing and accumulative roll-bonding are a few examples of SPD processing methods. All metal-forming processes that use the SPD approach can apply very high strains to materials to change their properties. Additionally, the application of a severe plastic deformation process is a potential opportunity for microstructural refinement of materials.

## 2.2 Principles of Multi-Directional Forging

Multidirectional forging is SPD technique that can capable of imparting high strain under compressive mode of deformation. It can be used to develop significant grain refinement in metals. In this technique, a large amount of plain strain is introduced into the material to attain severe plastic deformation, which can be utilised to alter the mechanical properties. Ultra-fined grain structure in bulk material was initially formed using MDF in the 1990s (Salishchev et al. 1995). MDF is a repeating forging process that changes the axis of applied strain in three orthogonal directions at each step. It is simplest and most economical way to achieve higher strains with little deviation from their original shape. As material is repeatedly deformed at room temperature or above, redundant plastic stresses may build up in the material. Since there is hardly any change in shape of the work piece under MDF conditions, many repetitive passes can be undertaken to produce extremely high total strains. Among the various SPDs, MDF is widely employed in industries since it can process relatively large samples (Zhu et al. 2014). However, among various SPD techniques, MDF is simplest to realize as no special tools are needed. Additionally, due to its low-strain compressive mode in comparison to ECAP and HPT processes, MDF can be used for brittle materials at ambient temperature (Djavanroodi et al. 2019). Figure 2.1 demonstrates the principle

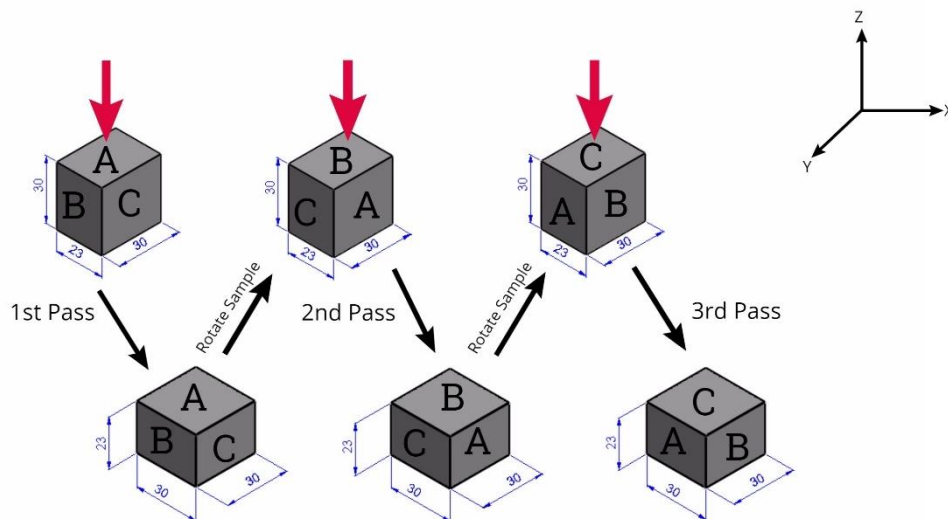


**Figure 2.1: Schematic representation of MDF processing.**

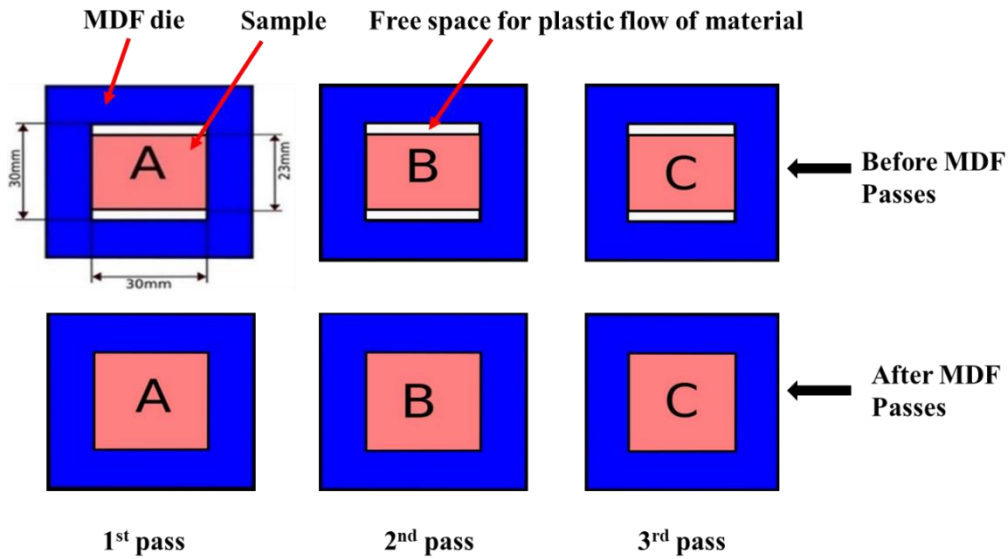


**Figure 2.2: MDF processing of the sample in top view.**

of MDF process. First, the Sample was pressed down to 30 mm along the Z direction (longest side); then, it was turned 90° and forged down to 30 mm along the Y direction (the newly created side); finally, it was turned 90° and forged down to 30 mm along the X direction. After three successful passes of MDF, it is said to be one complete cycle. Figure 2.2 shows the top view of MDF processing. MDF die is represented by a blue colour, the sample is represented by an orange colour, and the white colour represents free space for plastic flow of material during the processing.

### 2.3 Process parameters of MDF process

Multidirectional forging can effectively improve the microstructure and mechanical properties by subjecting the material to high plastic deformation. The processing conditions have a great impact on characteristics of MDF-processed materials. Hence, many parameters, including (a) strain imposed, (b) pressing speed, (c) pressing temperature, and (d) friction and lubrication, affect the characteristics of MDF-processed materials.

#### 2.3.1 Strain Imposed

Expression for the total effective strain imparted on MDF sample is given by Estrin and Vinogradov (2013).

$$\text{total effective strain} = N \ln \frac{a_i}{a_f} \quad \text{Equation 1}$$

where  $N$  is number of passes,  $a_i$  is initial height of the sample, and  $a_f$  is final height of the sample. SPD processes are often repeated several times to accumulate a high strain on the material. However, the number of strains can be increased by increasing the number of passes with a small initial strain, or the number of passes can be decreased by increasing the initial strain. The number of passes mainly depends on the initial strain. It has been shown that using a lower strain increment results in a lower strengthening effect in AA1070 even for the same amount of accumulated strain (Rosochowski et al. 2012).

### **2.3.2 Strain rate**

MDF-processed materials displayed a more uniform microstructure at low pressing speeds. Since strain rate imposed on material depends on the pressing speed, it is realistic to expect a more uniform structure at slower speeds due to the longer time allowed for the recovery process. Miura et al. (2016) performed SPD through multidirectional forging at low and high strain rates at same temperature. It was found that a more homogeneous microstructure occurs at low strain rates.

### **2.3.3 Pressing temperature**

In general, high processing temperatures make materials easily deformable. A finer grain size might be achievable if forging process is performed at lowest possible temperature without significantly fracturing the specimen. Sakai et al. (2014) have mentioned that the maximum processing temperature for the MDF process is well below the recrystallization temperature. Rao et al. (2014) processed aluminium-based alloys at cryogenic temperatures, producing equiaxed sub-grain microstructures.

### **2.3.4 Friction and lubrication**

Lubrication minimises friction between die and workpiece during MDF process. Subsequently, the amount of force required to forge the sample can be reduced. Different forms of lubricants, such as wax, grease, molybdenum disulfide, lubricant oil, nickel, and graphite can be utilised. Lubricants should not be abrasive or corrosive (Ujjwal Kumar et al. 2014).

## **2.4 Merits and demerits of MDF**

### **2.4.1 Merits:**

1. It can process relatively large samples that are ideal for industrial use.
2. Materials are subjected to extremely high strains during MDF process without necessarily changing their dimensions.
3. It can be processed by a traditional forging machine without the need for special tools.
4. Materials that are hard to deform can be forged effectively in MDF.
5. In this process, strain per pass can be controlled by maintaining the height-to-width ratio.
6. Material can be forged at various temperatures, such as in cold, warm, and hot working environments, through MDF.

### **2.4.2 Demerits**

1. The method is time-consuming since the sample must be taken out and rotated for each new pass.

## **2.5 Aluminium-Silicon Alloys**

Aluminium (Al) alloys are categorised according to major alloying elements. Common alloying elements include magnesium, copper, silicon, tin, manganese, and zinc. When compared to other alloys, like cast steel or cast iron, aluminium alloys have a comparatively higher specific strength (Hegde & Prabhu, 2008). Aluminium-silicon alloys are finding more importance in engineering disciplines due to their better physical and mechanical properties. Aluminium-silicon alloys are a good substitute for traditional Fe alloys in many different technical applications because of their attractive features (Singh et al. 2016). Due to their better wear and mechanical characteristics, Al-Si alloys are extensively employed in a variety of engineering applications, including aerospace and automobile sectors. They are an excellent choice for parts of internal combustion engines such as connecting rods, cylinder blocks, cylinder liners, manifolds, and valves. Aluminium-silicon alloys have attracted great interest among the most important materials in tribology applications. Silicon is the most significant alloying component in aluminium-silicon alloy. Silicon decreases the coefficient of thermal expansion, improves corrosion and wear, and enhances casting and machining

properties. Low density of silicon ( $2.3 \text{ gcm}^{-3}$ ) could aid in reducing the total weight of components. Silicon precipitates as hard, practically pure silicon because it is virtually insoluble in aluminium, increasing wear resistance. Silicon is extremely brittle because of its diamond-like crystal structure. Aluminium dissolves a maximum of 1.6 wt.% of silicon at eutectic temperature and about zero percent at ambient temperature. However, solubility of aluminium in silicon is almost zero. The Si content in standardised commercial cast Al-Si alloys is at the level of 5% to 23% (Hegde & Prabhu, 2008). Based on silicon content, the Al-Si alloys are categorised as hypoeutectic (<12% Si), eutectic (12–13% Si), and hypereutectic (>13% Si). Figure 2.3 depicts a phase diagram of a binary Al-Si alloy. According to the Al-Si binary phase diagram, the eutectic reaction occurs at eutectic temperature ( $577^\circ\text{C}$ ). Two solid phases (eutectic Si and aluminium) simultaneously crystallise from the liquid phase (L) with a eutectic composition of 12.6 Si via the reaction of  $L \rightarrow \text{SiE} + \alpha (\text{Al})$  where SiE is eutectic silicon.

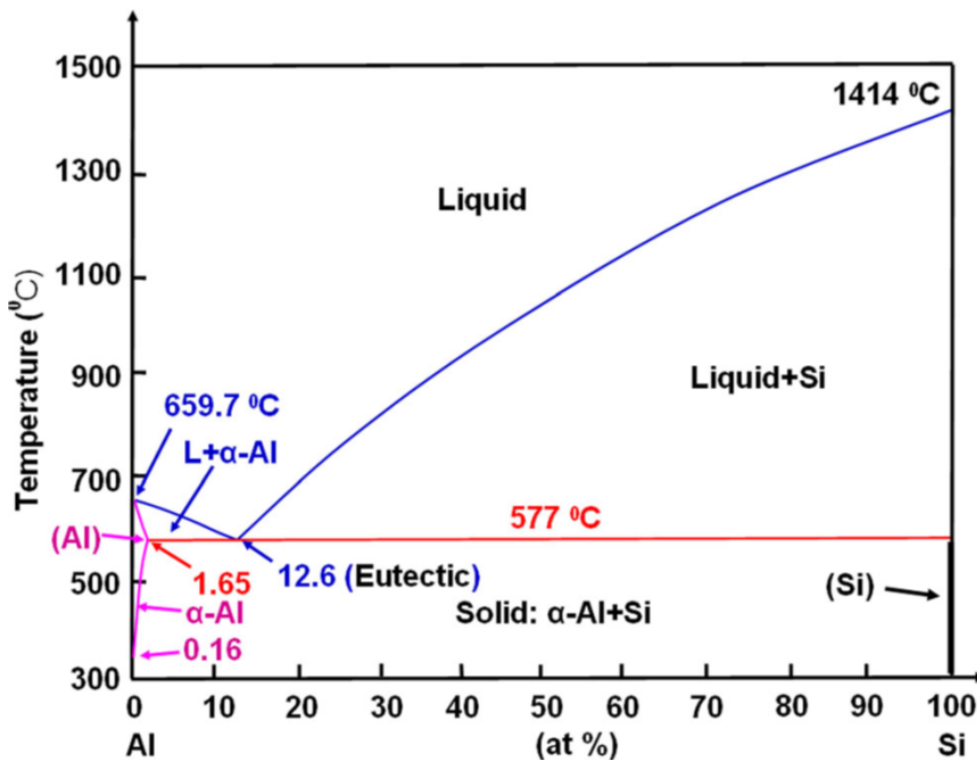


**Figure 2.3: The binary Al-Si alloy phase diagram**

(Richmire, S., & Haghshenas, M. (2019)).

In Al-Si alloys, eutectic silicon refers to the silicon phase that forms during solidification in the eutectic composition at a temperature of 577 °C. For hypoeutectic aluminium-silicon alloys, crystallisation of the Al phase is followed by a eutectic reaction. The reaction for hypoeutectic alloys is  $L \rightarrow L + \alpha(\text{Al}) \rightarrow (\text{SiE} + \alpha(\text{Al})) + \alpha(\text{Al})$ . Hypereutectic Al-Si alloy depicts primary crystallisation of Si precipitates, and then eutectic reaction originates after primary silicon. Hypereutectic reactions generally exhibit the following phase transformation as  $L \rightarrow L + \text{SiP} \rightarrow (\text{SiE} + \alpha(\text{Al})) + \text{SiP}$ , where SiP is primary silicon. Primary silicon refers to precipitated silicon, which is the first phase in the hypereutectic Al-Si alloys. The primary Si has a cuboidal form. When aluminium-silicon alloy solidifies, the primary aluminium phase forms and grows in dendrites, or the Si phase forms and grows into angular primary particles. The eutectic aluminium-silicon phases form when eutectic point is reached and continue to grow until solidification is completed. The soft and ductile primary Al phase with hard and brittle eutectic silicon phase are two phases of hypoeutectic alloys. Hypereutectic alloys include primary silicon particles in addition to a eutectic silicon phase.

### **2.5.1 Hypoeutectic Al-Si alloys**

Hypoeutectic Al-Si alloys consist of a soft and ductile primary aluminium phase with a hard and brittle eutectic silicon phase. Due to their outstanding mechanical properties at high temperatures, great wear resistance, and low coefficient of thermal expansion, these alloys are frequently used for castings in industry, particularly in automotive industry. However, one of the main disadvantages of Al-Si alloys is their low fracture toughness because of their microstructure, which consists of networks of eutectic silicon particles and aluminium dendrites (Al phase). Eutectic silicon crystals are brittle and complex structures, most of which are connected in three dimensions, which makes it easy for a crack to spread among them (Cepeda-Jiménez et al. 2011). The manufacturing of complex designs with a thinner cross-section is made possible by silicon concentrations ranging from 4% to 12%, which also reduces scrap losses and provides castings with improved surface and interior quality. Vessels, Rotors, valve bodies, and fan blade fittings are made up of 3-5% silicon (Hegde and Prabhu, 2008). Hypoeutectic aluminium-silicon alloys (Al-7Si) find applications in food, chemical, marine, electrical, automotive, and many other industries.

### **2.5.2 Eutectic Al-Si alloys**

Aluminium-silicon binary alloy is a eutectic system with a eutectic composition of 12.6 wt.% Si. One of the most commonly used cast alloys in the industry is eutectic Al-Si alloy. The low fracture toughness of these alloys limits their wider industrial application (Nishida et al. 2007). In automotive sector, eutectic alloys (11–13%Si) are utilised for IC engine cylinders, cylinder heads, pistons, and cylinder blocks (Hegde and Prabhu, 2008). The eutectic aluminium-silicon alloys (Al-12Si) have high corrosion resistance in both typical atmospheric and marine environments. These alloys are mainly employed in marine, automobile, and aerospace sectors.

### **2.5.3 Hypereutectic Al-Si alloys**

In hypereutectic aluminium-silicon alloys, the silicon concentration is more than 13%. Due to their potential to replace cast iron in automotive engine components, these alloys with high specific stiffness, low density, high-temperature resistance, good wear resistance, and low coefficient of thermal expansion are of great interest to transportation sector (Vijeesh & Prabhu 2014). High-performance automotive engine components such as rocker arms, connecting rods, cylinders, pistons, and valve retainers are few of main uses for hypereutectic Al-Si alloys (Omran et al. 2017). Heavy-duty diesel engine pistons were cast using hypereutectic Al-Si alloys more than 50 years ago in Germany, the United States, and other countries (Jorstad and Apelian 2009). In addition to a eutectic Si phase, hypereutectic alloys typically contain large primary silicon particles. Wear properties of Al-Si alloys depend on the existence of hard primary Si particles. However, extrudability, machinability, strength, and ductility are negatively impacted by the existence of coarse primary silicon; as a result, its mechanical characteristics are inferior. Superior mechanical properties and wear resistance mainly depend on even distributions of tiny primary Si particles.

### **2.6 Solution heat treatment**

Solution treatment deals with heating alloys to a certain temperature, maintaining that temperature long enough for one or more constituents to dissolve into a solid solution, and then rapidly cooling the alloys to prevent precipitation of dissolved constituents. Solution treatment is performed at high temperature, near eutectic temperature of the alloy. The following goals are achieved by solution heat treatment:

- Dissolve soluble phases containing copper and magnesium formed during solidification.
- Change the morphology of eutectic silicon.
- Distribute the Si phase evenly in the Al phase.

Uniformity of the as-cast microstructure and the spheroidization of eutectic Si phase are two primary objectives of solutionizing. Mechanical characteristics of the alloy are significantly influenced by changes in size and shape of silicon phase. It has been described that granulation or spheroidization process of Si particles through solutionizing takes place in two steps: (1) separation or dissolution of eutectic Si branches, and (2) spheroidization of separated branches (Mohamed & Samuel 2012). The solutionizing causes silicon particles to alter in size and shape. Unmodified Si particles are subjected to necking in the earliest stages and split into segments. Average particle size reduces as a result of the separation, and finally, the broken segments become spheroidized. During second stage, spheroidization of eutectic Si takes place and simultaneously coarsening occurs. The ductility and fracture toughness of the material can be increased by homogenising casting. The next essential stage in solutionizing is quenching. Minimization of precipitation during quenching, keeping as many precipitation-hardening elements in the solution as feasible to produce a supersaturated solid solution and trapping as many vacancies as possible within the atomic lattice are three main goals of quenching. With quick quenching, the greatest balance of ductility and strength can be achieved (Mohamed & Samuel 2012). The quenching media and the quenching interval are both important for the effectiveness of the quenching. Water is the most commonly employed quenchant for aluminium alloys (Sjölander & Seifeddine 2010). It may be noted that some parts of the Si particles are expected to go into the solid solution at solutionizing temperature due to higher solid solubility limit of Si in Al to the extent of ~1% at temperatures above 500 °C (Gupta et al. 2012). When samples are cooled to room temperature after solutionizing, the dissolved Si precipitates as tiny particles.

### **2.7 Influence of SPD on mechanical and microstructure properties of Al-Si alloy**

Al-Si alloy is largely used in industry due to its strong mechanical and physical characteristics. However, their wear and mechanical characteristics are weakened by

existence of micropores and dendritic microstructure with sharp-tipped eutectic Si phases (Singh et al. 2016). Both eutectic silicon phase and aluminium phase can be refined to enhance the mechanical characteristics of this alloy (Haghdadi et al. 2016). Deformation processing is an efficient way to improve mechanical properties (Wanga et al. 2015). Severe plastic deformation (SPD), which alters the microstructure of aluminium-silicon alloys, has received a lot of attention recently. This section reports on evolution of the mechanical and microstructure characteristics of Al-Si alloys that have been subjected to SPD processing.

Kim et al. (2003) conducted experiments on a rotary-die ECAP that was applied to Al-7.5Si-0.45Mg alloy to obtain better ductility and microstructural properties. ECAP was performed at 270 °C, 330 °C, and 400 °C temperatures. Tensile tests were performed at 480 °C, 500 °C, and 520 °C. It was noted that after six passes, there was a significant reduction in Si particles as well as grain size. The grain size was drastically decreased from 20–30 µm to 2–3 µm after six passes. A fairly homogeneous microstructure was attained after 10 passes. After 10 passes, elongation of the material increased from 25% to 125%. The Hv values of the eutectic Si region were significantly decreased from 82.6 Hv to 62 Hv. However, Hv values in the Al matrix were slightly increased from 56.7 Hv to 62 Hv. Ashouri et al. (2008) examined the semi-solid microstructure of aluminium alloy Al-7.2Si-0.4Mg that has been processed by ECAP at ambient temperature. To observe semi-solid microstructure, the processed samples from ECAP were put through an isothermal reheating method at 580 °C with three different holding times. It was mentioned that when strain increases, particle sphericity increases, and size reduces. Gutierrez-Urrutia et al. (2008) investigated the effect of processing temperature and ECAP die angle on grain size of Al-7Si alloy. ECAP was performed at both ambient temperature and intermediate temperature. The coarse silicon particles are broken down into near-micron particles. It was reported slight tendency to microstructural non-uniformity was seen with the high-strain die. When material is severely deformed at an intermediate temperature, the result is a substantially coarser grain size than when annealing room-temperature deformed material. The material produced using the 90° die achieved the same high strength as when processed with the 120° die. Garcia-Infanta et al. (2008) conducted experiments to examine both the

microstructure and tensile properties of an Al-7Si alloy that was subjected to up to eight passes of ECAP. The processed samples showed an increase in ultimate tensile strength (UTS) of about 60%, from 157 MPa for the as-cast sample to about 245 MPa for ECAP-processed samples. It was reported that there was no notable variation in tensile strength between the processed material. Natori et al. (2017) have investigated the effects of ECAP on a semi-solid Al-7.14%Si-0.41%Mg alloy with tiny silicon particles and a traditional cast alloy with coarse silicon particles. The Si particles of traditionally cast material could not be refined by ECAP process as finely as those of the semi-solid cast alloy. It was mentioned that silicon particle and grain refinement, as well as a reduction in variation in the hardness, were all achieved with the combination of semi-solid casting and ECAP process. The tensile strength was increased from 250 MPa to 350 MPa after 4 passes of ECAP process at 200 °C. Similarly, elongation was increased from 21.7% to around 28% after 4 passes of the ECAP process at 300 °C. Gebril et al. (2019) examine the effect of the cooling slope and ECAP method on microstructure of the Al-7Si alloy. ECAP was conducted at ambient temperature with a 120-degree channel angle. As-cast and cooling slope castings that were subjected to heat treatment before ECAP. According to reports, after six passes of ECAP process with heat-treated cooling slope casting, grain and Si particle sizes had significantly decreased. The Si particles were reduced from 4.22  $\mu\text{m}$  to 0.71  $\mu\text{m}$  after six passes of heat-treated cooling slope casting, using the ECAP process. The hardness increased with ECAP processing, from 61 Hv, for the as-cast alloy, to 134 Hv, after six passes of heat-treated cooling slope casting. Syukron et al. (2016) experimented with the microstructural evolution and hardness of ECAPed Al-0.3Mg-7Si alloy with the addition of TiB<sub>2</sub>(1.5%). Before ECAP, samples were subject to annealing. Results of hardness tests revealed that the ECAP process increased the hardness of the material. ECAP processing redistributes Si-phase in the specimen. The hardness increased from around 70 Hv for the as-cast alloy to around 90 Hv after four passes of ECAP at room temperature. Ma et al. (2005) experimented with rotary-die equal-channel to enhance the tensile properties of Al-11Si alloy processed at 300 °C. After ECAP silicon corals were broken and uniformly distributed. ECAP process improved the ductility of the material. The tensile strength increased from around 210 MPa for the as-cast alloy to around 245 MPa after 32 passes of RD-ECAP. The elongation was increased from

around 7% for the as-cast alloy to around 23% after 32 passes of RD-ECAP. The tensile strength increased significantly after first four passes with subsequently steady drop in the tensile strength as ECAP passes increased. It was reported that grain boundary sliding (GBS) resulted in a slight drop in the tensile strength. Hosseinzadeh et al. (2021) studied the effect of ECAP on mechanical properties of SLM as-built Al-12Si alloy. The yield point, ultimate strength, and ductility of the as-built sample were all enhanced after 4 passes of ECAP. It was mentioned that improved mechanical properties were attributed to grain refinement and morphological modification in silicon particles. The tensile strength and elongation were increased from 465 MPa and 3.8% for the as-cast alloy to 514 MPa and 5.9%, respectively, after 4 passes of ECAP. The hardness was increased from 140 Hv for the as-cast alloy to 162 Hv after 4 passes of ECAP. Purcek et al. (2010) examined the mechanical and microstructural characteristics of Al-12Si alloy processed by equal-channel angular extrusion (ECAE). The material was pressed through ECAP for up to 6 passes at 200 °C. The acicular-shaped eutectic Si plates were broken up into smaller pieces as a result of the high stresses that were imposed during ECAE processing. The length and width of the Si particles decreased from  $35.5\pm 31.8$   $\mu\text{m}$  and  $13.7\pm 8.9$   $\mu\text{m}$  to  $2.7\pm 1.1$   $\mu\text{m}$  and  $1.3\pm 0.4$   $\mu\text{m}$  after six ECAE passes, respectively. The tensile strength and elongation were increased from 113 MPa and 1.6% for the as-cast alloy to 190 MPa and 12% after six ECAE passes, respectively. Damavandi et al. (2019) have conducted work on the tensile and microstructure evaluation of Al-18Si-4.2Cu-0.3Mg alloy processed by ECAP. The sample was pre-heated at 300 °C for 15 minutes before each ECAP pass. It was then processed by ECAP at 400 °C. The silicon particle sizes were reduced and more evenly dispersed after ECAP. The mean sizes of ESPs in the as-cast and 1, 2, 3, and 4 passes processed samples were 5.3, 3.4, 3.1, 2.4 and 2.7  $\mu\text{m}$ , respectively. The size of ESPs after the fourth pass is slightly higher than that of ESPs after the third pass due to diffusion phenomena. The tensile strength and elongation were increased from around 125 MPa and 4% for the as-cast alloy to around 250 MPa and 9% after four ECAP passes, respectively. Yoon et al. (2007) reported the influence of ECAP on mechanical characteristics of Al-20Si alloys that quickly solidified and consolidated. Al-20Si alloy was produced by extruding gas-atomized particles at 400 °C. ECAP subsequently processed the powder extrudates. It was found that materials that had undergone ECAP

processing had effectively refined the grain and Si particles. It was mentioned that the greater refinement in the grain size and Si particle led to the increased strength of the alloy after ECAP.

Ma et al. (2006) investigated the impact of FSP to improve the mechanical properties through microstructural refinement of Al-7.2Si-0.36Mg alloy. FSPed material depicted significant microstructural refinement and uniform dispersion of Si particles with reduced porosity. The Si particles decreased from 16.75  $\mu\text{m}$  to 2.44  $\mu\text{m}$  after 1100 rpm of FSP. The author concluded that a higher tool rotation can refine the Si particles, eliminate porosity, and subsequently increase strength. The tensile strength and elongation were increased from 220 MPa and 2% for the T6 heat-treated as-cast alloy to 295 MPa and 28% after 1100 rpm of FSP, respectively. Garca-Infanta et al. (2010) studied the effects of FSP and ECAP on microstructure of a Na-modified Al-7Si alloy at room temperature. FS-processed material showed more homogenised distribution of Si particles than ECAP-processed material. In comparison to FSPed material, ECAPed material demonstrated greater tensile strength. However, the FSPed material has a greater level of ductility than ECAP-processed material. The tensile strength and elongation were increased from around 150 MPa and 15% for the as-cast alloy to around 250 MPa and 20% after eight passes of ECAP, respectively. Similarly, the ductility achieved by FSP was around 40%. Meenia et al. (2016) have studied the effect of pre-process thermal treatment and multi-pass FSP on microstructure and mechanical properties of Al-6.5Si-0.35Mg alloy. Effect of FSP with and without pre-process thermal treatment was studied for up to three passes. It was reported that maximum particle and grain refinement was observed in the material subjected to three passes of FSP with pre-process thermal treatment. FS-processed material with 3 passes without thermal treatment showed maximum ductility. However, maximum tensile strength is obtained in 3-pass material with pre-process thermal treatment. The UTS and elongation were increased from 152 MPa and 4.8% for the as-cast alloy to around 250.7 MPa and 24.5% after combined solution heat treatment and FSP, respectively. Aktarer et al. (2015) experimented with friction stir processing to improve mechanical and microstructural properties of Al-12Si alloy. It was noted that FSP results in uniform distribution of fine silicon particles. The average length of eutectic Si particles

decreases from 27  $\mu\text{m}$  in the as-cast state to about 2.6  $\mu\text{m}$  in the FSPed state. After two passes of FSP, mechanical properties were improved. The UTS and elongation were increased from 167 MPa and 3.4% for the as-cast alloy to around 215 MPa and 25% after two passes of FSP. Two-pass FSP considerably increased the hardness of the alloy inside the nugget zone. The sample shows an increase in the hardness of about 15%, from 58 Hv in the unprocessed as-cast zone to about 67 Hv in the nugget zone. The author reported that significant changes in the form, size, and distribution of Si particles as well as breaking and refinement of grains during two-pass FSP were primarily responsible for the improvements in all mechanical characteristics. Abdul Malik et al. (2018) examined the effect of FSP on microstructure modification, hardness, and tensile properties of Al-18Si-1Cu-1.1Ni alloy. The coarse eutectic and primary silicon particles broke down into fine particles along with reduced porosities after FSP. The mean area of the fragmented Si particles decreased from 155.1  $\mu\text{m}^2$  to around 49.4  $\mu\text{m}^2$  after FSP. After FSP, both ductility and strength of the material increased. The UTS and elongation were increased from about 120 MPa and 2% for as-cast alloy to around 184 MPa and 7.5% after FSP at a tool spindle speed of 1000 rpm. The hardness of the alloy increased from 64.6 Hv for the as-cast alloy to about 85.74 Hv after FSP. According to reports, remarkable changes in the form, size, and distribution of silicon crystals were substantially responsible for the improvement in all of the characteristics of FSPed material. Golafshani et al. (2019) studied the influence of FSP on shear strength microstructure evaluation and of Al-18Si-4.2Cu-0.3Mg aluminium alloy. Hardness increases up to three passes and then decreases after fourth pass. As number of passes increased, it was discovered that the size of Si crystals gradually decreased. The average size of Si particles from the first to the fourth pass is  $2.10\pm 2.01$ ,  $1.64\pm 1.59$ ,  $0.89\pm 0.54$ , and  $0.89\pm 0.60$   $\mu\text{m}$ , respectively. The UTS and hardness were increased from around 110 MPa and 116 Hv for the as-cast alloy to around 130 MPa and 125 Hv after three passes of FSP. The larger grain size and coarser intermetallic compounds after the third pass will decrease the barriers to the movement of dislocations and result in decreasing hardness. The shear strength of FS-processed material was studied by evaluating the strain rate sensitivity with shear punch testing. Richmire & Haghshenas (2019) conducted a study on effects of friction stir welding (FSW) on mechanical and microstructural properties of Al-10Si aluminium sheets. It was found that eutectic

silicon crystals are refined and evenly dispersed after FSW. According to the report, elimination of porosities, refinement of grain, and silicon particles were attributed to the improved mechanical characteristics of FSW-processed materials in the stirring zone.

Venkateswarlu et al. (2011) experimented with effect of HPT on microstructure properties of Al-2Si alloys with and without 0.25% scandium additions. Scandium additions improved the Al grain structure but did not significantly alter the morphology of Si particles. Both experimental alloys were processed by HPT and exhibited sub-micrometre grains with evenly dispersed Si particles. The average length of eutectic Si particles decreases from about 12  $\mu\text{m}$  in the as-cast state to about 1.2  $\mu\text{m}$  after five turns of FSP. It was noted that the hardness and UTS increased as the number of HPT turns increased. With increased turns, the hardness values between the middle and the edge became less different. Alloy 1 exhibited hardness values of  $\sim 61$  Hv at the centre and  $\sim 68$  Hv at the edges in the early stages of HPT processing but after 5 turns the hardness values were  $\sim 67$  Hv at the centre and  $\sim 73$  Hv at the edges. The UTS was increased from 105 MPa for alloy 1 to 325 MPa after five turns of HPT. Similarly, the UTS of alloy 2 was increased from 185 MPa to 375 MPa after five turns of HPT. Al-2Si alloys with 0.25% scandium additions showed better mechanical properties than Al-2Si alloys without scandium. Mungole et al. (2013) experimented with the impact of room-temperature and high-temperature (171  $^{\circ}\text{C}$ ) HPT processing on the surface modification of an Al-7Si alloy. It was discovered that the hardness of processed samples was much higher than that of the cast samples. As-cast sample exhibited hardness values of  $\sim 40$  Hv at the centre and  $\sim 45$  Hv at the edges, but after ten turns, the hardness values were  $\sim 75$  Hv at the centre and  $\sim 77$  Hv at the edges. However, ten turns of HPT samples exhibited hardness values of  $\sim 53$  Hv at the centre and  $\sim 56$  Hv at the edges at higher temperatures. The grains in the samples processed at low temperatures were smaller than those in the samples processed at high temperatures. It was noted that when HPT rotations or applied strain increased, the dispersion of Si particles became fairly uniform. Zhilyaev et al. (2007) researched the influence of HPT on microstructure of an Al-7% Si alloy. HPT was employed to process the material for five turns at ambient temperature and under 6 GPa pressure. With HPT process, the uniformity of silicon particle distribution and refinement of aluminium grains improved. The average length

of eutectic Si particles decreased from ~10–15  $\mu\text{m}$  in the as-cast state to about ~5–10  $\mu\text{m}$  after HPT. Wang et al. (2015) investigated hardness and corrosion properties of Al-7Si alloys processed by HPT. The results showed that Si particles and intermetallic phases were broken into fine particles and uniformly distributed after HPT. With more HPT turns, hardness of the Al-7Si alloy dramatically increased. The average microhardness increased to  $185.0 \pm 4.4$  Hv for the sample processed through 10 turns from  $71.5 \pm 8.0$  Hv for the as-received sample. According to a report, microstructure of the alloy was refined by HPT processing, which enhanced its corrosion resistance and microhardness. Corrosion rate reduced from  $7.41 \mu\text{m y}^{-1}$  for the as-received sample to  $1.68 \mu\text{m y}^{-1}$  for the 10-turn processed sample. Kumar et al. (2017) examined the combined effects of annealing and HPT on ductility and strength of an Al-7Si alloy. The samples were annealed for five hours at  $172^\circ\text{C}$  in a vacuum furnace before HPT. Uniform dispersion of Si particles was improved after HPT. When compared to the as-cast sample, the material that had undergone HPT processing displayed an increase in both strength and ductility. The UTS and elongation were increased from ~150 MPa and ~38% for the as-cast alloy to around ~200 MPa and 95% after 5 turns of HPT. The average microhardness increased to ~75 Hv for the sample processed through 5 turns from ~45 Hv for the as-received sample.

Jamaati et al. (2011) have employed ARB method to manufacture high-strength, finely dispersed and highly-uniform Al-7.3Si-0.3Mg alloy. ARB was conducted at ambient temperature for up to five cycles with equivalent strain of 0.8 per cycle. According to the research, when number of cycles increased, the Si particles became finer and more uniform. The sizes of Si particles for as-cast, as-rolled, one, three and five cycles ARB-processed samples were 11.70, 9.97, 7.12, 6.42, and 4.77  $\mu\text{m}$ , respectively. Furthermore, after fifth cycle of ARB, the as-cast sample's hardness value dramatically increased. After one cycle, the elongation value dropped, and then it increased as the number of cycles increased. Tensile strength and elongation value were increased from 103 MPa and 2.1% for as-cast alloy to 269 MPa and 5.3% after the fifth cycle of ARB. It was mentioned that the uniformity of Si particles has a major effect on both strength and elongation values. Hardness value increased from 55.4 for as-cast sample to 100.2 HV after five cycles of ARB. Mahallawy et al. (2017) have experimented with the

ARB process, which was used to produce Al/Al-12%Si multi-layered composites. The sheets were stacked so that two Al 1050 layers were at the outer surfaces and one Al-12%Si layer between them. The stacked laminates were riveted from one end to produce a sandwich stack. ARB process was carried out at 300 °C. It was reported that Al/Al-12%Si composite with evenly distributed silicon fragments was achieved after five cycles of the ARB process. The UTS was increased from ~225 MPa for the sandwich stack to ~315 MPa after 5 cycles of ARB. The average microhardness increased from 60 Hv to 115 Hv for the Al layer after 5 cycles of ARB. Similarly, average microhardness increased from 115 Hv to 120 Hv for the Al-12%Si layer after 5 cycles of ARB. Dodangeh et al. (2012) experimented with high plastic deformation of the rheoforged Al-7.2Si-0.3Mg alloy to evaluate the microstructure and hardness. In this study, cast Al-7.2Si-0.3Mg aluminium alloy was converted into a semi-solid slurry with a globular structure using the electromagnetic stirring (EMS) method. The slurry was then forged in a die, which is known as rheoforging. Impact of SPD on the mechanical and microstructure characteristics of Al-7.2Si-0.3Mg alloy in dendritic and globular states was examined using multidirectional forging. With no considerable change in the globule morphology of the rheoforged samples, MDF process increased the shear strength and hardness of the samples. The average microhardness increased to 84 Hv for the sample processed through 3 passes of MDF from 61.6 Hv for the as-received sample. Ultimate shear stress increased from 148 MPa for as-cast alloy to 206 MPa after three passes of MDF. Haghdadi et al. (2016) examined the microstructural and tensile properties of an Al-7Si-0.4Mg alloy in a single pass of accumulative back extrusion. As-cast Al-7Si-0.4Mg alloy was processed at temperatures between 200 °C and 500 °C. Microstructural analysis revealed that the fibrous-shaped Si particles were fractured and the globular  $\alpha$ -Al primary phase was divided into fine substructures after ABE processing. Ultimate tensile strength and yield strength of the materials were significantly enhanced after ABE at lower processing temperatures. The UTS was increased from 199 MPa for as-cast alloy to 402 MPa after single pass of accumulative back extrusion at 200 °C. Immanuel and Panigrahi (2015) performed research on microstructural and tensile properties of Al-6.6Si-0.3Mg alloy processed by cryo-rolling at various applied strains. It was found that cryo-rolling eliminated casting porosity, and coarse acicular eutectic particles to break up and distribute uniformly. It

was reported that strength and ductility were significantly improved as a result of microstructural modifications. The UTS and elongation were increased from 129 MPa and 3.8% for the as-cast alloy to 332 MPa and 5.2% for the 87% cryo-rolled sample. Table 2.1 shows overview of SPD on mechanical and microstructure properties of Al-Si alloy.

**Table 2.1: Overview of SPDs on mechanical and microstructure properties of Al-Si alloys.**

<b>Authors</b>	<b>Experiment techniques &amp; Objectives</b>	<b>Outcomes</b>
Kim et al. (2003)	Material: Al-7% Si alloy.  Processing techniques: ECAP(10 passes) at 270°C, 330 °C, and 400 °C.	Hardness of the Al matrix was slightly increased.  Homogenous microstructure was obtained.
Ashouri et al. (2008)	Material: Al-7.2Si-0.4Mg alloy.  Processing techniques: ECAP at ambient temperature.	With increasing strain, the size of the Si particles was reduced.
Gutierrez-Urrutia et al. (2008)	Material: Al-7Si alloy.  Processing techniques: ambient temperature and 200 °C.	Silicon particles were broken down into near-micron particles.
Garcia-Infanta et al. (2008)	Material: Al-7Si alloy.  Processing techniques: Eight passes of ECAP at room temperature.	UTS was increased from 157 MPa for the as-cast sample to about 245 MPa for ECAP-processed samples.  Silicon particle was broken and redistributed.

Natori et al. (2017)	Material: Al-7.14Si-0.41Mg.  Processing techniques: ECAP (4-passes) on semi-solid Al-7.14Si-0.41Mg alloy at 200 °C.	Size of Si particles was reduced after ECAP.  Tensile strength was increased from 250 MPa to 350 MPa after ECAP.  Elongation was increased from ~21.7% to ~28% after ECAP.
Gebril et al. (2019)	Material: Al-7Si alloy.  Processing techniques: Cooling slope and ECAP (6-passes) at ambient temperature.	Size of the Si particles was reduced from 4.22 $\mu\text{m}$ to 0.71 $\mu\text{m}$ after ECAP.  Hardness was increased from 61 Hv, for the as-cast alloy, to 134 Hv after ECAP.
Syukron et al. (2016)	Material: Al-0.3Mg-7Si alloy with the addition of TiB <sub>2</sub> (1.5%).  Processing techniques: ECAP(4-passes) at room temperature.	Silicon particles were reduced and redistributed after ECAP.  Hardness was increased from ~70 Hv for the as-cast alloy to ~90 Hv after ECAP.
Ma et al. (2005)	Material: Al-11Si alloy.  Processing techniques: ECAP (32-passes) at room temperature.	Silicon particles were broken and uniformly distributed.  Tensile strength was increased from ~210 MPa for the as-cast alloy to ~245 MPa after ECAP.

		Elongation was increased from ~7% for the as-cast alloy to ~23% after ECAP.
Hosseinzadeh et al. (2021)	Material: Al-12Si alloy.  Processing techniques: ECAP (4-passes) on SLM as-built Al-12Si alloy.	Silicon particles were reduced.  Tensile strength and elongation were increased from 465 MPa and 3.8% for the as-cast alloy to 514 MPa and 5.9% after ECAP.  Hardness was increased from 140 Hv for the as-cast alloy to 162 Hv after ECAP.
Purcek et al. (2010)	Material: Al-12Si alloy.  Processing techniques: ECAE (6-passes) at 200 °C.	Length and width of the Si particles decreased from 35.5±31.8 μm and 13.7±8.9 μm to 2.7±1.1 μm and 1.3±0.4 μm after ECAP, respectively.  The tensile strength and elongation were increased from 113 MPa and 1.6% for the as-cast alloy to 190 MPa and 12% after ECAE respectively.
Damavandi et al. (2019)	Material: Al-18Si-4.2Cu-0.3Mg alloy.  Processing techniques: ECAP (4-passes) at 400 °C.	Sizes of Si particles in the as-cast and 1, 2, 3, and 4 passes processed samples were 5.3, 3.4, 3.1, 2.4 and 2.7 μm, respectively.

		Tensile strength and elongation were increased from ~125 MPa and 4% for the as-cast alloy to a~250 MPa and 9% after four ECAP passes, respectively
Yoon et al. (2007)	Material: Al-20Si alloys.  Processing techniques: ECAP (8-passes) at 400 °C.	Size of the Silicon particles was reduced after ECAP  Enhanced tensile strength was up to 350 from 280 MPa.
Ma et al. (2006)	Material: Al-7.2Si-0.36Mg alloy.  Processing techniques: FSP 1100 rpm.	The Si particles decreased from 16.75 μm to 2.44 μm after FSP.  Tensile strength and elongation were increased from 220 MPa and 2% for the T6 heat-treated as-cast alloy to 295 MPa and 28% after FSP, respectively.
Garca-Infanta et al. (2010)	Material: Na-modified Al-7Si alloy.  Processing techniques: FSP (800rpm) and ECAP (8-passes) at room temperature.	Uniform distribution of Si particles was observed.  The tensile strength and elongation were increased from ~150 MPa and 15% for the as-cast alloy to ~250 MPa and 20% after ECAP, respectively.  Ductility achieved by FSP was around 40%.
Meenia et al. (2016)	Material: Al-6.5Si-0.35Mg alloy.	Silicon particle refinement was observed.

	Processing techniques: FSP (3-passes at 800 rpm).	UTS and elongation were increased from 152 MPa and 4.8% for the as-cast alloy to around 250.7 MPa and 24.5% after FSP, respectively.
Aktarer et al. (2015)	Material: Al-12Si alloy.  Processing techniques: FSP (2-passes at 1250 rpm).	Silicon particles decreased from 27 $\mu\text{m}$ in the as-cast state to about 2.6 $\mu\text{m}$ after FSP.  The UTS and elongation were increased from 167 MPa and 3.4% for the as-cast alloy to around 215 MPa and 25% after FSP.  Hardness is increased from 58 Hv in the unprocessed as-cast zone to about 67 Hv in the processed zone.
Abdul Malik et al. (2018)	Material: Al-18Si-1Cu-1.1Ni alloy.  Processing techniques: FSP (1000 rpm).	The size of Si particles decreased from 155.1 $\mu\text{m}^2$ to around 49.4 $\mu\text{m}^2$ after FSP.  UTS and elongation were increased from ~120 MPa and 2% for as-cast alloy to ~184 MPa and 7.5% after FSP.  Hardness of the alloy increased from 64.6 Hv for the as-cast

		alloy to about 85.74 Hv after FSP.
Golafshani et al. (2019)	Material: Al-18Si-4.2Cu-0.3Mg.  Processing techniques: FSP (600, 800, 1000, and 1200 rpm).	Average size of Si particles from the first to the fourth pass is $2.10\pm 2.01$ , $1.64\pm 1.59$ , $0.89\pm 0.54$ , and $0.89\pm 0.60$ $\mu\text{m}$ , respectively.  UTS and hardness were increased from $\sim 110$ MPa and 116 Hv for the as-cast alloy to $\sim 130$ MPa and 125 Hv after FSP.
Venkateswarlu et al. (2011)	Material: Al-2Si alloys with and without 0.25% scandium.  Processing techniques: Five turns of HPT.	Average length of eutectic Si particles decreases from about 12 $\mu\text{m}$ in the as-cast state to about 1.2 $\mu\text{m}$ after HPT.  UTS was increased from 105 MPa for alloy 1 to 325 MPa after five turns of HPT. Similarly, the UTS of alloy 2 was increased from 185 MPa to 375 MPa after five turns of HPT.
Mungole et al. (2013)	Material: Al-7Si alloy.  Processing techniques: Ten turns of HPT at room temperature.	Silicon particles were uniformly distributed.  Hardness was increased from $\sim 40$ Hv for the as-cast sample

		to ~75 Hv after ten turns of HPT
Zhilyaev et al. (2007)	Material: Al-7Si alloys.  Processing techniques: Five turns of HPT.	The average length of eutectic Si particles decreased from ~10–15 $\mu\text{m}$ in the as-cast state to about ~5–10 $\mu\text{m}$ after HPT
Wang et al. (2015)	Material: Al-7Si alloys.  Processing techniques: Ten turns of HPT.	Si particles were broken into fine particles and uniformly distributed after HPT.  The average microhardness increased to $185.0 \pm 4.4$ Hv for the sample processed through 10 turns from $71.5 \pm 8.0$ Hv for the as-received sample.
Kumar et al. (2017)	Material: Al-7Si alloys.  Processing techniques: annealing and HPT (5-turn).	Uniform distribution of Si particles was improved after HPT.  UTS and elongation were increased from ~150 MPa and ~38% for the as-cast alloy to around ~200 MPa and 95% after 5 turns of HPT.  Hardness was increased to ~75 Hv for the sample processed through 5 turns from ~45 Hv for the as-received sample.
Jamaati et al. (2011)	Material: Al-7.3Si-0.3Mg alloy.	Sizes of Si particles for as-cast, as-rolled, one, three and five

	<p>Processing techniques: ARB at ambient temperature for up to five cycles.</p>	<p>cycles ARB-processed samples were 11.70, 9.97, 7.12, 6.42, and 4.77 <math>\mu\text{m}</math>, respectively.</p> <p>Tensile strength and elongation were increased from 103 MPa and 2.1% for as-cast alloy to 269 MPa and 5.3% after ARB.</p> <p>Hardness increased from 55.4 Hv for as-cast sample to 100.2 Hv after ARB.</p>
Mahallawy et al. (2017)	<p>Material: Al/Al-12%Si multi-layered composites.</p> <p>Processing techniques: Five cycles of the ARB process at 300 °C.</p>	<p>Uniform distributed silicon fragments were achieved after the ARB process.</p> <p>UTS was increased from ~225 MPa for the sandwich stack to ~315 MPa after ARB.</p> <p>Average microhardness increased from 115 Hv to 120 Hv for the Al-12%Si layer after ARB.</p>
Dodangeh et al. (2012)	<p>Material: Al-7.2Si-0.3Mg alloy.</p> <p>Processing techniques: Rheoforged and MDF.</p>	<p>Average microhardness increased to 84 Hv for the sample processed through 3 passes of MDF from 61.6 Hv for the as-received sample.</p>
Haghdadi et al. (2016)	<p>Material: Al-7Si-0.4Mg alloy</p>	<p>Size of Si particles was reduced after ABE.</p>

	Processing techniques: ABE(1-pass) processing at temperatures between 200 °C and 500 °C.	The UTS was increased from 199 MPa for as-cast alloy to 402 MPa after ABE at 200 °C.
Immanuel and Panigrahi (2015)	Material: Al-6.6Si-0.3Mg alloy.  Processing techniques: Cryo-rolling.	Coarse acicular eutectic particles were reduced and distributed uniformly.  UTS and elongation were increased from 129 MPa and 3.8% for the as-cast alloy to 332 MPa and 5.2% for cryo-rolled sample.

## 2.8 Wear and wear mechanisms

Wear is described as removal of material from one or both surfaces when two surfaces are in contact. It is a method of gradually removing material from solid surfaces. The detached material becomes loose wear debris. Wear causes damage to the material on contact surfaces. Numerous mechanical, physical, and chemical factors cause materials to wear. One of the most common problems in the industry is wear, which leads to replacement of machine parts (Kori & Chandrashekharaiyah 2007). Serviceability and durability of engineering components are significantly impacted by wear. Wear results in deterioration of material in machine technology as fracture, fatigue, and corrosion (Alfred 2006). Therefore, when designing engineering parts, wear characteristics must be considered. It is common knowledge that the hardness of a material directly relates to wear resistance. Wear is often a very slow process in well-designed tribological systems, but it is very steady and continuous (Bhushan 2012). Wear properties of a material depend on a variety of variables, including load, sliding speed, counter-face, lubrication, and environmental conditions. In general, investigations on wear of engineering materials focus more on influence of load and less on impact of sliding speed. Wear resistance of structural components significantly impacts the friction

coefficient as they move against one another. Tribological performance of materials can typically be assessed in two ways. In first case, the material is kept moving against a metal counter-face to examine how well it resists metallic wear. In second case, an appropriate abrasive media will be utilised as a counter-face to examine the material's resistance to abrasion. There are now three primary concerns in overcoming wear problems, namely: 1) Invention and use of new tribo-materials with improved tribological properties, including lubricant development: 2) Development and use of new production technologies that provide traditional materials with new qualities; 3) Development and use of new tribological coatings and surface modifications (Kandeva-Ivanova et al. 2016).

During sliding, materials experience different wear mechanisms under various conditions. To reduce wear, it is essential to know the wear mechanism. However, wear process involves one or a combination of wear mechanisms, which include abrasive, adhesive, erosive, oxidation and corrosive wear (Kato 2005). Wear of solids is typically viewed as a mechanical process. The only exceptions to this are oxidation, corrosion, and other chemical reactions. From a technological perspective, abrasive wear and contact fatigue are most significant. According to estimates, abrasion accounts for 80–90% of the overall wear of machine parts, and fatigue wear accounts for 8%. Contributions from other types of wear are small (Alfred 2006).

### 2.8.1 Adhesive Wear

In adhesive wear, material is transferred from one surface to another during sliding as a result of the solid-phase welding process. The adhesive wear process is schematically shown in Figure 2.4. The adhesive takes place when two flat bodies come into contact with each other while rubbing, whether lubricated or not. Adhesion takes place at the

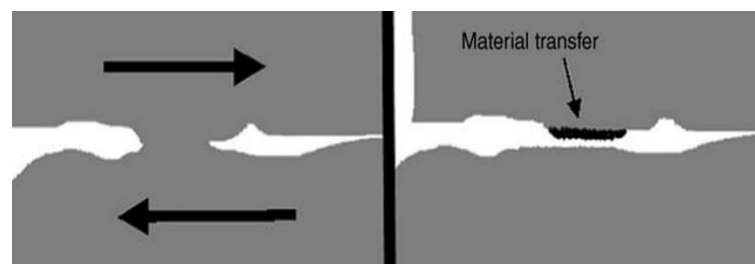


**Figure 2.4 Illustration of adhesive wear mechanism (Affatato & Brando 2013).**

asperity junction, and wear debris is dragged off one surface and stuck to other through adhesion (or bonding) (Bhushan 2012). Dwivedi (2010) reported that adhesive wear takes place when two smooth bodies sliding over one another. During sliding, softer material is pulled away by harder countersurface. As a result, intermetallic adhesion will occur, which leads to growth of cold weld junctions. The transferred wear particles may either drop or transfer back to the soft surface.

### 2.8.2 Abrasive Wear

This type of wear takes place when a hard and rough surface moves across a softer surface, creating a pattern of grooves. Abrasive wear resistance is crucial in many industries because it is one of the most frequent types of wear. Estimated costs of abrasive wear are between 1% and 4% of the total national product of developed countries (Kandeva-Ivanova et al. 2016). The most noticeable type of wear is abrasive wear, whose wear process is primarily mechanical. Abrasive wear is influenced by a variety of factors, including typical load, sliding distance, hardness of the softer material coming into contact, the amount and size of abrasive particles, etc. Abrasive wear is categorised into two types: two-body wear and three-body wear. In two-body abrasion, wear results from a hard projection on one surface that removes material from

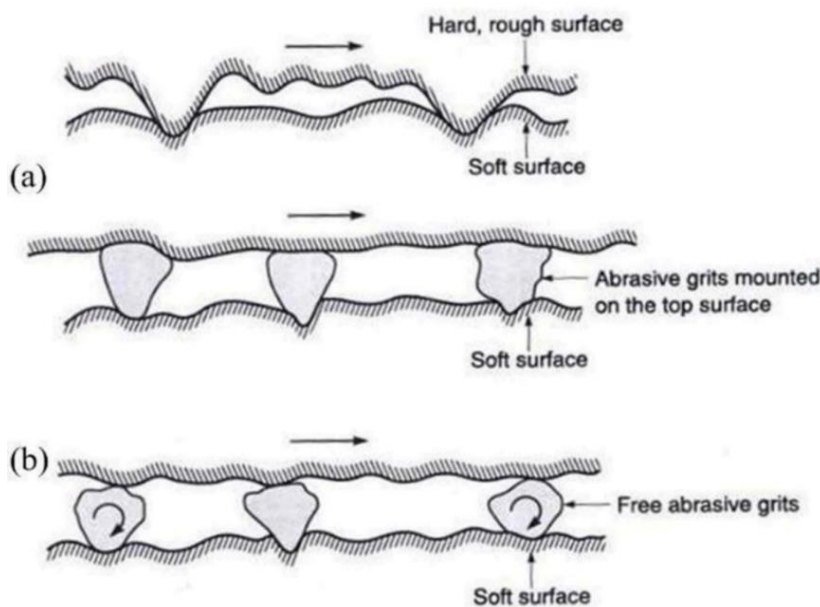


**Figure 2.5 (a) Two body abrasive wear; (b) Three body abrasive wear (Bhushan, 2002).**

the opposite surface. Abrasion action is caused by a cutting or ploughing operation, as depicted in Figure 2.5 a. In three-body erosion, as depicted in Figure 2.5b, the particles are trapped between two solid surfaces but are free to roll and move. Abrasive particles result either internally (wear particles) or externally (contaminants) in tribological systems. According to the degree of contact, abrasive wear is divided into three modes, such as ploughing, wedge-forming, and cutting mode, as shown in Figure 2.6. In ploughing mode, ridges formed along the sides of grooves, and no loose wear debris was formed; only a groove or furrow remained. When a wedge is formed, the material is pushed in front of the grit to create a wedge-like shape. Wedge expands until it eventually separates, at which point the process starts over. Both sides of the groove develop little ridges. Thus, small-scale ploughing may also take place in wedge-forming mode. An intermediary mechanism between cutting and ploughing is the creation of wedges. In cutting mode, lost material from the wearing surface occurs in the form of

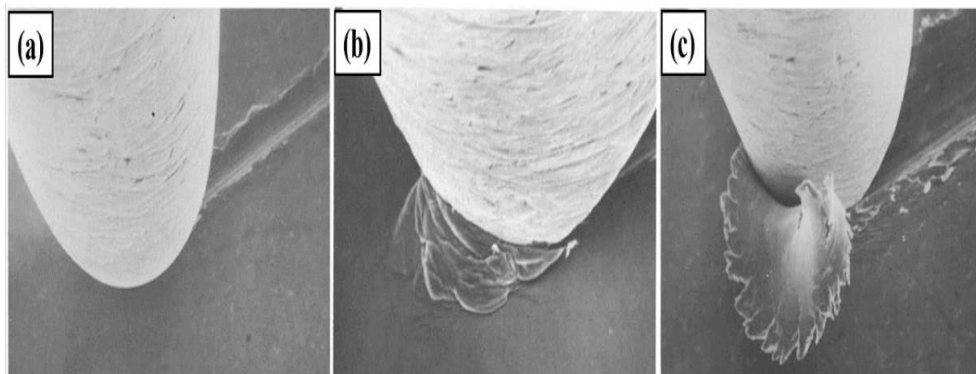


**Figure 2.6 Illustration of Abrasive wear modes (a) ploughing mode (b) wedge forming mode (C) cutting mode (Hokkirigawa and Kato 1988).**

chips. Both sides of the groove develop little ridges. Consequently, small-scale ploughing may also take place during cutting process. (Hokkirigawa and Kato 1988).

### **2.8.3 Erosive wear**

This wear mechanism is caused when eroding particle impinges on the surface of material at a very high velocity. Erosive wear can be classified into three types: (1) solid particle wear; (2) fluid impingement wear; and (3) cavitation wear. The shapes and sizes of the erodent particles, the impingement angle, the impingement velocity, and screening by rebounding particles are typical characteristics connected with many

types of erosive wear testing (Kandeva-Ivanova et al. 2016). Erosive wear is also an expensive type of wear in industry, like abrasive wear. It affects conveyor systems, turbomachinery, pumping equipment, and pipes. According to Alfred (2006), in case of erosive wear, the weight lost is proportional to high power of the particle velocity. Basic strategies for reducing erosive wear include lowering fluid/particle velocity, removing solid particles, and selecting the right material based on impact angle.

#### **2.8.4 Fretting**

Fretting is a unique form of wear that takes place at the point where two materials come into contact while being loaded and is characterised by tiny relative movements caused by vibration or another force. When adherent particles are removed from a surface, the damage increases and starts with local adhesion between mating surfaces. Surfaces that have adhering particles removed from them may react with air or other corrosive conditions. Surfaces that have been affected have pits or grooves from nearby corrosion products. On ferrous metals, corrosion often appears as a very thin, reddish iron oxide; on aluminium, it typically takes the form of a black material. Noble metals are damaged, but the scrap doesn't oxidise.

#### **2.8.5 Corrosive and oxidation wear**

This type of wear results when sliding occurs in a corrosive atmosphere. This wear involves the removal of the corroded layer on top of the material. Oxidation wear, which occurs when materials slide in an oxidising or damp environment, is the most common type of corrosive wear. Corrosion and wear together result in corrosive wear, a process of material degradation. Without sliding, the corrosion products (such as oxides) would form a film on the surfaces, which would generally tend to slow down or even completely stop the corrosion, but sliding action wears the film away so that additional corrosion can occur. Metallic surfaces exposed to any atmosphere containing oxygen will get oxidised, resulting in the formation of a thin oxide deposit. One of the common types of corrosive wear is oxidation wear since this process typically takes place in oxygen-rich environments. High-temperature, high-humidity environments lead to chemical corrosion.

## **2.9 Wear study of SPD-processed Al-Si materials**

Al-Si alloys are employed as wear-resistant materials in many engineering applications. Also, hard second phase (eutectic Si) of Al-Si structure prevents material removal from the component. Microstructure of as-cast Al-Si alloy has a significant influence on their wear performance during service. Wear behaviour of these alloys is determined by hardness of Al phase and evenly distributed fine Si particles (Kori & Chandrashekharaiah 2007). Numerous parameters, including the hardness, strength, ductility, form, and size of the microstructural components, affect the wear properties of Al-Si alloys. In addition to these, practical considerations including pressure, speed, temperature, ambient conditions, and rubbing surfaces also have an impact on the wear properties of Al-Si alloys. However, it has low wear resistance in an as-cast state due to its dendritic microstructure structure with sharp silicon particles, porosity, inclusion, etc. Serviceability and durability of engineering components are significantly impacted by wear characteristics. Therefore, when designing engineering parts, wear characteristics must be considered. Some effective methods to solve this problem are heat treatment, microstructure alteration by the introduction of alloying elements (i.e., Sr), and the use of extreme plastic strain methods. These techniques are employed to change the morphology of sharp Si particles through fragmentation and spheroidization. Using grain refiner and/or modifier additives, various studies have demonstrated enhanced wear resistance in aluminium-silicon alloys. On the other hand, an enormous amount of study has been done on the tribological wear behaviour of an Al-Si alloy. Severe plastic-deformed materials have received a lot of attention due to their better physical and mechanical properties. SPD results in the production of fine-grained materials with exceptional mechanical properties, including high strength and tolerable hardness. However, earlier studies on the wear behaviour of SPD-processed materials revealed contradictory outcomes (Kucukomeroglu, T. 2010). In this section, the wear properties of SPD-processed Al-Si alloys are reviewed.

Thuong et al. (2015) examined the influence of ECAP on microstructural of semi-solidly Al-7Si-Mg alloy using a cooling slope casting and traditional casting of Al-7Si-Mg alloy. The microstructure of cooling slope-cast alloy processed by ECAP was more homogeneous than microstructure of samples processed through traditional

casting. In comparison to the traditional cast ECAPed sample, the cooling slope-cast ECAPed sample had a greater hardness. The Si particles decreased from 4.66  $\mu\text{m}$  for cooling slope-cast annealed to 2.36  $\mu\text{m}$  after ECAP. Similarly, Si particles decreased from 4.98  $\mu\text{m}$  for conventionally cast annealed to 2.56  $\mu\text{m}$  after ECAP. Wear resistance of the material increased as a result of ECAP processing and cooling slope casting. Syukron et al. (2019) examined the wear resistance of Al-7Si-0.3Mg alloys with 1.5%  $\text{TiB}_2$  and enhanced them using a combination of heat treatment, grain refiner addition, and ECAP. Alloys were classified into pre-ECAP annealing samples and cast samples. Pre-ECAP annealing samples depicted increased hardness than as-cast samples. It was reported that considerable strain hardening and grain refining after ECAP were the main causes of the increase in hardness in pre-ECAPed samples. Pre-ECAP annealed specimens showed better wear resistance. Kucukomeroglu (2010) studied effects of ECAP on wear and mechanical behaviour of Al-12Si alloys. Material was processed at 200 °C through ECAP. The acicular-shaped eutectic silicon plates were broken up into finer particles and distributed evenly after ECAP processing. Mechanical properties (ductility and tensile strength) of the material were significantly improved by ECAP processing. The UTS and elongation were increased from ~122 MPa and 2.2% for as-cast alloy to ~180 MPa and 10.2% after ECAP. However, the ECAP method does not lead to enhancement in wear resistance for the Al-12Si alloy. In contrast, the wear resistance was slightly decreased by the ECAP process. This was mainly attributed to the tribochemical reaction leading to oxidative wear with the abrasive effect in Al-Si alloys during sliding. The oxide layer played a dominant role in determining the wear resistance of the sample in both as-cast and ECAP-processed states, and it masked the effect of strengthening of alloy structure on the wear resistance.

Singh et al. (2016) reported that wear properties and machinability of Al-6.6Si-0.35Mg alloy improved with FSP. A metallic and abrasive media was used to assess the wear resistance of FSPed materials. Material that has been through three passes of FSP has superior wear resistance under metallic wear conditions. FSPed material with two passes has the highest wear resistance under abrasive wear. However, in all cases, the friction coefficient was constant. Alidokht et al. (2012) conducted a wear and

microstructure analysis of Al-7.2Si-0.4Mg alloy processed by FSP, which resulted in a remarkable breakdown of acicular silicon crystals and aluminium dendrites. FS-processed material showed increased hardness compared to the as-cast material. The average hardness increased to 84 BHN for the sample processed through FSP at a rotational speed of 1250 rpm from 55 BHN for the as-received sample. It was mentioned that important changes in size, form, and distribution of Si crystals, as well as grain refinement and hardness enhancement, led to an improvement in wear resistance. Additionally, it was discovered that increased tool rotation speeds improved microstructure refinement and, hence, increased wear resistance. Reddy et al. (2010) examined the effect of FSP on the surface modification of Al-7Si-0.35Mg alloy. Hardness mapping revealed a 40% improvement in hardness in stir zones compared to as-cast metal. In the friction-stirred processing zone, microhardness of 85Hv was observed. FS-processed material displayed exceptional wear resistance. According to reports, broken dendritic structure and evenly distributed Si crystals were the reasons behind the increased wear resistance. Stawiarz et al. (2019) investigated the mechanical and tribological properties of an Al-10.5Si-3.2Cu /SiCp composite reinforced with SiC crystal and modified using FSP. FS-processed material had significant fragmentation of Si and SiC reinforcing particles. The distribution of reinforcing particles appeared to be more uniform. The microhardness increased and the specific wear rate decreased after FSP process. According to reports, the attained homogeneity of particle distribution and reduction of particle size were responsible for both outcomes. Aktarer et al. (2017) examined the impact of FSP on friction and wear behaviour of Al-12Si alloy. In comparison to the as-cast sample, FSPed samples showed much less weight loss when subjected to higher loads. It was noted that the wear behaviour of the Al-12Si material improved with the refinement and distribution of Si particles. Average coefficient of friction was not drastically altered after FSP. Mahmoud (2013) experimented with FSP for the modification of the Al-16Si-4Cu-0.6Mg alloy surface. FS-processing greatly reduced the silicon particles and grain size. The Si particle size and aspect ratio were both significantly reduced by FSP. In comparison to as-cast alloy, the friction stir-processed portions showed fewer scattered particles and higher hardness values. FS-processed material had reduced wear rates and coefficients of friction than the unprocessed material.

Aal et al. (2014) conducted experiments on an Al-7Si alloy processed through HPT at ambient temperature. Before HPT, the Al-7Si alloy ingots were subjected to a slow cooling process after being annealed at 540 °C for 20 hours. After HPT, the microhardness dramatically improved. After HPT, the weight loss and Coefficient of friction (COF) dropped. Before HPT, the wear mechanism included delamination, adhesive, plastic deformation bands, and oxidation wear; after HPT, it included both adhesive and abrasive wear. According to the report, the better wear resistance after HPT process was mainly due to the even distribution of Si crystals and grain refinement. Gode et al. (2014) evaluated the effects of HPT on the wear and mechanical characteristics of Al-15Si-2.5Cu alloy and its composite, which was reinforced by SiC particles. The samples were prepared through the powder metallurgy technique and hot extrusion at 565 °C. Hot-extruded samples were then processed using HPT. The HPT process, the Al-Si-Cu alloy, as well as Al-Si-Cu/SiCp composite, greatly improved in terms of hardness and tensile strength. According to the results of wear tests, wear loss reduced after HPT. It was mentioned that the better refining and uniform microstructure were primarily responsible for the increased wear resistance of these alloys. Immanuel and Panigrahi (2016) experimented with two alternative thermo-mechanical processing approaches to improve the wear resistance of a cast Al-7.2Si-0.44Mg alloy. As-cast plates were solutionized at 540 °C for 8 hours in the first thermo-mechanical approach, which was followed by water quenching. After solution treatment, the materials were cryo-rolled over a number of passes. Samples were immersed in liquid nitrogen before each pass. Strength and ductility of the material increased after cryo-rolling. Thermally treated material has the highest level of wear resistance, followed by cryo-rolled material with pre-roll thermal treatment. Table 2.2 shows overview of SPD on wear properties of Al-Si alloy.

**Table 2.2: Overview of SPDs on wear properties of Al-Si alloys.**

<b>Authors</b>	<b>Experiment techniques &amp; Objectives</b>	<b>Outcomes</b>
Thuong et al. (2015)	Material: Al-7Si-Mg alloy.	Si particles decreased from 4.66 μm for cooling slope cast sample to 2.36 μm after ECAP.

	<p>Processing techniques: ECAP on cooling slope casting and traditional casting Al-7Si-Mg alloy.</p>	<p>Similarly, Si particles decreased from 4.98 <math>\mu\text{m}</math> for conventionally cast samples to 2.56 <math>\mu\text{m}</math> after ECAP.</p> <p>Wear resistance of the CSE sample was higher than that of the CCE sample.</p>
<p>Syukron et al. (2019)</p>	<p>Material: Al-7Si-0.3Mg alloys with 1.5% TiB<sub>2</sub>.</p> <p>Processing techniques: Annealing and ECAP; as-cast and ECAP.</p>	<p>Combined annealing and ECAP specimens showed better wear resistance than as-cast and ECAP.</p>
<p>Kucukomeroglu (2010)</p>	<p>Material: Al-12Si alloy.</p> <p>Processing techniques: ECAP at 200 °C.</p>	<p>Silicon particles were broken into smaller and distributed uniformly.</p> <p>The UTS and elongation were increased from ~122 MPa and 2.2% for as-cast alloy to ~180 MPa and 10.2% after ECAP.</p> <p>Wear resistance slightly decreased after ECAP.</p>

<p>Singh et al. (2016)</p>	<p>Material: Al-6.6Si-0.35Mg.</p> <p>Processing techniques: FSP(3-passes at 800 rpm).</p>	<p>Silicon particles were fragmented and redistributed after FSP.</p> <p>Material with three passes of FSP has superior wear resistance under metallic wear conditions. FSPed material with two passes has the highest wear resistance under abrasive wear.</p>
<p>Alidokht et al. (2012)</p>	<p>Material: Al-7.2Si-0.4Mg.</p> <p>Processing techniques: FSP (at 500, 800, and 1250 rpm).</p>	<p>Si particles decreased from ~15 <math>\mu\text{m}</math> for as-cast alloy to ~4.8 <math>\mu\text{m}</math> after FSP.</p> <p>Wear resistance increased after FSP.</p>
<p>Reddy et al. (2010)</p>	<p>Material: Al-7Si-0.35Mg alloy.</p> <p>Processing techniques: FSP rotational speed of 2000 rpm.</p>	<p>Silicon particles were uniformly distributed in the matrix after FSP.</p> <p>FS-processed material displayed exceptional wear resistance.</p>
<p>Stawiarz et al. (2019)</p>	<p>Material: Al-10.5Si-3.2Cu /SiCp.</p> <p>Processing techniques: FSP rotational speed of 900 rpm.</p>	<p>FS-processed material had significant fragmentation of Si and SiC reinforcing particles.</p> <p>Wear rate decreased after FSP process.</p>

Aktarer et al. (2017)	<p>Material: Al-12Si alloy</p> <p>Processing techniques: FSP at 1250 rpm (2-passes).</p>	<p>Si particle size was reduced and uniformly distributed after FSP.</p> <p>Wear resistance increased after FSP.</p>
Mahmoud (2013)	<p>Material: Al-16Si-4Cu-0.6Mg alloy</p> <p>Processing techniques: FSP(3-passes) at 1200 rpm</p>	<p>Average size of eutectic Si particles decreases from ~59 <math>\mu\text{m}</math> in the as-cast state to 1.18 <math>\mu\text{m}</math> in the FSPed state.</p> <p>Wear resistance of FS-processed material was higher than unprocessed material.</p>
Aal et al. (2014)	<p>Material: Al-7Si alloy</p> <p>Processing techniques: HPT (10-turn).</p>	<p>Average size of eutectic Si particles decreases from 5.6 <math>\mu\text{m}</math> for as-cast alloy to 1.6 <math>\mu\text{m}</math> after HPT.</p> <p>Better wear resistance was observed after the HPT process.</p>
Gode et al. (2014)	<p>Material: Al-15Si-2.5Cu alloy.</p> <p>Processing techniques: HPT (5-turn).</p>	<p>Wear resistance increased after HPT.</p>

Immanuel and Panigrahi (2016)	Material: Al-7.2Si-0.44Mg alloy.  Processing techniques: solution treatment and cryo-rolling.	Solution-treated, followed by cryo-rolled material, showed better wear resistance.
-------------------------------	---	--

## 2.10 Summary of Literature Review

In this chapter, SPD techniques were discussed, and their advantages compared to other conventional techniques were elaborated. Multidirectional forging process principle was discussed. The merits and demerits of MDF process compared to other SPD and conventional techniques were discussed. Influence of various processing parameters on resulting mechanical microstructure properties was elaborated to get a complete understanding of the process. Reports on various SPD studies on the Al-Si alloys were discussed.

Literature review revealed that many studies have been performed to improve mechanical and wear properties of Al-Si alloys through SPD. However, limited information is available about influence of SPD on mechanical and wear properties of hypoeutectic and eutectic aluminium-silicon alloys at room temperature. In SPD-processed aluminium-silicon alloys, both favourable and unfavourable effects were reported. Still no clear information regarding combined effect of solution heat treatment and multidirectional room temperature forging on mechanical properties of hypoeutectic (Al-7Si alloys) and eutectic Al-Si alloys (Al-12Si alloys). Furthermore, wear properties of MDF-processed hypoeutectic and eutectic Al-Si alloys at room temperature have not yet been studied. Also, no clear study exists regarding the role of silicon particle size and its distribution on the wear and mechanical properties of MDF-processed hypoeutectic and eutectic Al-Si alloys. Aluminium-silicon alloys typically have low ductility due to the presence of silicon particles. Low ductility of these metals has been a major issue in deformation processes. Furthermore, MDF can process relatively large samples and is a cost-effective method. Additionally, this process can be easily applied to materials at room temperature due to its low-strain

application. In this process, strain can be controlled by maintaining the height-to-width ratio. Therefore, in the present study, effects of multidirectional room temperature forging on microstructure, mechanical properties, and wear behaviours of hypoeutectic (Al-7.3Si) and eutectic (Al-12.1Si) Al-Si alloys are investigated. Furthermore, flow properties and scratch hardness of processed and unprocessed Al-Si alloys are studied. Both alloys were successfully forged in MDF at room temperature.

### **2.11 Objectives of present work**

Based on the literature gaps identified in the literature survey and considering the scope of the present work, the following objectives are outlined:

- 1) Process the solution heat-treated Al-Si alloy by the technique of multidirectional forging at room temperature.
- 2) Characterize the MDF-processed Al-Si alloy using an optical microscope, SEM, and XRD.
- 3) Evaluate the combined effect of solutionizing and multidirectional room temperature forging on the mechanical properties of Al-Si alloys.
- 4) Evaluate the flow properties and scratch hardness of MDF-processed Al-Si alloy
- 5) Study the wear properties of MDF-processed Al-Si alloys under different wear conditions.



## CHAPTER 3

### EXPERIMENTAL PROCEDURES

This chapter explains the experiments related to the multidirectional forging of solution heat-treated Al-Si alloys. The following sections provide an overview of the experimental technique and equipment used for the analysis of unprocessed and processed materials.

#### 3.1 Materials

In the present work, commercially available LM-25 (Al-7.3Si) and LM-6 (Al-12.1Si) alloy ingots procured from RSA Metals, Coimbatore, India, were used. The composition of these materials is presented in Table 3.1. The chemical composition of the alloys was confirmed by using SPECTRO MAXx LMF04 optical emission spectroscopy (OES).

**Table 3.1 Chemical composition of Al-7.3Si and Al-12.1Si alloys.**

Si	Fe	Cu	Mn	Mg	Zn	Ni	Ti	Al
7.3	0.32	0.12	0.15	0.52	0.08	0.02	0.06	Rem
12.10	0.28	0.08	0.14	0.09	0.08	0.01	0.02	Rem



**Figure 3.1: Photograph of Al-7.3Si alloy**

### 3.2 Preparation of cast sample for MDF

The Al-7.3Si and Al-12.1Si alloy ingots (Figure 3.1) were melted in the furnace and then poured into a preheated metallic die of 32mm×32mm×100mm size to produce a cast sample of desired shape and dimension; die casting also reduces casting defects in the ingot. Figure 3.2 shows the casting die and cast sample. The electric resistance furnace has an automatic temperature controller with an accuracy of  $\pm 5$  °C. The crucible is cleaned and preheated before pouring the molten metal. Preheating



**Figure 3.2: Casting die with cast sample.**



**Figure 3.3: Al-7.3Si and Al-12.1Si samples for MDF Processing.**

temperature of casting die was maintained at around 250 °C. Molten metal was stirred with a graphite rod. Degassing tablets (hexachloroethane) were used to clear gas bubbles from molten metal. Coverall flux was applied to the molten metal to avoid surface oxidation. As-cast sample of 32mm×32mm×100mm size was cut and machined to required size for MDF processing. Dimensions of both Al-7.3Si and Al-12.1Si alloys are maintained differently depending on the amount of strain to be imposed. Al-7.3Si alloys were machined to dimensions of 30 mm x 30 mm x 24 mm for MDF processing with equivalent strain of 0.22. Similarly, Al-12.1Si alloy with dimensions of 30 mm x 30 mm x 23 mm was machined for MDF processing with an equivalent strain of 0.27. The strain is selected by trial-and-error method. Figure 3.3 shows the machined samples for MDF processing. The machined samples were then exposed to solution heat treatment at various temperatures and times. The purpose of solution heat treatment is to change the morphology of sharp-tipped eutectic silicon, which exists in as-cast structure of Al-Si alloys. These sharp-tipped silicon particles act as stress concentrators, causing localised shearing during plastic deformation at an early stage. Additionally, solution heat treatment minimises residual stresses (Li et al. 2015). Al-7.3Si alloy was solutionized at 535 °C for 10 hours, whereas Al-12.1Si alloy was solutionized for 3 hours at 525 °C, followed by water quenching. Subsequently, heat-treated samples were processed through MDF dies at room temperature using a Universal Testing Machine.

### **3.3 Multidirectional forging**

Figure 3.4 depicts the three-dimensional schematic view of multidirectional forging dies. MDF die set-up consists of the base plate and two split sections. Channels are provided to split sections of the MDF die. A pair of bolts and nuts are used to assemble the two split sections. Sample is inserted into the square channel of MDF die and forged with UTM through the plunger. Workpiece deforms plastically through the given space in the MDF die while under pressure. Free space or gap for the plastic flow of material depends on the amount of strain. Figure 3.5 shows a photograph of the MDF die along with the plunger. Solutionized samples were forged at room temperature using a 100-ton Universal Testing Machine. Figure 3.6 shows a photograph of the 100-ton UTM with MDF set-up. Molybdenum disulphide (MoS<sub>2</sub>) lubricant was used to minimise friction at the contact point of sample and die during MDF processing. An equivalent

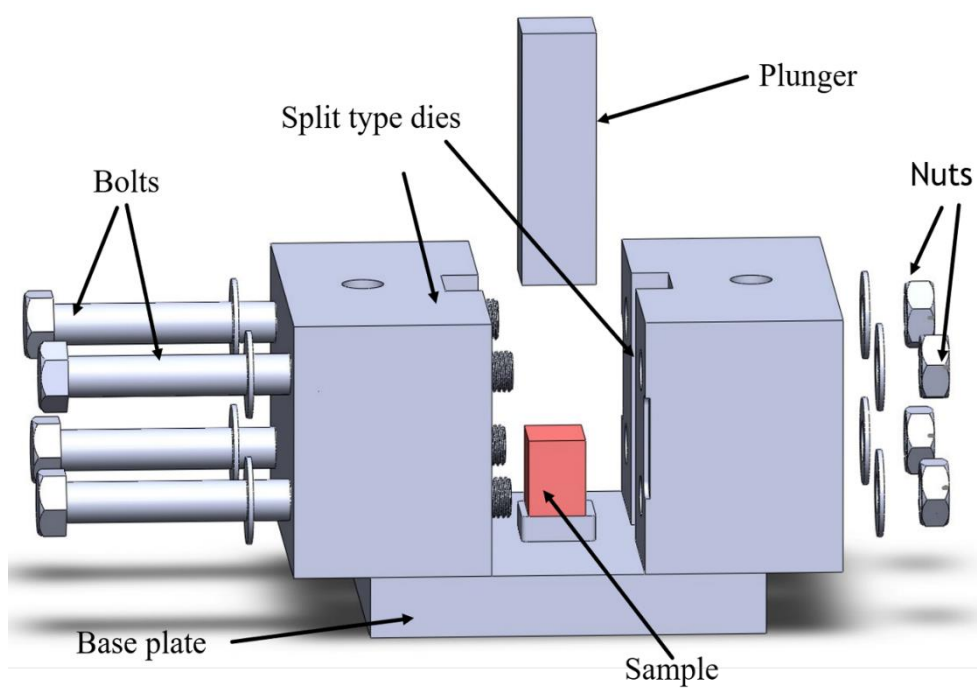


**Figure 3.4: Three-dimensional schematic view of the MDF die.**

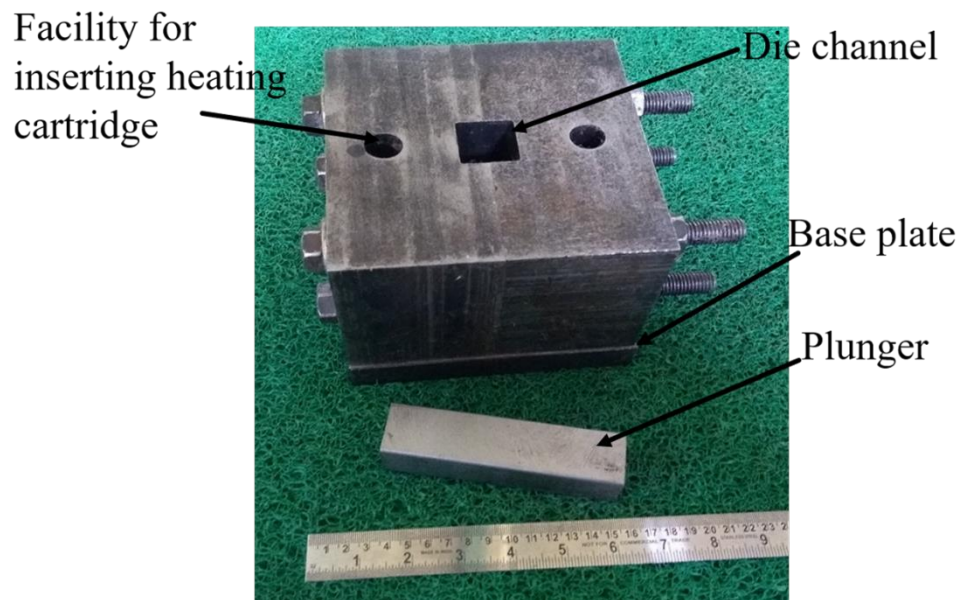


**Figure 3.5: MDF die assembly.**



**Figure 3.6:** Hydraulic press with MDF set up.

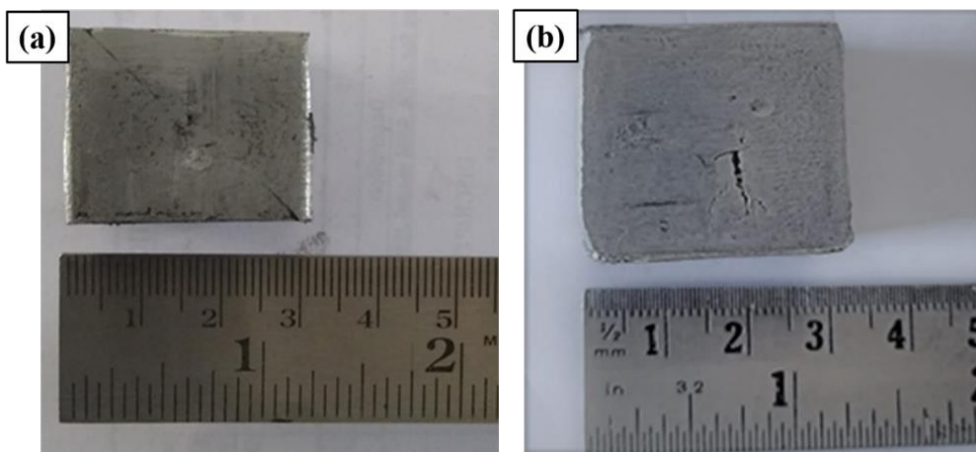


**Figure 3.7:** Fractured Al-7.3Si and Al-12.1Si alloys after seven and eleven passes through MDF at room temperature, respectively.

strain of 0.22 for Al-7.3Si alloys and 0.27 for Al-12.1Si alloys was maintained at each pass. Al-7.3Si and Al-12Si alloy have been successfully forged by MDF for two cycles with an equivalent strain of 0.22 and three cycles with an equivalent strain of 0.27, respectively. Further continued deformation of these alloys caused failure during forging, which is shown in Figure 3.7.

### **3.4 Material characterization**

#### **3.4.1 Optical Microscopy**

Optical microscope is used to magnify the images of small objects. These microscopes are also referred to as "light microscopes". Microstructure of MDF processed and unprocessed alloys were examined by a Carl-Zeiss optical microscope. A common metallographic procedure was used to prepare the specimen. The specimens were polished with alumina paste (2-5 $\mu$ m) and silicon carbide (SiC) abrasive sheets of 2000 grit. Keller's reagent (3 ml of hydrochloric acid, 2 ml of hydrofluoric acid, 25 ml of nitric acid, and 175 ml of water) was used to etch the specimens.

#### **3.4.2 Field emission scanning electron microscopy (FESEM)**

Carl Zeiss field emission scanning electron microscopy made in Germany (GeminiSEM 300 model) was used to study the wear micrographs of processed and unprocessed material. EDS examination of the samples was performed for elemental analysis of macro and micro constituents.

#### **3.4.3 X-Ray Diffractometry**

The X-ray diffractometer (Make: JEOL, Model: JPX 8) was employed to determine the phases of the alloys. XRD profiles were generated using a computer-controlled diffractometer with a nickel filter operating at 30 kV tube voltage and 20 mA current with Cu-K $\alpha$  radiation of 1.54 Å. For phase identification  $2\theta$  range was selected from 20° to 100°.

### **3.5 Mechanical characteristics**

#### **3.5.1 Microhardness measurement**

Hardness testing is a method of finding the resistance of a material to permanent deformation by penetrating harder material. Hardness testing is divided into two ranges: microhardness and macrohardness. Macrohardness test involves applying a load greater

than 1 kg, or roughly 10 N. The smaller samples, thin and plated samples are usually tested for microhardness with an applied load of less than 10 N. However, there is no scientific basis for selection of material for microhardness. In current work, material hardness is evaluated under microhardness testing. Microhardness of samples was measured using a Shimadzu Vickers microhardness tester (model: HMV-G20 ST). A hardness test was carried out on flat surface of sample with an applied load of 250 g for a 15-second dwell time. Conventional metallographic technique was applied to obtain flat surface. Microhardness measurements were performed at different locations in each sample, and values were obtained from the average of the measurements.

### 3.5.2 Tensile Testing

This test is used to evaluate tensile strength, yield strength, and ductility of materials. Tensile testing is a fundamental mechanical measurement to determine how long a material can withstand applied tensile forces before breaking. It measures the amount

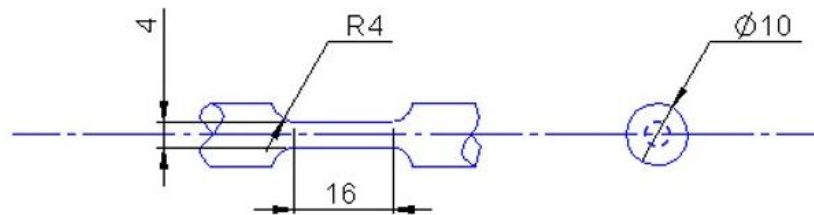


**Figure 3.8: Schematic diagram of the tensile test sample**

**(Note: All dimensions are in mm).**

of force required to break a specimen as well as how far the specimen stretches before breaking. Instron 30KN universal testing machine was employed to evaluate tensile strength of materials. Experiments were performed with a constant crosshead speed of 1 mm/min at room temperature. Specimens were machined for tensile testing in accordance with ASTM E-8 requirements. Figure 3.8 shows a schematic diagram of the tensile test sample. The SEM was employed to evaluate fracture surface morphology of tensile test samples.

### 3.5.3 Compression Testing

Compression tests were performed to determine flow curve, strength coefficient and strain hardening exponent according to the ASTM standard E9-09. The Shimadzu AG-

X plus™ universal testing equipment of 100 kN capacity was used to perform compression testing on the processed and unprocessed specimens. Cylindrical specimens with length-to-diameter ratio of 1.25 were machined from the processed and

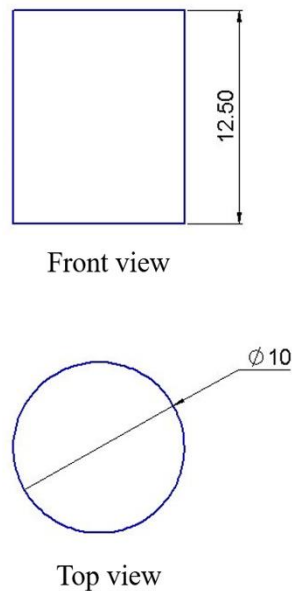


**Figure 3.9: Schematic diagram of the compression test sample (Note: All dimensions are in mm).**

unprocessed samples. Figure 3.9 depicts a schematic diagram of compression test sample. Tests were carried out at ambient temperature with a constant crosshead speed of 1 mm/min. Before the test, molybdenum disulphide (MoS<sub>2</sub>) was applied to the top and bottom surfaces of compression samples. From true stress ( $\sigma$ ) and true strain ( $\epsilon$ ) curves, material properties such as strength coefficient (K) and strain hardening exponent (n) were calculated by fitting the curve to Hollomon equation (Selin, M. 2010). It is described as given below,

$$\sigma = K \epsilon^n \quad \text{Equation 2}$$

### 3.5.4 Scratch Testing

Scratch test is the earliest conception of a mechanics of materials test for characterising properties. A single abrasive particle (indenter) comes into contact with the tested material during scratch test. Scratch-testing techniques give more basic information on

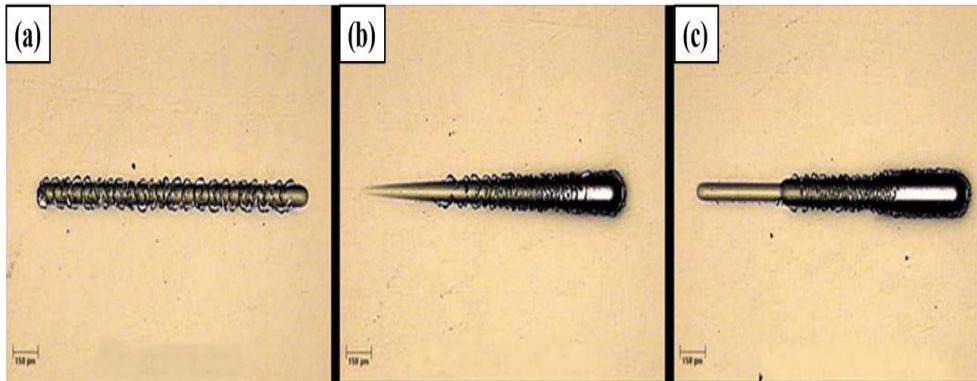


**Figure 3.10: Schematic diagram of three scratch modes: (a) constant load, (b) progressive load, and (c) incremental load (A. Onur Sergici Nicholas X. Randall 2006).**

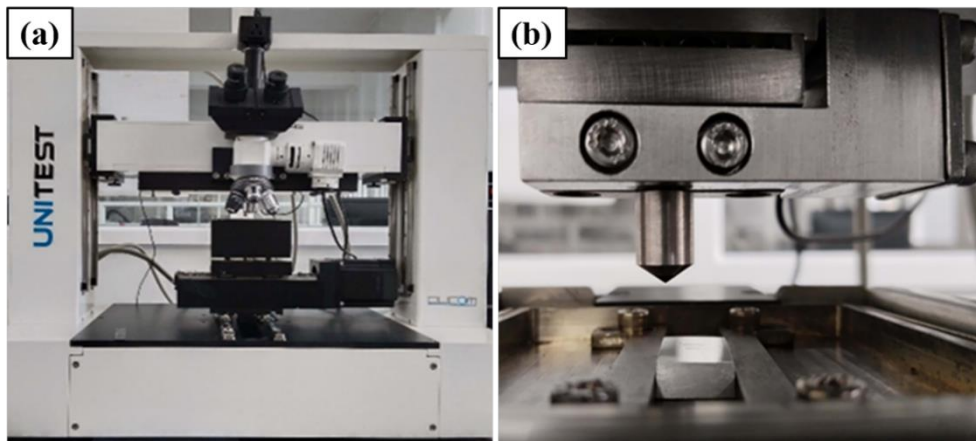


**Figure 3.11: a) photograph of scratch testing machine; (b) scratch testing machine with sample set up.**

wear mechanisms (Vencl et al., 2010). Scratch tests have two main uses: (a) determining how well a coating adheres, and (b) determining how well a surface resists being damaged by a harder opposing body. Scratch test involves simply ploughing and cutting the surface of a weaker material with a scratch device and quantifying scratch resistance through scratch hardness. Scratch testing has been used for many years to assess the resistance of materials to scratch. Scratch test consists of pressing a diamond stylus onto the surface, using either a constant, progressive, or increasing load against the sample, and moving with constant velocity, producing a scratch of a certain width and depth on the sample. In the constant-load scratch test, load is maintained at a constant level during the scratching of material. In incremental load, a scratch map can

be constructed to calculate the critical load associated with the specified damage by increasing load for each additional scratch. In progressive-load scratch testing, the indenter is moved along the sample while load is progressively increased to a predetermined maximum value. Normal load at which damage is first noticed is the critical load. If there is a shortage of space on the sample, incremental-load scratch testing, which consists of increasingly increasing constant-load scratch segments, is helpful. Figure 3.10 depicts these three distinct scratch test techniques. In the present work, a progressive load of 2–15 N was applied over a 5 mm distance at a speed of 1 mm/min. Tests were conducted at ambient temperature under dry sliding conditions. Stylus was cleaned before each scratch with a soft tissue soaked in acetone. Scratch tests were done to study the effectiveness of the multidirectional room-temperature forged Al-Si alloys on the resistance to fracture during indentation motion. Scratch tests were performed by using a DUCOM UNITEST scratch with a conical diamond tip, which is shown in Figure 3.11.

### **3.5.5 Wear testing**

Wear testing is done to characterize the wear performance of materials and to determine how differences in material properties can affect wear and friction. In addition, obtain basic information about the wear mechanisms occurring in the worn material. Wear test was conducted using a DUCOM pin-on-disc wear testing machine (model: TR-20LE-PHM 400-CHM 600) in accordance with the ASTM G99 standard. To analyse friction and wear in materials, the pin-on-disc testing machine was employed. Surface damage can be detected after some sliding, and wear debris can be observed both inside and outside the wear track. Figure 3.12 depicts the pin-on-disc wear testing machine that was used to evaluate the wear properties of the material. A stationary pin is forced against a rotating disc by the applied load in the test setup. Pin can be any shape, although due to the simplicity of alignment, cylinder or spherical (ball or lens) shapes are the most common. Test was conducted at room temperature and in dry conditions. Pins of 6 mm diameter were machined from the unprocessed and processed materials for the wear test and then made to slide against an EN31 steel disc (E52100) with a 120 mm track diameter throughout the experiment. Before each test, sample and disc surfaces were polished with silicon carbide emery paper and cleaned with acetone.

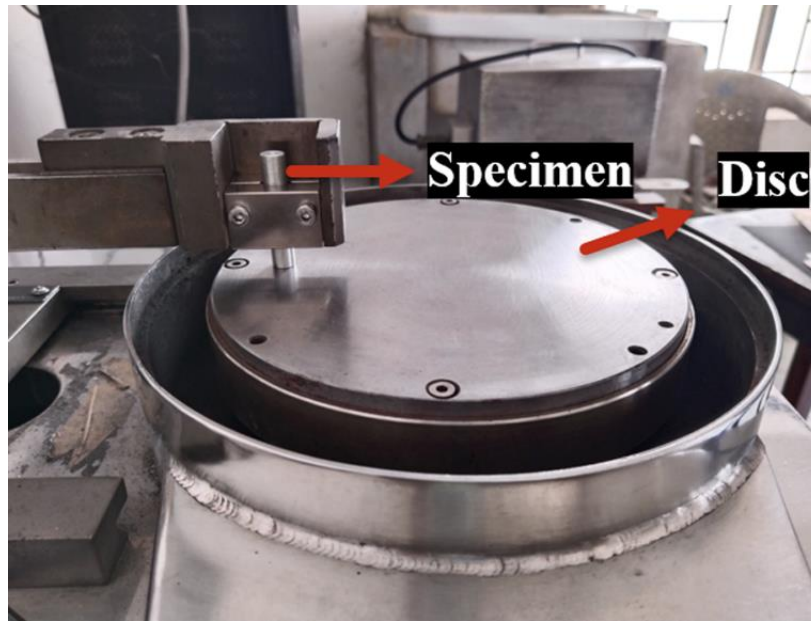


**Figure 3.12: photograph of pin on disc wear testing machine.**

**Table 3.2 Wear test conditions**

	<b>Condition 1</b>	<b>Condition 2</b>	<b>Condition 3</b>	<b>Condition 4</b>
<b>Load (N)</b>	19.61	39.23	19.61	39.23
<b>Sliding speed(m/s)</b>	0.7	0.7	2.2	2.2
<b>Sliding distance(m)</b>	1500	1500	1500	1500

Wear properties of the alloys have been tested with varying applied loads (19.61 N and 39.23N) and varying sliding speeds (0.7 m/s and 2.2 m/s) at a constant sliding distance of 1500 m. Table 3.2 represents wear testing conditions. Mass loss was measured based on the weight difference between the samples before and after test using a microbalance. Friction coefficient ( $\mu = F/N$ ) was calculated using frictional force data recorded on the computer and applied load. Field emission scanning electron microscopy (FESEM) was used to analyse the surface morphology and energy dispersive spectroscopy (EDS) of the worn surfaces of wear test specimens.



## CHAPTER 4

### RESULTS

The MDF-processed Al-7.3Si and Al-12.1Si alloys with different strains were emphasizing microstructural analysis, wear studies, tensile study, compression and hardness, etc. Details of the results are presented in this chapter.

#### 4.1 Microstructural characterization

##### 4.1.1 Al-7.3Si alloys

Figure 4.1 depicts optical micrograph of as-cast and solutionized Al-7.3Si alloy. Figure 4.1a shows microstructure of as-cast samples at lower magnification, which consists of dendrites of Al phase and network of eutectic Si particles. Figure 4.1 b depicts as-cast microstructure at higher magnification, which displays eutectic silicon in the form of acicular morphology with various shapes and sizes. Average length of acicular eutectic silicon particles is 17  $\mu\text{m}$  and average width is 1.9  $\mu\text{m}$ .

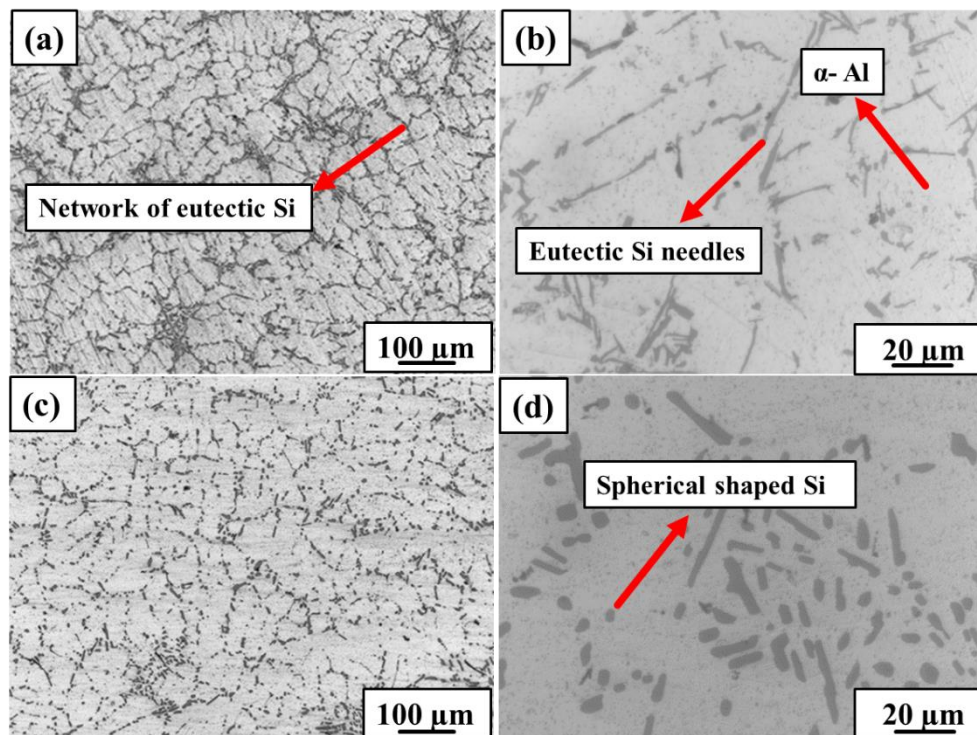


**Figure 4.1: Optical micrograph of Al-7.3Si alloys:  
(a, b) as-cast; (c, d) solutionized.**

Figures 4.1c and d show microstructure of solutionized sample at lower and higher magnifications. It can be noted that network of eutectic Si particles is almost broken after solutionizing. Figure 4.1d shows magnified view of solutionized microstructure exhibiting a morphological change in the eutectic silicon particles from coarse acicular eutectic silicon to spherical/ elongated with blunted tips. Furthermore, there is improved homogeneity of eutectic silicon distribution in Al phase, as can be observed in Figure 4.1c. Average length of eutectic Si particles is around 7.4  $\mu\text{m}$  and average width is 3.5  $\mu\text{m}$ .

Figure 4.2 illustrates microstructure of MDF-processed Al-7.3Si alloys at room temperature. Figures 4.2a and b show microstructure of one cycle of MDF-processed samples at lower and higher magnifications. According to microstructure, Si particles are broken into smaller particles of different sizes and shapes. Particle size is reduced to average length of 5  $\mu\text{m}$  and 3.2  $\mu\text{m}$  in width. Similarly, after two cycles, there is a significant change in microstructure, where Si particles are further effectively broken

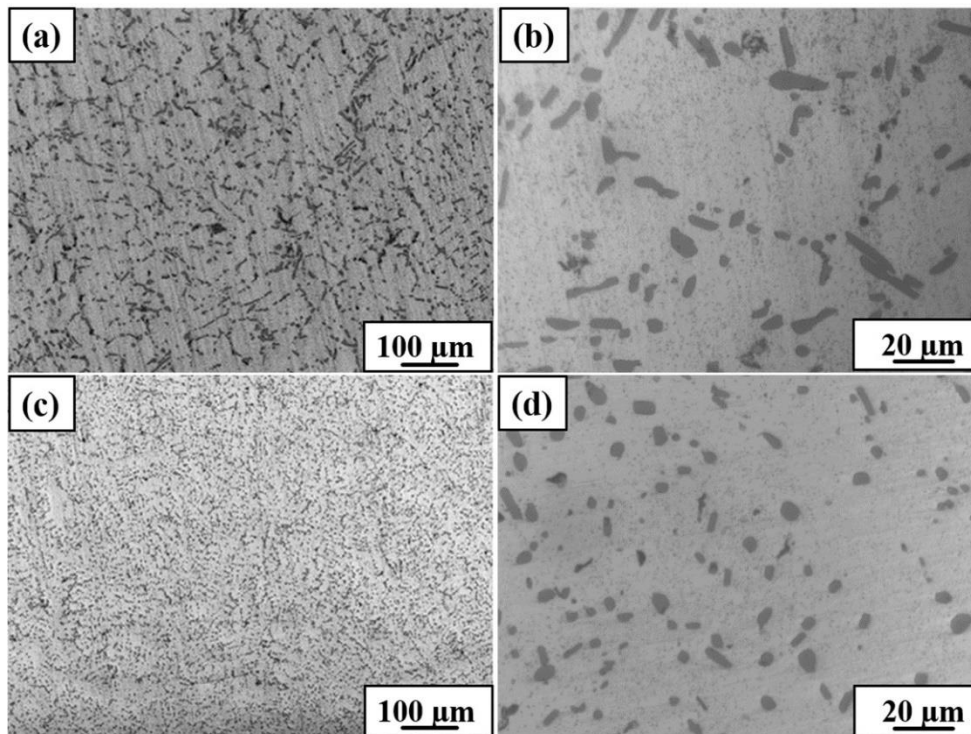


**Figure 4.2: Optical micrograph of Al-7.3Si alloys:  
(a, b) one cycle of MDF; (c, d) two cycles of MDF.**

into very fine particles and almost all silicon particles are redistributed uniformly, as shown in Figures 4.2c and d. Eutectic silicon particles are effectively broken into very fine particles with average length of 4  $\mu\text{m}$  and width of 2.5  $\mu\text{m}$ . Additionally, some silicon particles are broken down to less than two microns after two cycles of MDF. Furthermore, it is observed that when number of MDF cycles is increased, particle-free zones almost decrease.

#### 4.1.2 Al-12.1Si alloys

Figure 4.3 depicts microstructures of as-cast and solutionized Al-12.1Si alloys. In as-cast state (Figure 4.3a), microstructure consists of aluminium dendrites and networks of eutectic Si particles. Segregation of eutectic silicon particles resulting from dendritic solidification may have a negative effect on mechanical properties. Furthermore, clusters of eutectic silicon can be observed in the as-cast microstructure. A magnified view of microstructure delineates eutectic silicon in the form of sharp-edged plates with average size of 11.7  $\mu\text{m}$  in length and 2.6  $\mu\text{m}$  in width, as shown in Figure 4.3b.

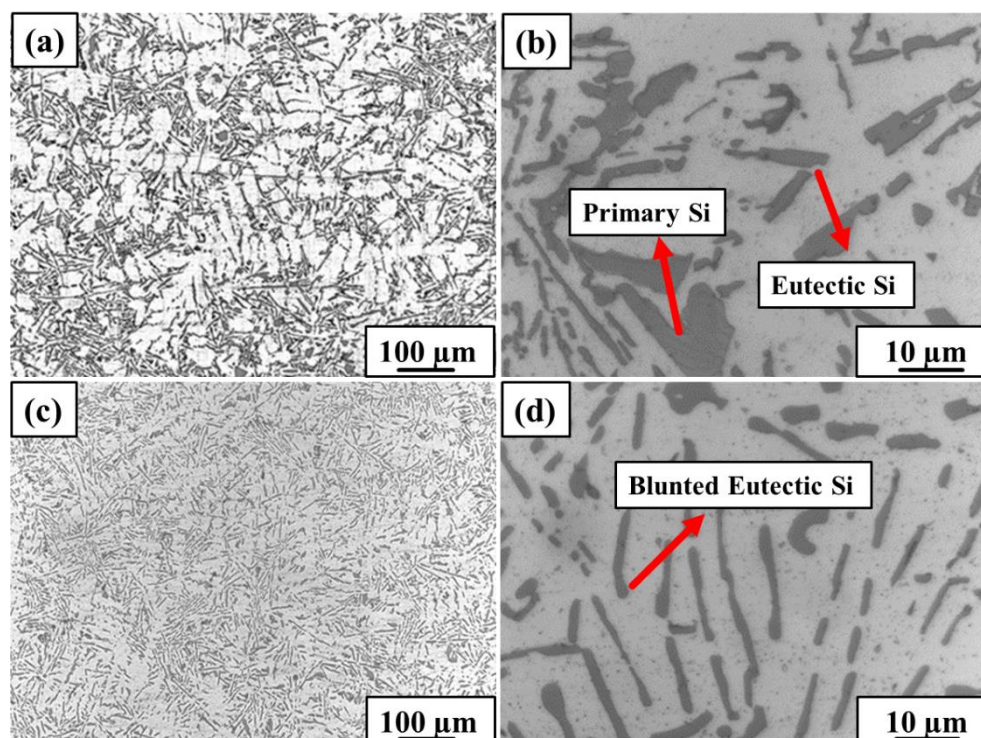


**Figure 4.3: Optical micrograph of Al-12.1Si alloys:  
(a, b) as-cast; (c, d) solutionized.**

Similarly, primary Si particles, with average size of 17  $\mu\text{m}$  in length, can also be seen in the as-cast microstructure. Limited primary Si particles in the microstructure are due to non-equilibrium cooling and slight variations in eutectic composition (Aktarer et al. 2015)( Purcek et al. 2010). Wang et al. (2012) have reported that Si atoms are easy to separate and form Si-Si clusters, which leads to formation of primary silicon even in eutectic or hypoeutectic Al-Si alloys. Sharp-edged eutectic Si plate morphology in microstructure is severely reducing ductility of Al-Si alloys. Figures 4.3c and d illustrate microstructure of solutionized sample at lower and higher magnifications. After solutionizing, dendrites of aluminium phase and network of eutectic silicon are decreased. Additionally, sharp-edged silicon particles of as-cast alloys are blunted after solutionizing, as shown in Figure 4.3d. Average length of eutectic Si particles is around 8.1  $\mu\text{m}$ , and average width is 2.1  $\mu\text{m}$  after solutionizing.

Figures 4.4a and b show microstructure of one-cycle MDF-processed Al-12.1Si alloy at lower and higher magnifications, respectively. After one cycle, average length of eutectic Si particles is reduced to 5.3  $\mu\text{m}$  and average width of 1.8  $\mu\text{m}$ . However,

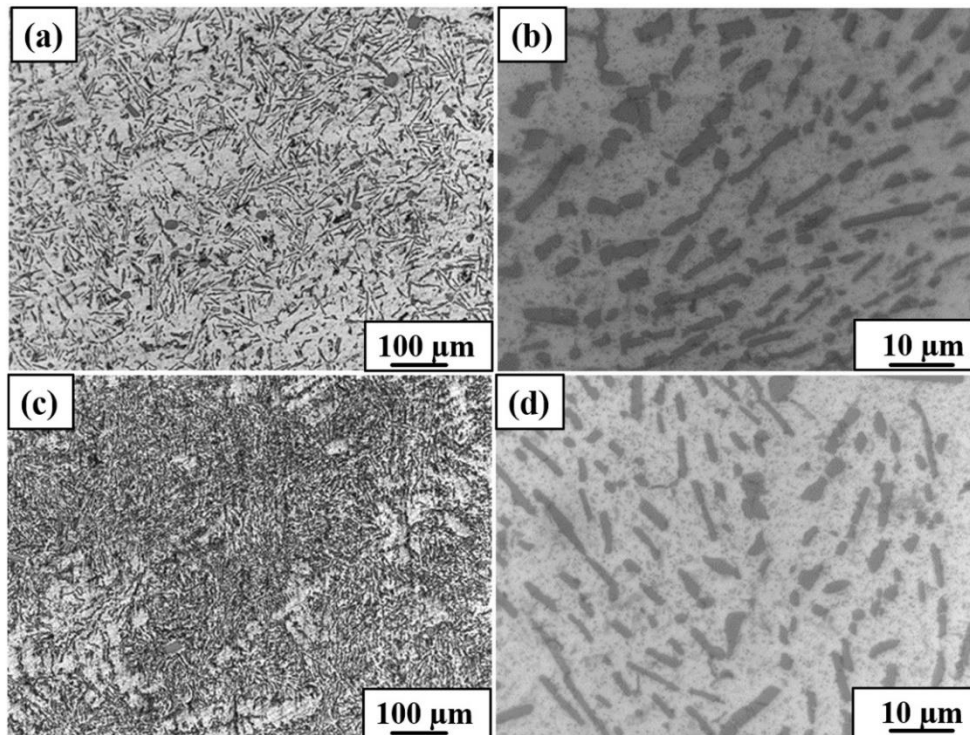


**Figure 4.4: Optical micrograph of Al-12.1Si alloys:  
(a, b) one cycle of MDF; (c, d) two cycles of MDF.**

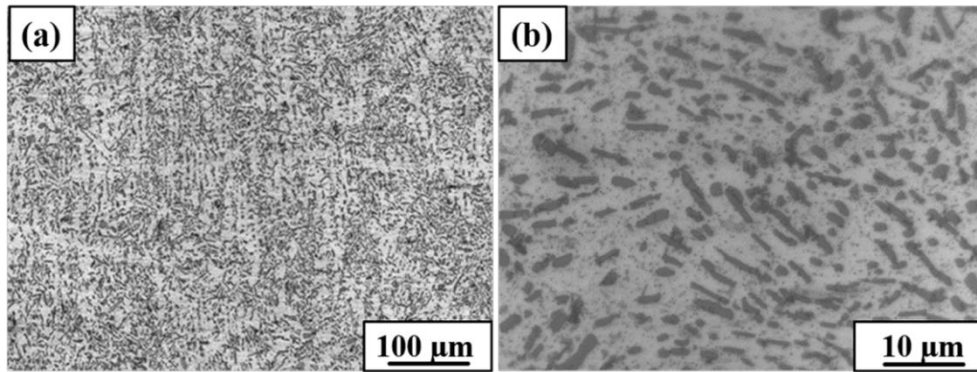


**Figure 4.5: Optical micrograph of Al-12.1Si alloys: (a, b) three cycles of MDF.**

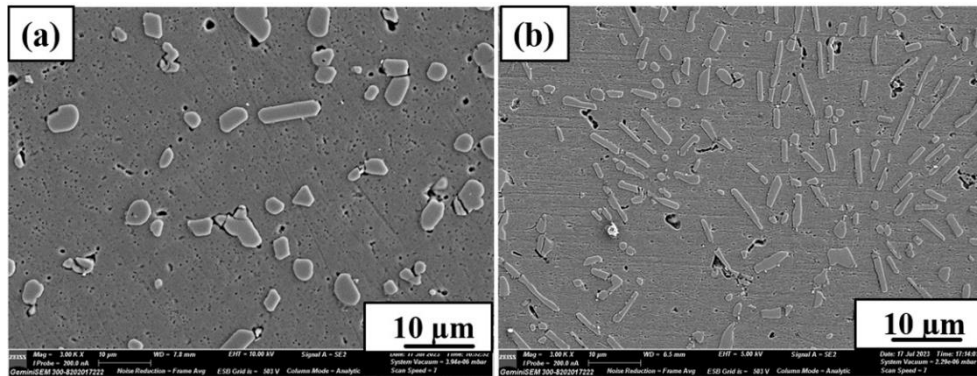


**Figure 4.6: FESEM micrograph of MDF processed Al-7.3Si with two cycles and Al-12.1Si alloy with three cycles of MDF.**

particle refinement is not efficient with one cycle of MDF. Figures 4.4c and d show microstructure of two cycles of MDF-processed Al-12.1Si alloy at lower and higher magnifications, respectively. It can be observed from the figure that with increasing MDF cycles, the silicon particles are further broken down into smaller particles, and their distribution in the aluminium phase improves. Average length of eutectic Si particles is reduced to 4.6  $\mu\text{m}$  and average width of 1.2  $\mu\text{m}$ . After three cycles of MDF (Figure 4.5), remarkable changes in the microstructure with fine and uniform silicon particles are observed. Average length of eutectic Si particles is reduced to around 2.8  $\mu\text{m}$  and average width is 1.1  $\mu\text{m}$ . Furthermore, some silicon particles are reduced to less than two microns in size. Microstructure of three-cycle processed samples shows evenly distributed fine silicon particles across aluminium phase, with reduced particle-free zones in tested samples. Figure 4.6 depicts FESEM image of finely broken silicon particles in Al-7.3Si alloy with two cycles of MDF and Al-12.1Si alloy with three

cycles. It is observed that combined solutionizing and MDF led to significant improvement in the microstructure. The roundness of the Si particle edge is result of solutionizing. The coarse eutectic silicon particles are fragmented into fine particles and more uniformly distributed in the aluminium phase matrix compared to the as-cast sample. This is attributed to the intense plastic deformation with increasing MDF passes on the Al-base, which carries the silicon particles. It can be observed that some silicon particles are finely broken in the Al-12.1 alloy with three-pass sample compared to the Al-7.3Si alloy with two-pass sample.

Figures 4.7 and 4.8 depict the graph of average silicon particle size of Al-7.3Si and Al-12.1Si alloy under different processing conditions. It can be seen that size of eutectic silicon particles decreases as the number of MDF cycles increases. High applied strain causes the Si particles to fragment, which results in decreased silicon particle size during MDF process. During MDF processing, high strain is transmitted to eutectic silicon particles via Al phase. Since eutectic Si particles are very brittle and non-formable, they cannot withstand plastic deformation of the surrounding aluminium. For this reason, eutectic silicon particles are fractured during plastic deformation, especially at room temperature. Additionally, it can be seen that decreasing trend of eutectic particle length is greater than reduction of particle width. This is because high strain introduced during the MDF processing causes Si particles to break easily in the direction of length. Figures 4.9 and 4.10 show the graph of average number of Si particles of Al-7.3Si and Al-12.1Si alloys with different processing conditions. Number of silicon particles is calculated using average of silicon particles from three microstructure images. From the graph (Figures 4.9 and 4.10), It can be shown that as-cast samples have fewer silicon particles and more variance in their number. Additionally, with increasing number of MDF cycles, the number of silicon particles for the given area increased. According to microstructure, inter-particle distance of hard Si particles is greatly reduced after MDF process, indicating that the particle-free zone is significantly reduced. Therefore, these results show that the multidirectional forging process at room temperature has a significant impact on the refinement of hard silicon particles and their distribution. Increasing number of MDF cycles leads to better uniformity of silicon particles in aluminium phase, and particles become finer.

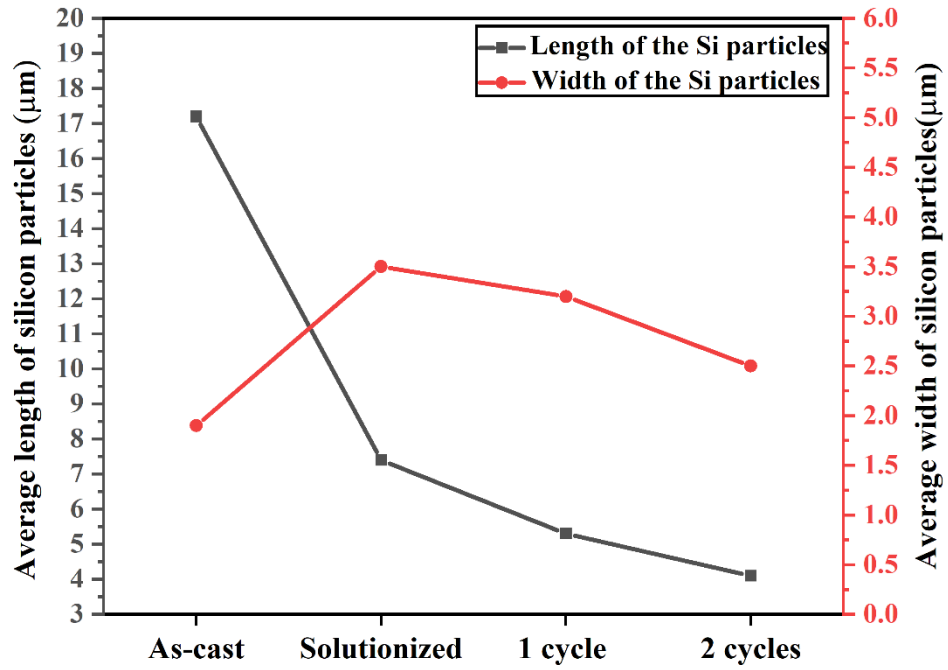


**Figure 4.7: Average silicon particle size of Al-7.3Si alloy under the different processing conditions.**

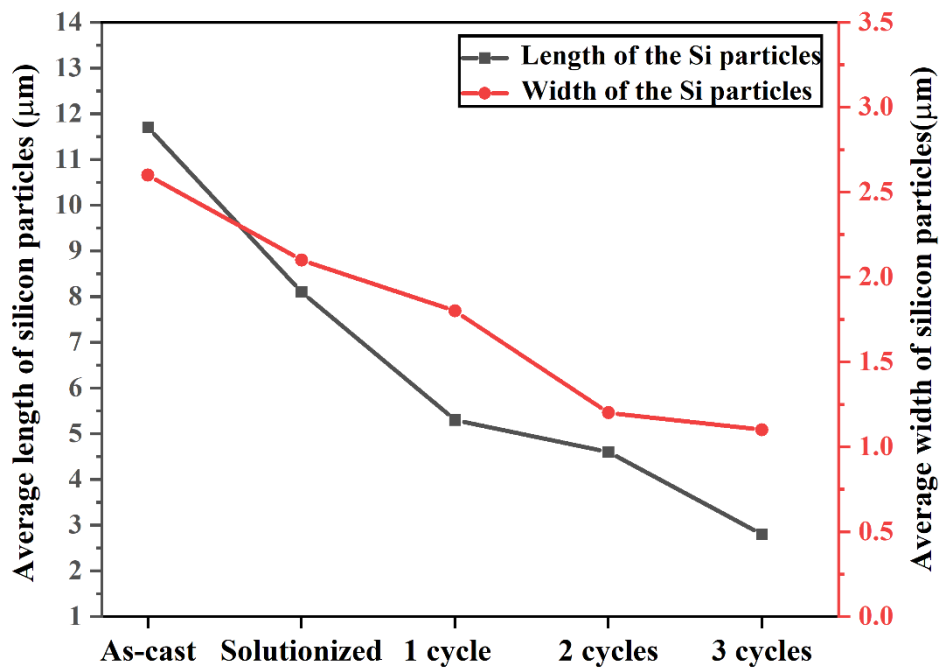


**Figure 4.8: Average silicon particle size of Al-12.1Si alloy under the different processing conditions.**

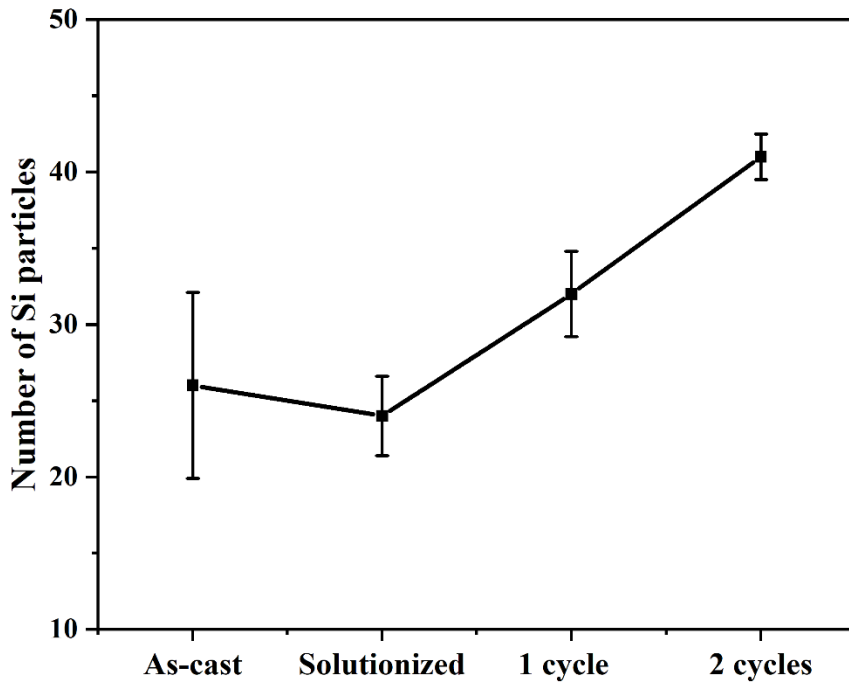


**Figure 4.9: Average number of Si particles of Al-7.3Si alloy under the different processing conditions.**

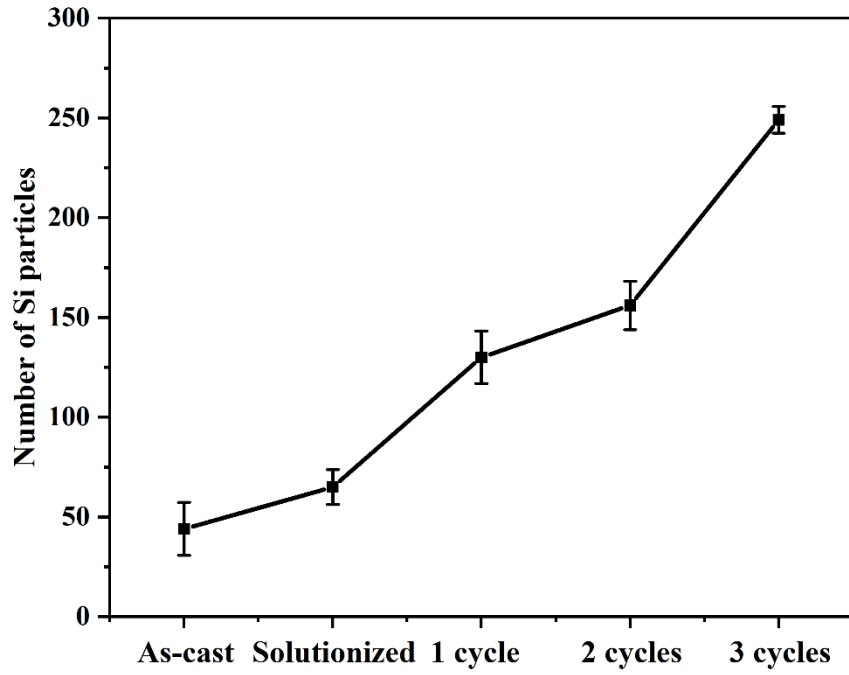


**Figure 4.10: Average number of Si particles of Al-12.1Si alloy under the different processing conditions.**

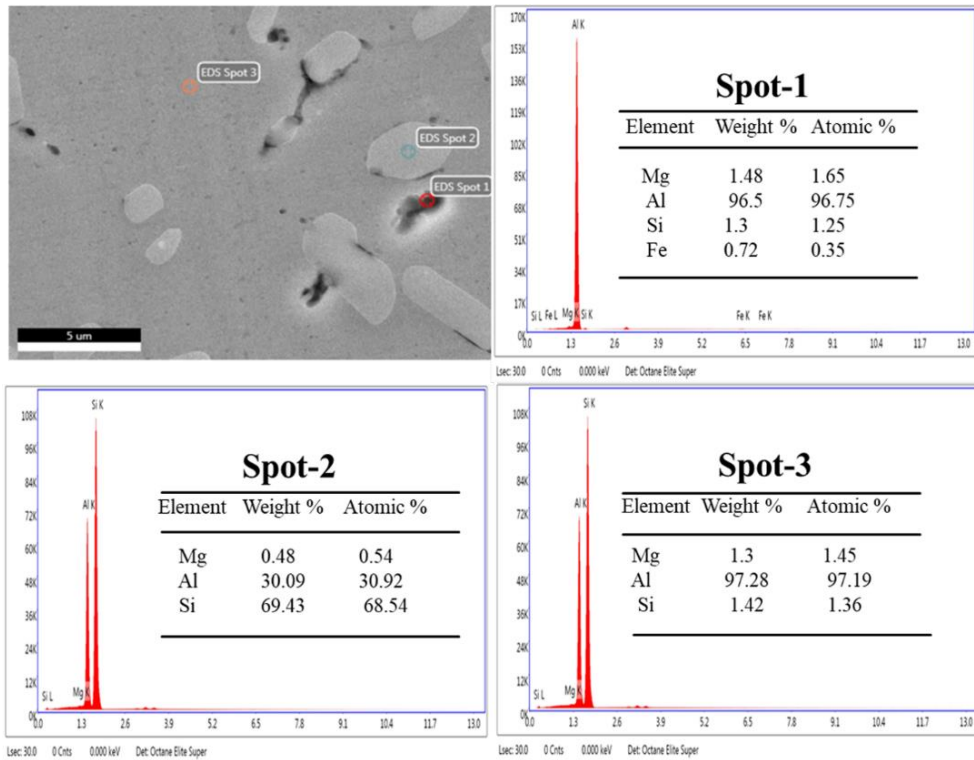


Figure 4.11: SEM image and EDX of solutionized Al-7.3Si alloy.

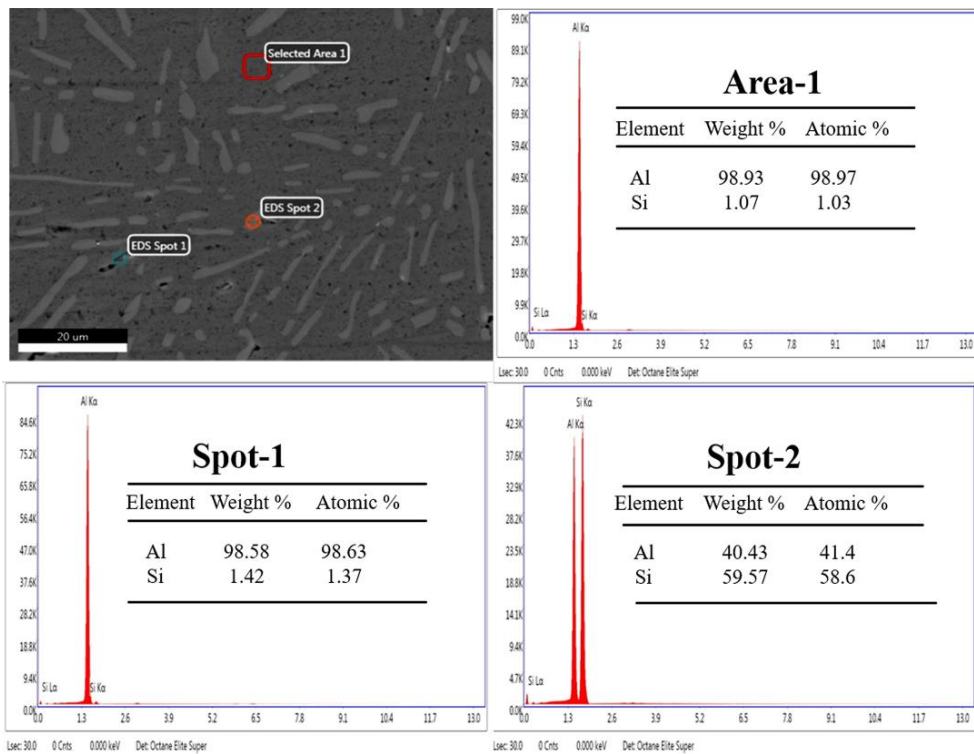
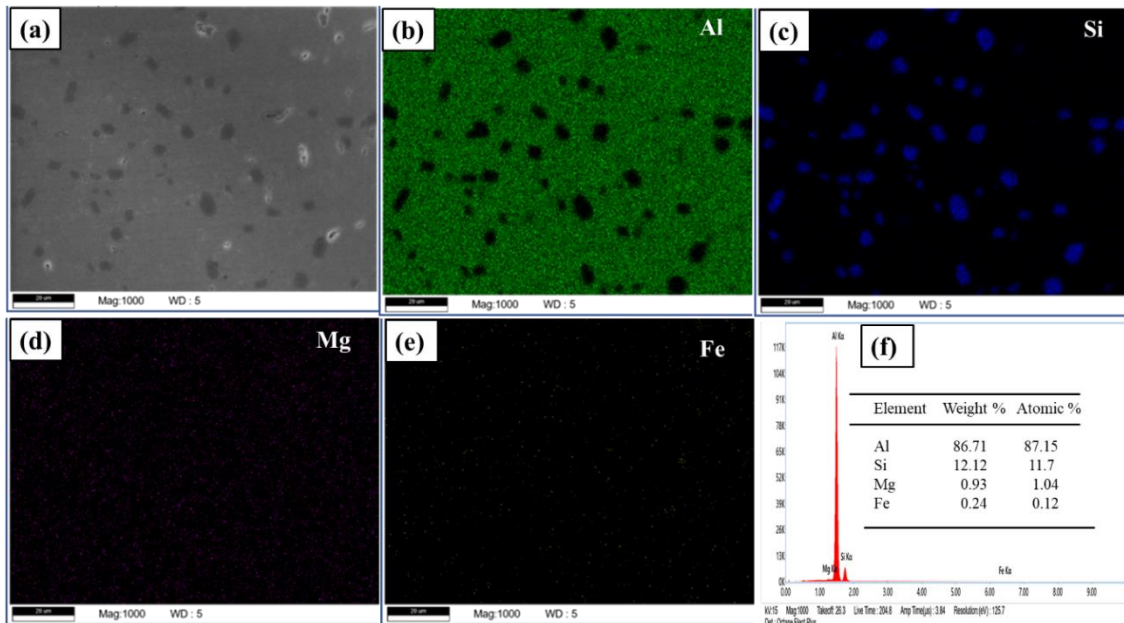
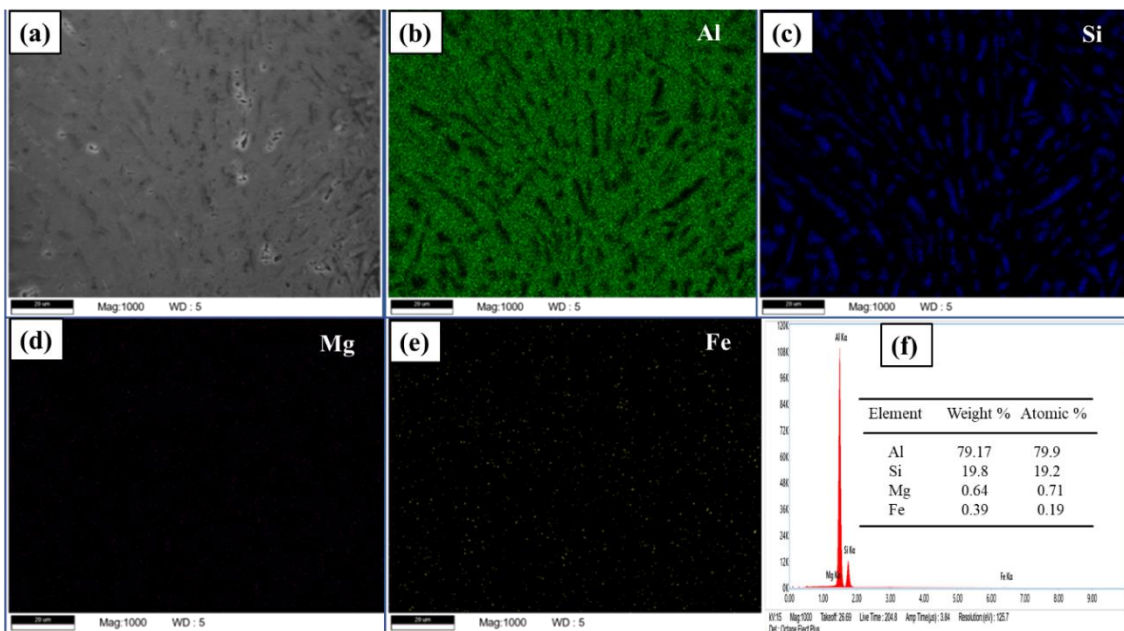


Figure 4.12: SEM image and EDX of solutionized Al-12.1Si alloy.



**Figure 4.13: Elemental mapping of two cycles of MDF processed Al-7.3Si alloy: a) FESEM image; b) Al; c) Si; d) Mg; e) Fe; f) weight and atomic percentage of various elements.**



**Figure 4.14: Elemental mapping of three cycles of MDF processed Al-12.1Si alloy: a) FESEM image; b) Al; c) Si; d) Mg; e) Fe; f) Weight and atomic percentage of various elements.**

The composition of Al-7.3Si and Al-12.1Si alloys was analysed by energy dispersive X-ray and confirmed the presence of Al and Si elements, as depicted in Figures 4.11 and 4.12. Figures 4.13 and 4.14 show elemental maps of MDF-processed Al-7.3Si alloy with two cycles and Al-12.1Si alloy with three cycles. From Figure 4.13, it can be observed that Al and Si are major elements with small percentage of Mg in Al-7.3Si alloys. In the Al-12.1Si alloy, Al and Si are the major elements, with trace amounts of Fe, and Mg elements. Elemental mapping of Si shows significant refinement and uniform distribution of Si particles in the aluminium phase matrix, which can be observed in both MDF-processed Al-Si alloys. Additionally, silicon networks are completely broken in both MDF-processed alloys. More small fragmented Si particles can be observed in the Al-12.1Si alloy with three cycles compared to the Al-7.3Si alloy with two cycles. Tables 4.1 and 4.2 show summary of the silicon particle sizes of Al-7.3Si and Al-12.1Si alloys under various processing conditions.

**Table 4.1: Summary of Silicon particle size of Al-7.3Si alloys in various conditions**

Conditions	Average length Si particles	Average width Si particles
As-cast	17.2 $\mu\text{m}$	1.9 $\mu\text{m}$
solutionizing	7.4 $\mu\text{m}$	3.5 $\mu\text{m}$
One cycle	5 $\mu\text{m}$	3.2 $\mu\text{m}$
Two cycles	4 $\mu\text{m}$	2.5 $\mu\text{m}$

**Table 4.2: Summary of Silicon particle size of Al-12.1Si alloys in various conditions**

Conditions	Average length Si particles	Average width Si particles
As-cast	11.7 $\mu\text{m}$	2.6 $\mu\text{m}$
solutionizing	8.1 $\mu\text{m}$	2.1 $\mu\text{m}$
One cycle	5.3 $\mu\text{m}$	1.8 $\mu\text{m}$
Two cycles	4.6 $\mu\text{m}$	1.2 $\mu\text{m}$
Three cycles	2.8 $\mu\text{m}$	1.1 $\mu\text{m}$

## 4.2 X-ray diffraction analysis

Figures 4.15 and 4.16 depict the XRD patterns of Al-7.3Si and Al-12.1Si alloys containing  $\alpha$ -Al and eutectic silicon phases, respectively. Measurements were scanned for a wide range of diffraction angles ( $2\theta$ ) ranging from 20 to 100 degrees for phase identification. The diffraction peaks corresponding to (111), (200), (220), (311), (222), and (400) planes belonging to aluminium phase along with some weak peaks corresponding to (111), (220), (311), (331), and (422) planes belonging to eutectic silicon (Shaw et al. 2016). Based on the correlation between crystallite size and strain, the following equation could be applied:

$$\beta_T = \beta_D + \beta_\varepsilon \quad \text{Equation 3}$$

Where  $\beta_T$  is the total peak broadening,  $\beta_D$  is broadening due to crystallite size and  $\beta_\varepsilon$  is the broadening due to strain.

From the Scherrer equation (Zak et al. 2011), we know that

$$D = \frac{K\lambda}{\beta_D \cos\theta} \quad \text{Equation 4}$$

Or

$$\beta_D = \frac{K\lambda}{D \cos\theta} \quad \text{Equation 5}$$

Where  $\beta_D$  is the full-width at half-maximum (i.e., broadening of the peak) in radians,  $K = 0.9$  is the shape factor,  $\lambda = 0.15406$  nm is the wavelength of X-ray source,  $D$  is the crystallite size and  $\theta$  is the peak position in radians.

Similarly, the XRD peak broadening due to microstrain is given by,

$$\beta_\varepsilon = 4 \varepsilon \tan\theta \quad \text{Equation 6}$$

Where  $\beta_\varepsilon$  is broadening due to strain,  $\varepsilon$  is the strain and  $\theta$  is the peak position in radians.

Putting equation (5) and (6) in equation (3), we get,

$$\beta_T = \frac{K\lambda}{D \cos\theta} + 4 \varepsilon \tan\theta \quad \text{Equation 7}$$

The equation (7) can be written as

$$\beta_T \cos\theta = \frac{\kappa\lambda}{D} + 4 \varepsilon \sin\theta \quad \text{Equation 8}$$

Equation (8) is the Williamson–Hall equation. The intercept of the plotted  $\beta_T \cos\theta$  versus  $4 \sin\theta$  gave the crystallite size while the slope gave strain. Both crystallite size and micro-strain are obtained by the Williamson–Hall method. Tables 4.3 and 4.4 show peak broadening in terms of FWHM, crystallite size, and micro-strain value of processed and unprocessed Al-Si alloys. From the tables, it can be observed that the peak broadening (FWHM) of aluminium phase and eutectic silicon phases increased in the case of MDF-processed samples with cumulative strains of 1.3 (two cycles) and 2.43 (three cycles) compared to as-cast samples. Peak broadening of aluminium phase and eutectic silicon phases in the XRD pattern could be influenced by grain size refinement, reduction in particle size, and macro-strain. From the tables, it can be noted that MDF-processed samples showed increased micro-strain compared to as-cast

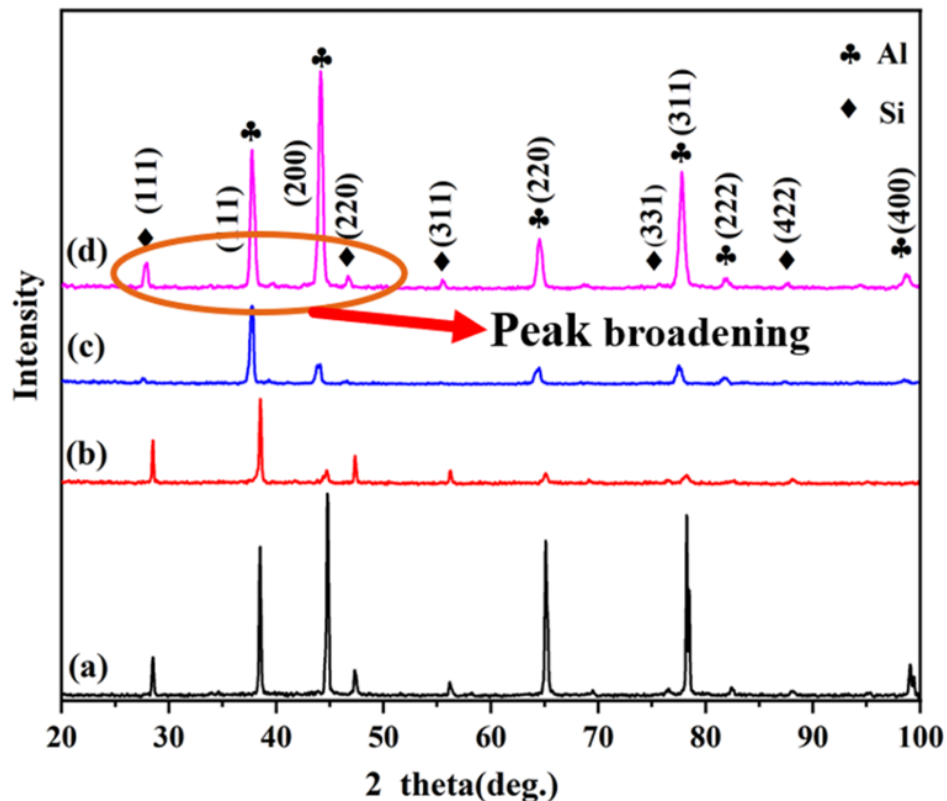


**Figure 4.15: XRD patterns of Al-7.3Si alloy: (a) as-cast; (b) solutionized; (c) one cycle; and (d) two cycles.**

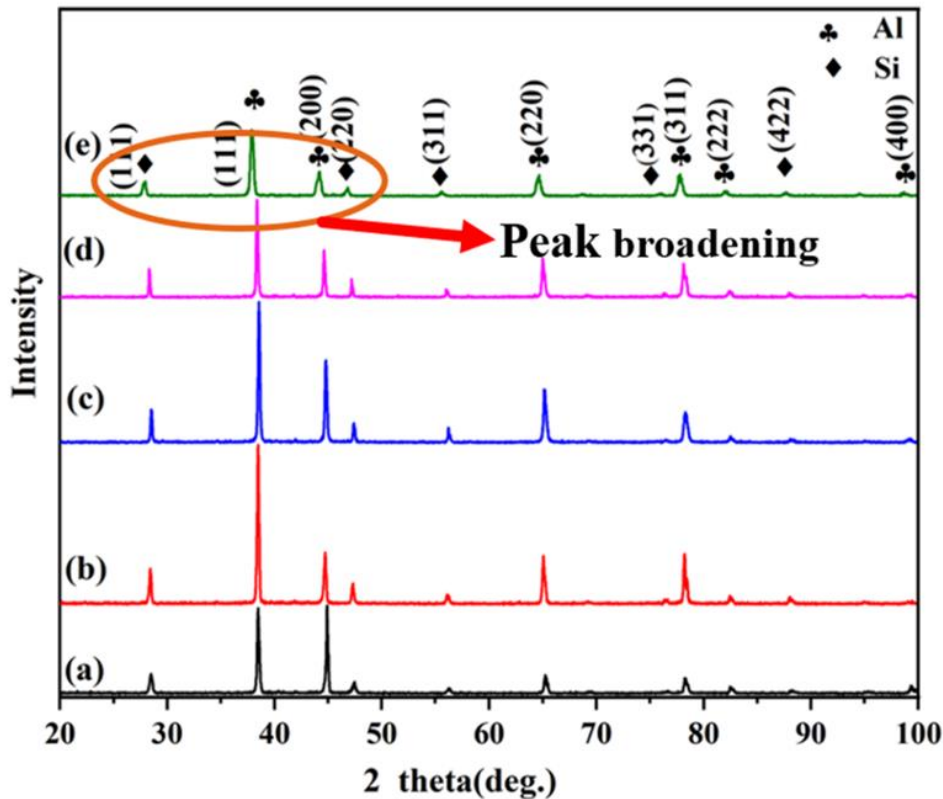


**Figure 4.16: XRD patterns of Al-12.1Si alloy: (a) as-cast, (b) solutionized, (c) one cycle (d) two cycles (e) three cycles.**

samples. Similarly, the crystallite size of MDF-processed samples in both alloys was reduced when compared to as-cast samples due to higher imposed strain. Therefore, the combined effect of crystallite size and micro-strain is responsible for the peak broadening. Peak shifts and intensity variations of the peaks can be observed in MDF-processed XRD pattern of Al-7.3Si and Al-12.1Si alloys. Peak shifts and intensity variations might be due to strain in the MDF sample (Ramesh et al., 2019). Preferred orientation of crystals is potential reason for change in intensity of the peaks (Wanga et al., 2015). In the XRD profile of Al-7.3Si alloys, aluminium phase shifted in the  $2\theta$  values from 38.49 in solutionized samples to 37.69 after two cycles. Similarly, in the XRD profile of Al-12.1Si alloys, the aluminium phase shifted slightly in the  $2\theta$  values from 38.46 in the solutionized sample to 37.88 after three cycles. This peak shift is result of strain developed in the materials after MDF processing at room temperature (Rajender and Giri 2016).

**Table 4.3: Microstructural parameters of the Al–7.3Si samples calculated from XRD patterns via Williamson-Hall method.**

Processing condition	FWHM $2\theta(\text{Al})$ $\beta_{hkl}(\text{°})$	FWHM $2\theta(\text{Si})$ $\beta_{hkl}(\text{°})$	Crystallite Size D (nm)	Micro-strain $\epsilon$ (%)
As-cast	0.07872	0.15744	167	0.147
Solutionized	0.11808	0.23616	127	0.27
MDF 1 cycle	0.35424	0.47232	82	0.25
MDF 2 cycle	0.43296	0.62976	45	0.20

**Table 4.4: Microstructural parameters of the Al–12.1Si samples calculated from XRD patterns via Williamson-Hall method.**

Processing condition	FWHM $2\theta(\text{Al})$ $\beta_{hkl}(\text{°})$	FWHM $2\theta(\text{Si})$ $\beta_{hkl}(\text{°})$	Crystallite Size D (nm)	Micro-strain $\epsilon$ (%)
As-cast	0.15744	0.21648	101	0.055
Solutionized	0.11808	0.23616	199	0.046
MDF 1 cycle	0.13776	0.3936	120	0.161
MDF 3 cycle	0.47232	0.47232	78	0.341

### 4.3 Mechanical Properties

#### 4.3.1 Microhardness

Vickers microhardness measurements are performed at various locations on the sample surfaces, and values are obtained from average of these measurements. Figure 4.17 shows variation in hardness of as-cast, solutionized, and MDF-processed Al-7.3Si alloys. In as-cast condition, hardness of the alloy is around  $78.4 \pm 6.2$  Hv. After solutionizing, hardness is increased to  $89.3 \pm 2.9$  Hv. A noticeable improvement in hardness of the alloy can be observed after solutionizing. Similarly, hardness values for MDF-processed one and two cycles are  $95 \pm 1.6$  Hv and  $125 \pm 1.3$  Hv, with cumulative strains of 0.66 and 1.32, respectively. After two cycles of MDF processing, hardness significantly increased and showed maximum value compared to the other processing conditions. Hardness value increased from 78.4 Hv (for as-cast sample) to 125 Hv (after

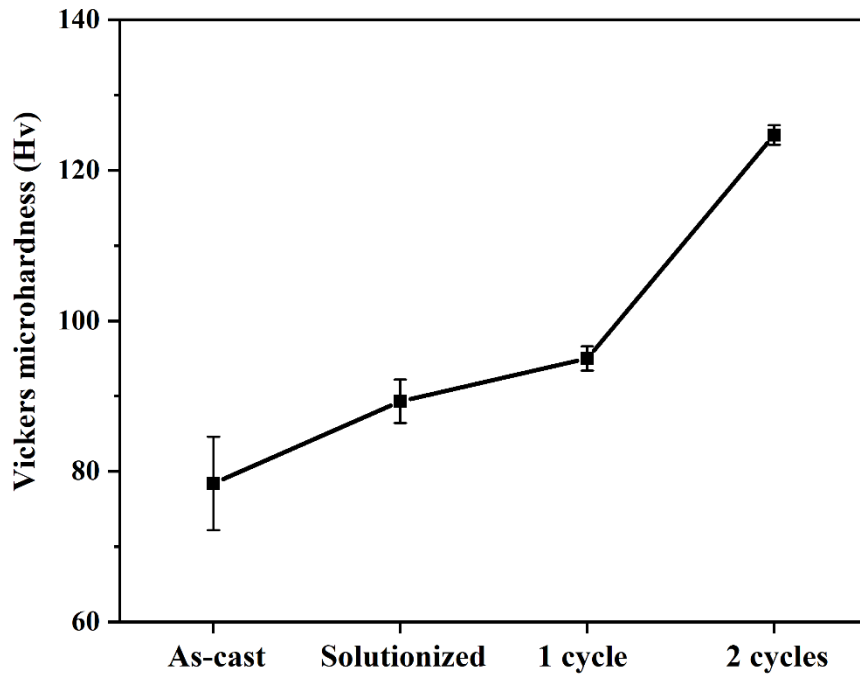


**Figure 4.17: Micro-hardness of the as-cast, solutionized and MDF processed Al-7.3Si samples.**

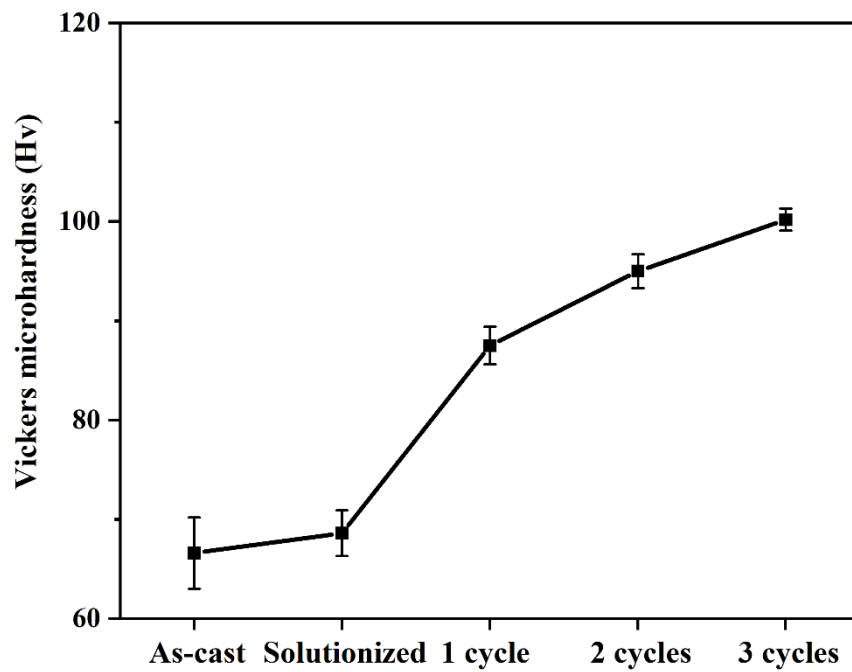


**Figure 4.18: Micro-hardness of the as-cast, solutionized and MDF processed Al-12.1Si samples.**

two cycles of MDF) and registered a 60% increment in Al-7.3Si alloys. Figure 4.18 represents hardness of as-cast, solutionized, and MDF-processed Al-12.1Si alloys. Hardness of as-cast samples is around  $66.6 \pm 3.5$  Hv. After solutionizing, hardness is slightly increased to  $68.6 \pm 2.3$  Hv. In comparison to Al-7.3Si alloys, Al-12.1Si alloys showed a lower hardness value after solutionizing. Similarly, hardness values of one and two cycles of MDF processing were  $87.5 \pm 2$  Hv and  $95.5 \pm 1.7$  Hv, with cumulative strains of 0.81 and 1.62, respectively. After three cycles of MDF processing, hardness reached  $100.2 \pm 1$  Hv with cumulative strains of 2.43. Hardness of MDF-processed three-cycle samples shows maximum value compared to the other processing conditions. In Al-12.1Si alloys, hardness value increased from 66.6 Hv (for as-cast sample) to 100.2 Hv (after third cycle of MDF) and registered a 50% increment. From the results, Al-7.3Si alloys with two cycles of forging showed greater hardness compared to Al-12.1Si alloys with three-cycle forging.

#### **4.3.2 Tensile properties**

Figure 4.19 displays stress-strain graphs of as-cast, solutionized and MDF-processed Al-7.3Si alloys. Figure 4.20 illustrates tensile strength and elongation to failure of Al-7.3Si alloys as a function of different processing conditions. Ultimate tensile strength and percentage elongation of as-cast specimens are 177 MPa and 7.5%, respectively. After solutionizing, UTS and percentage elongation of the specimen reached 298 MPa and 11.7%, respectively, which are greater than that of as-cast alloys. Ultimate tensile strength and percentage elongation of MDF processed up to one cycle are 373 MPa and 5.5%, respectively. After processing for up to two cycles, ultimate tensile strength and percentage elongation reach 441 MPa and 5.6%, respectively. The UTS is achieved for MDF-processed two-cycle specimens, which is approximately 149% higher than that of cast alloys. Similarly, Figure 4.21 shows the stress-strain graph of as-cast, solutionized, and MDF samples of Al-12.1Si alloys. Figure 4.22 depicts the tensile strength and elongation to failure of Al-12.1Si alloy as function of different processing conditions. As shown in Figure 4.22, cast specimens show UTS of 192 MPa and percentage elongation of 5.6%. Solutionized sample shows increase in ductility of 7.7% in addition to strengthening up to 208 MPa. However, strength and ductility achieved in Al-12.1Si alloys are lower compared to Al-7.3Si alloys after solutionizing. Tensile

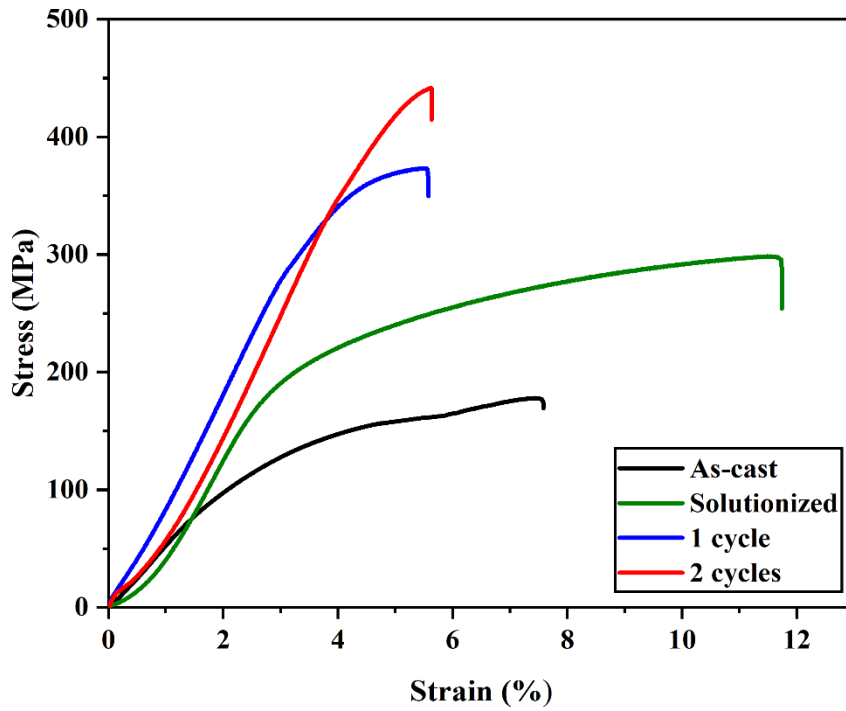


Figure 4.19: Stress–strain curves of as-cast, solutionized, and MDF-processed Al-7.3Si alloy.

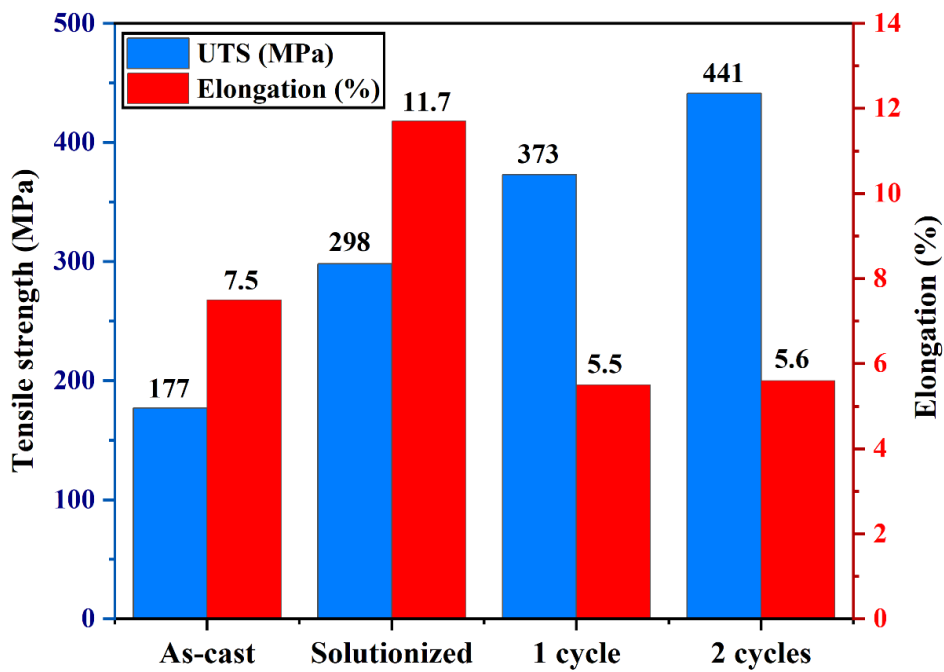


Figure 4.20: Strength-elongation bar chart of Al-7.3Si alloy in different processing conditions.

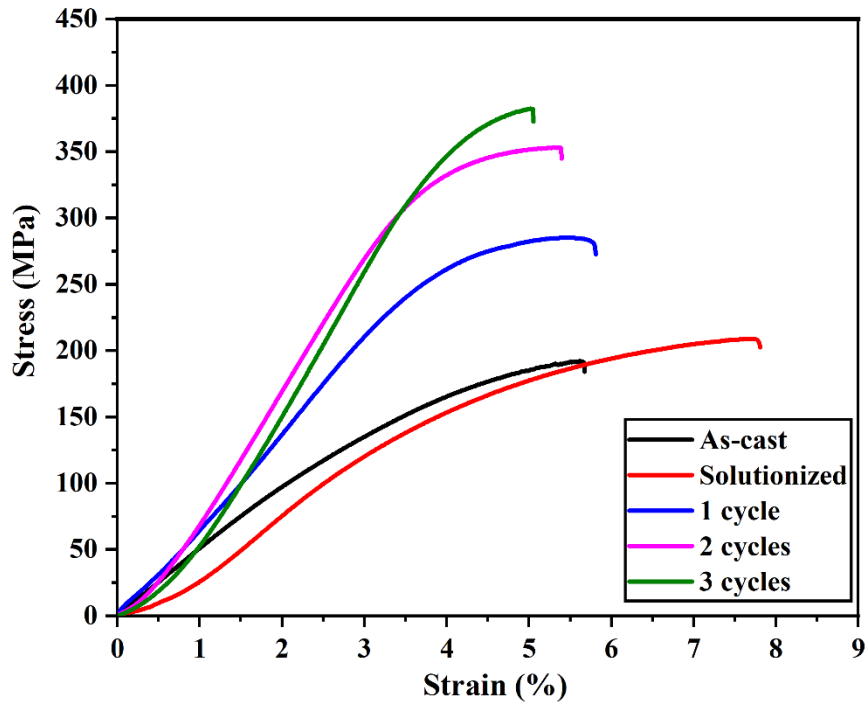


Figure 4.21: Stress–strain curves of as-cast, solutionized, and MDF-processed Al-12.1Si alloy.

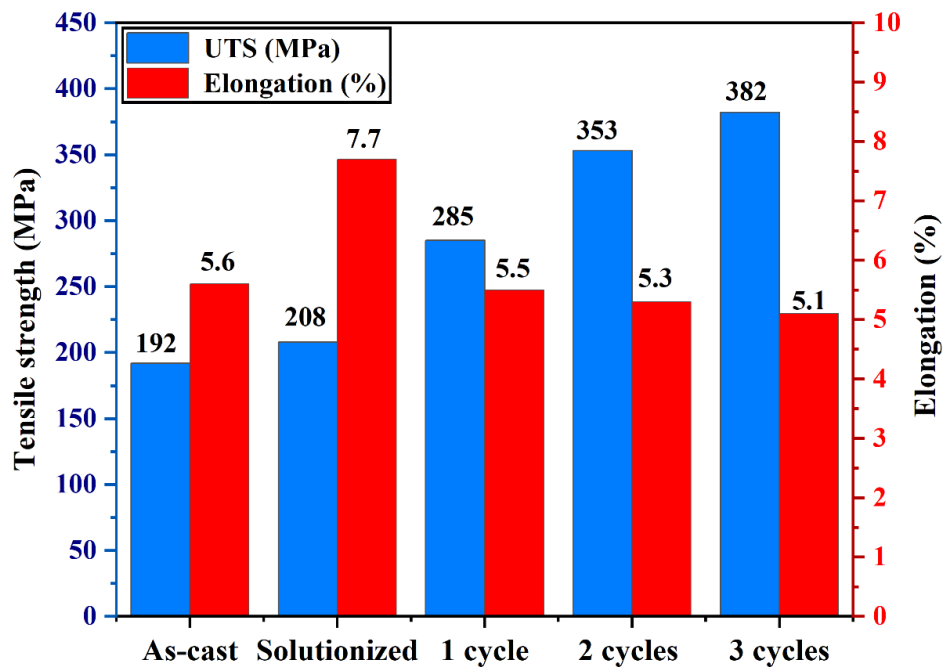
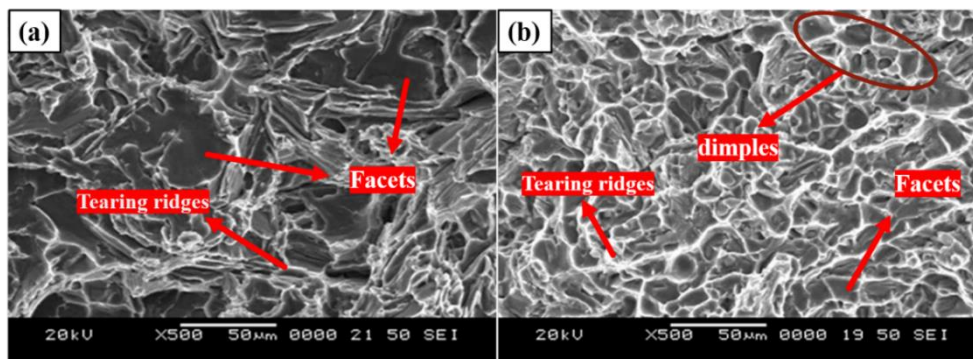


Figure 4.22: Strength-elongation bar chart of Al-12.1Si alloy in different processing conditions.

strengths of one and two cycles processed samples are 285 MPa and 353 MPa, respectively, while percentage elongation is 5.5% and 5.3%. After three cycles, tensile strength reaches 382 MPa with 5% percentage elongation. Tensile strength (UTS) of three-cycle samples is approximately 98.9% higher than that of cast samples. In contrast to Al-12.1Si alloy with three cycles of forging, the ultimate tensile strength of Al-7.3Si alloy with two cycles of forging increased dramatically.

### 4.3.3 Tensile-tested fracture surface

Figure 4.23 displays tensile tested fracture surfaces of as-cast and solutionized Al-7.3Si alloys. Similarly, Figure 4.24 shows tensile tested fracture surfaces of as-cast and solutionized Al-12.1Si alloys. As seen in Figures 4.23a and 4.24a, the tensile tested fracture surface of as-cast alloy displays large cleavage facets due to fracture of brittle silicon particles (Rao et al. 2018). These kinds of fractures are related to low-energy mode of fracture (Azmah Hanim et al. 2011). Also fractured surface of the as-cast sample displays flat regions, representing easy crack nucleation and propagation. Figure 4.23b displays fractured surface of the solutionized Al-7.3Si alloy, which consists of dimples and a few facets surrounded by tearing ridges. However, in Figure 4.24b, fractured surface of the solutionized Al-12.1Si alloy exhibits decreased facets with tearing ridges. Figures 4.25a and b depict the fracture surfaces of tensile-tested MDF-processed Al-7.3Si alloys. Similarly, Figures 4.26a, b, and 4.27 depict the fracture surfaces of MDF-processed Al-12.1Si alloys. Fracture surface is characterised by facets and tearing ridges after MDF processing. It can also be observed that, with



**Figure 4.23: SEM micrographs of the fracture surface of Al-7.3Si alloy: (a) as-cast, (b) solutionized.**

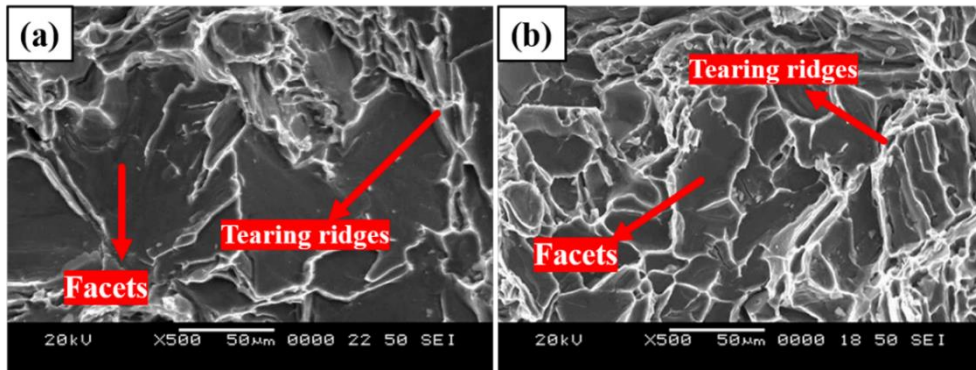


Figure 4.24: SEM micrographs of the fracture surface of Al-12.1Si alloy: (a) as-cast, (b) solutionized.

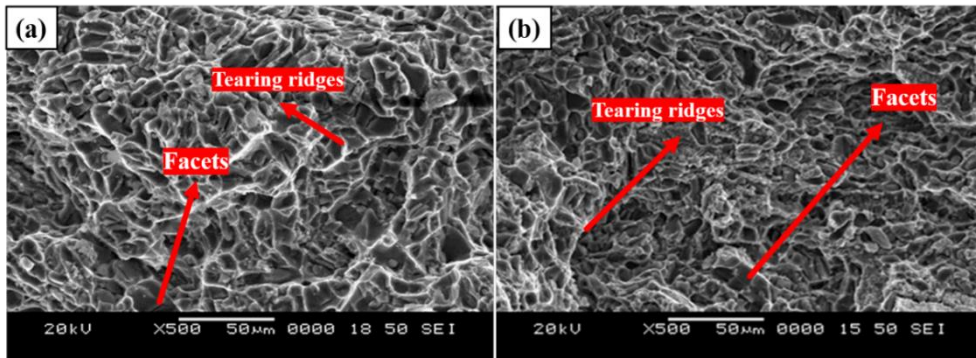


Figure 4.25: SEM micrographs of the fracture surface of Al-7.3Si alloys: (a) one cycle; (b) two cycles.

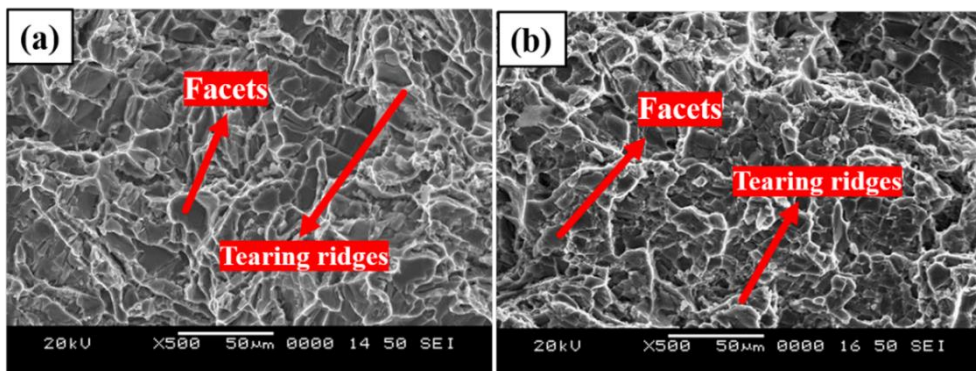
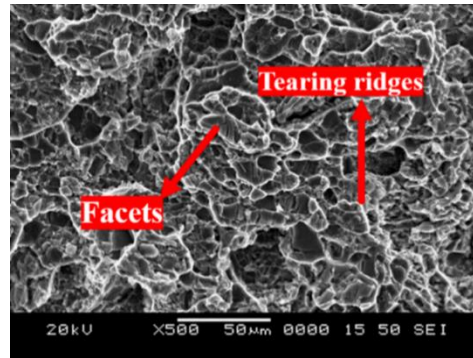


Figure 4.26: SEM micrographs of the fracture surface of Al-12.1Si alloys: (a) one cycle; (b) two cycles.



**Figure 4.27: SEM micrographs of the fracture surface of Al-12.1Si alloy with three-cycle.**

increasing number of MDF cycles, size of facets decreased considerably, and more tearing ridges formed. However, fracture surfaces of MDF-processed Al-7.3Si samples show few dimples with decreased facet size. With the existence of both facets and tearing ridges, the fracture mode can be classified as a mixed one. Tear ridges are caused by considerable plastic deformation of aluminium phase, and circled traces are fracture evidence of Si particles in a brittle manner.

Based on previous reports, impact of various SPDs on mechanical characteristics of hypoeutectic and eutectic Al-Si alloys is shown in Tables 4.5 and 4.6. From Table 4.5, UTS achieved by MDF-processed Al-7.3Si alloys is higher than that of processed by different SPD methods, as reported in the literature. However, there is improvement in percentage elongation (13%) when processed by ECAP. HPT-processed material showed higher microhardness than the other SPD techniques, but it has the drawback of having a small sample size (Pippan et al. 2008). From Table 4.6, ECAP on the SLM-as-built Al-12Si alloy showed highest tensile strength and hardness. Higher mechanical properties (UTS and hardness) were obtained as a result of combined effects of selective laser melting (SLM) and ECAP. However, selective laser melting is very expensive and requires high-powered lasers. Al-11Si alloy with rotary-die ECAP processing at 573 K produced a tensile strength of 250 MPa. Similarly, friction stir processing and ECAP at 200 °C on Al-12Si alloy resulted in tensile strengths of 180 MPa and 159 MPa, respectively. In the current study, Al-12.1Si alloy with three cycles of MDF achieved tensile strength of 382 MPa and hardness of 100.2 Hv, which is higher than that of earlier research, except for the combination of SLM and ECAP. Furthermore, the

amount of enhanced tensile strength and hardness from MDF is higher even after two cycles compared to RD-ECAP (32 passes), FSP, and ECAP (6 passes). The RD-ECAP and FSP technique yields a higher degree of ductility than previously reported values.

**Table 4.5 Influence of various SPD on mechanical characteristics of Al–7.3Si alloys**

<b>Studies &amp; Conditions</b>	<b><math>\sigma_{UTS}</math> (MPa)</b>	<b><math>\epsilon_f</math> (%)</b>	<b>Hv</b>	<b>Reference</b>
As-cast ECAP at RT	$\approx 140$ $\approx 270$	4.5% 13%	--- ---	Gutierrez-Urrutia I et al. 2008
As-cast ARB at RT	103 269	2.1 5.3	55.4 100	(Jamaati et al. 2011)
As-cast Rheoforged and MDF (3 passes)	--- ---	--- ---	61.6 84	(Dodangeh et al. 2012)
As-cast (annealing) As-cast (cooling slope) ECAP at RT (annealing) ECAP at RT (cooling slope)	--- --- --- ---	--- --- --- ---	$\approx 36$ $\approx 39$ $\approx 78$ $\approx 85$	Thuong et al. (2015)
As-cast HPT at RT (10 turns)	--- ---	--- ---	71.5 185	Wang et al. (2015)
As-cast Cryorolling	129 332	3.8 5	60 108	Immanuel R. J., & Panigrahi S. K. (2015).
As-cast MDF (RT-2cycles)	177 441	7.5 5.6	75 125	Current

**Table 4.6 Influence of various SPD on mechanical characteristics of Al–12Si alloys**

<b>Studies &amp; Conditions</b>	<b><math>\sigma_{UTS}</math> (MPa)</b>	<b><math>\epsilon_f</math> (%)</b>	<b>Hv</b>	<b>Reference</b>
As-cast Modifier and RD- ECAP (573 K-32 passes)	$\approx 210$ $\approx 250$	$\approx 7$ $\approx 14$	--- ---	Ma, A. et al., (2005)
As-cast ECAP (200 $\pm$ 5 °C- 6 passes)	122 180	2.2 10.1	--- ---	Kucukomeroglu T et al., (2010)
FSP RPM = 500–1400 traverse speeds = 28 mm/min	159	9.87	57	Sun et al. (2018)
SLM & as-cast SLM & ECAP (150 °C- 4 passes)	465 514	3.8 5.9	140 162	Hosseinzadeh et al., (2021)
As-cast MDF (R T- 3 cycles)	192 382	5.6 5.1	66.6 100	Current

However, multidirectional forging appears to be a more suitable technique for industries than other types of SPD techniques since it can process relatively large samples. Additionally, due to its simplicity, MDF can be employed on a small to medium scale.

#### 4.3.4 Flow properties

Material properties such as strength coefficient (K) and strain hardening exponent (n) are calculated using compression test. This is an approximation of plastic flow, or strain hardening behaviour, of material when stress exceeds the yield strength. The strain-hardening behaviour of unprocessed and processed Al-7.3Si and Al-12.1Si alloys is examined using true stress-true strain diagram obtained from the compression test. For this purpose, true stress-true strain relationship is summed up by Hollomon equation. According to this, double logarithmic plots of true stress against true strain result in a straight line ( $\log \sigma = \log K + n \log \epsilon$ ), whose slope is equal to strain hardening exponent (n), and whose intercept with true strain value of 1 is the strength coefficient (K). Figure 4.28 depicts the true stress and true strain graphs of Al-7.3Si alloys under different processing conditions. Figure 4.29 shows the strength coefficient and strain hardening exponent for as-cast, solutionized, and MDF Al-7.3Si alloys. Strain hardening exponent and strength coefficient of as-cast specimens are 0.19 and 337 MPa, respectively. Furthermore, after heat treatment, strain hardening exponent and strength coefficient of the specimen increased to 2.2 and 412 MPa, respectively. Strain hardening exponent of MDF-processed up to one cycle sample decreased to 0.08 and strength coefficient increased to 424 MPa, respectively. After two cycles of MDF processing, strain hardening exponent further decreased to 0.05 and strength coefficient value increased to 442 MPa, respectively. Similarly, Figure 4.30 depicts the true stress and true strain graphs of Al-12.1Si alloys under different processing conditions. Figure 4.31 shows the strength coefficient and strain hardening exponent for as-cast, solutionized, and MDF Al-12.1Si alloys. As shown in Figure 4.31, the strain hardening exponent and strength coefficient of as-cast samples are 0.14 and 257 MPa, respectively. After solutionizing, the strain hardening exponent and strength coefficient increased to 0.16 and 260 MPa, respectively. Strain hardening exponents for one-cycle and two-cycle samples are decreased to 0.081 and 0.062, while the strength coefficient increased to 305 MPa and 337 MPa, respectively. After three cycles, the strain hardening exponent decreased to 0.061 and the strength coefficient increased to 347 MPa. It is clear that strain hardening exponents in both alloys increased after solutionizing and steadily dropped as the number of MDF cycles increased. But strength coefficient is continuously increasing

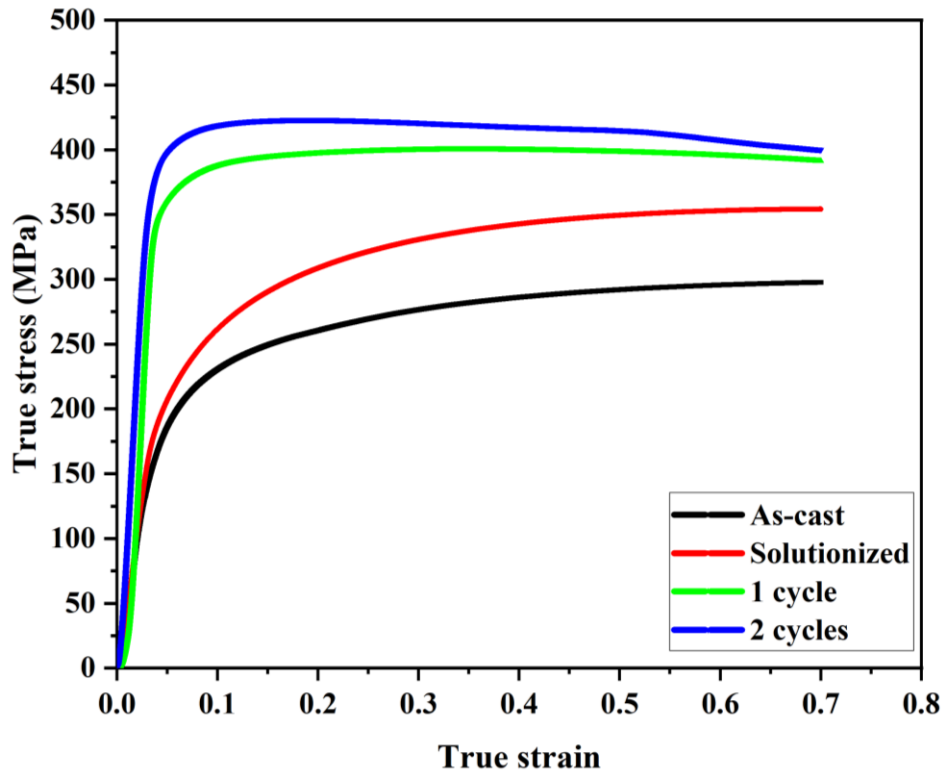


Figure 4.28: Compression true stress-strain graph of as-cast, solutionized, and MDF-processed Al-7.3Si alloy.

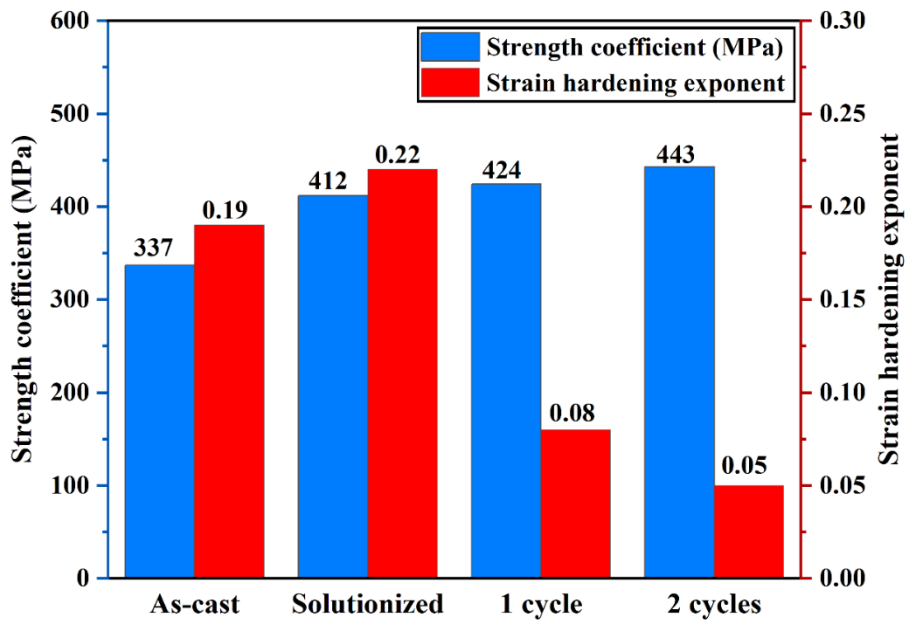


Figure 4.29: Strength coefficient and strain hardening exponent of as-cast, solutionized, and MDF-processed Al-7.3Si alloys.

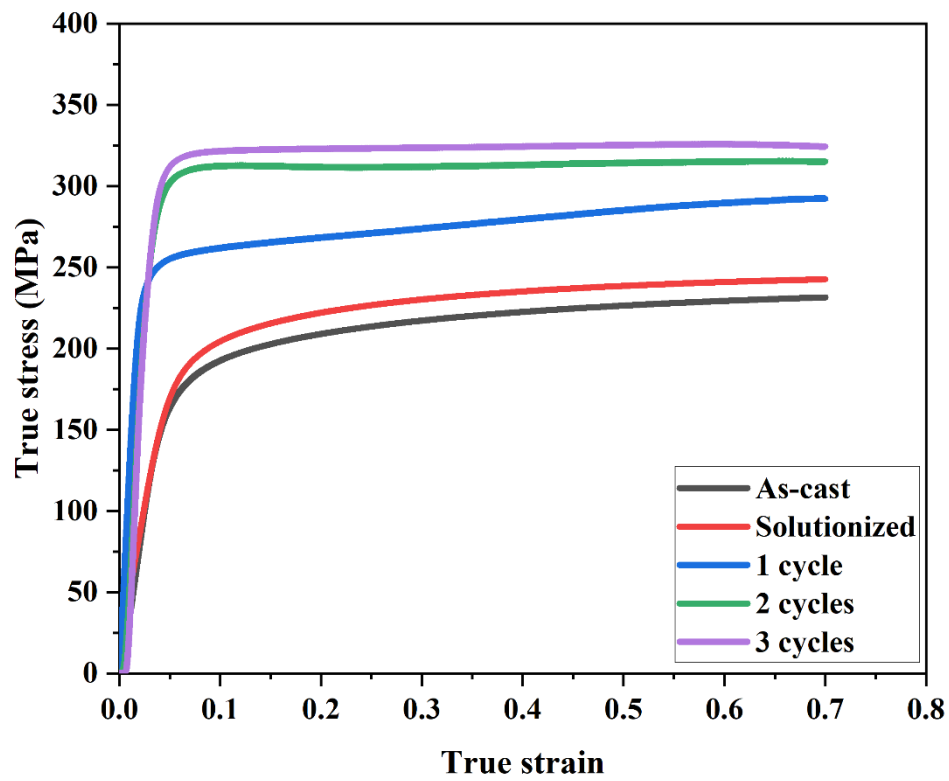


Figure 4.30: Compression true stress-strain graph of as-cast, solutionized, and MDF-processed Al-12.1Si alloy.

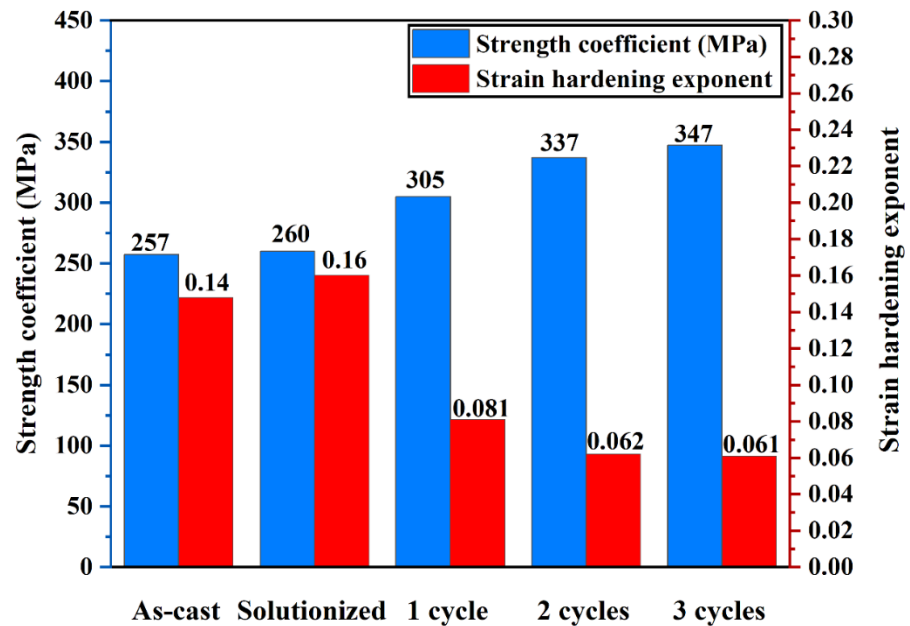
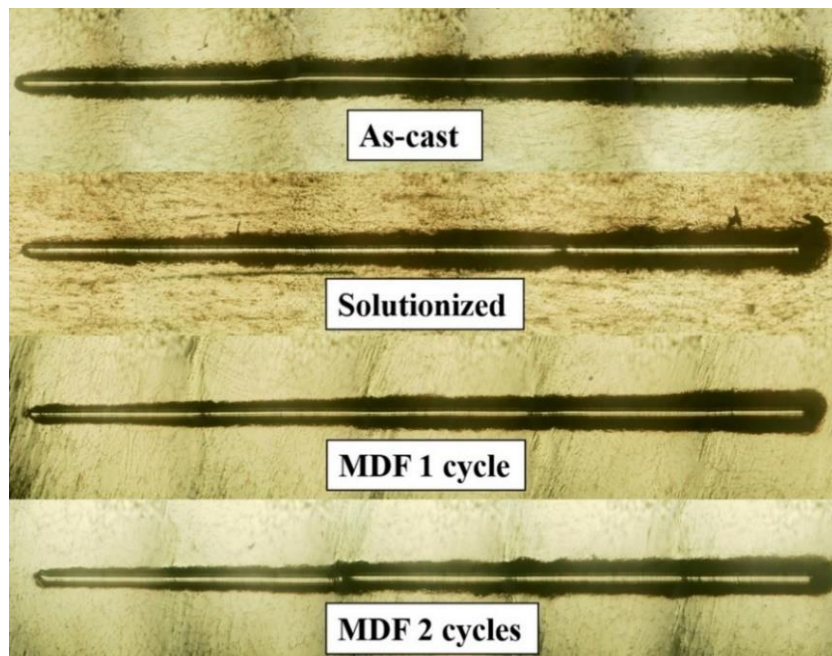


Figure 4.31: Strength coefficient and strain hardening exponent of as-cast, solutionized, and MDF-processed Al-12.1Si alloy.

as the number of MDF cycles increases. MDF-processed Al-7.3Si alloys with two cycles and Al-12.1Si with three cycles showed higher strength coefficients compared to other samples.

#### 4.3.5 Scratch Testing

In scratch test process, a diamond indenter is moved across the surface of testing material at constant speed with a defined normal load over a specified distance. The normal force can be set as constant, progressive, or incremental. Scratch testing is used to evaluate a material's resistance to scratch damage or to measure scratch hardness. In the current study, scratch test involved applying a progressive load of 2–15 N over 5 mm scratch distance at speed of 1 mm/min. Figures 4.32 and 4.33 display the scratch images and variations in scratch depth of as-cast, solutionized and MDF-processed Al-7.3Si alloys. It can be seen from Figure 4.33 that the maximum scratch depth values for as-cast and solutionized samples at maximum progressive load of 15 N are 99.5  $\mu\text{m}$ , and 50.1  $\mu\text{m}$ , respectively. The maximum scratch depth values for MDF processed up



**Figure 4.32: Scratch images of Al-7.3Si alloy in various processing conditions under progressive load scratch test (2–15 N).**

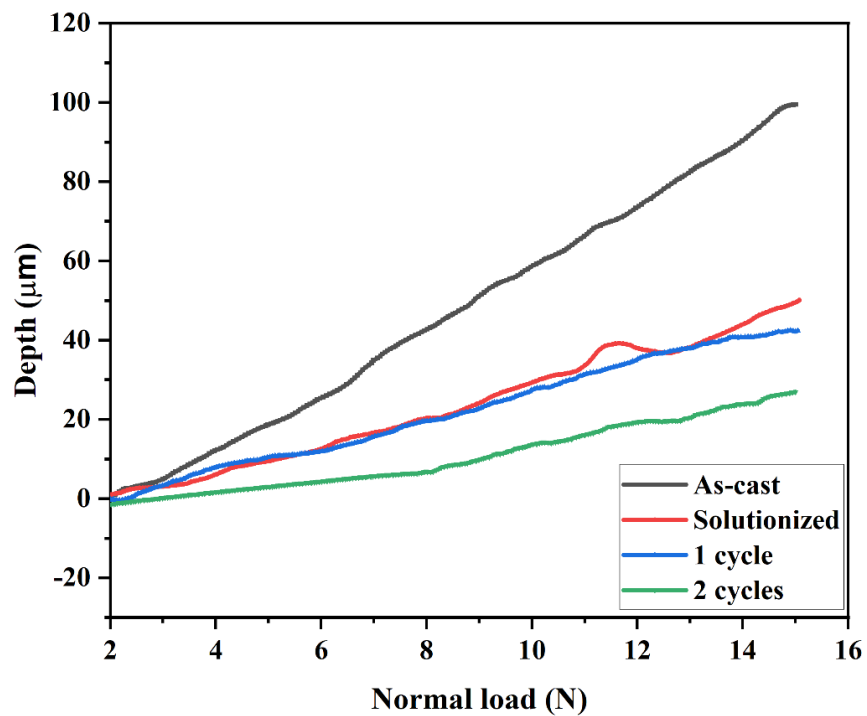


**Figure 4.33: Variation in scratch depth of Al-7.3Si alloy in various processing conditions under progressive load scratch test (2–15 N).**

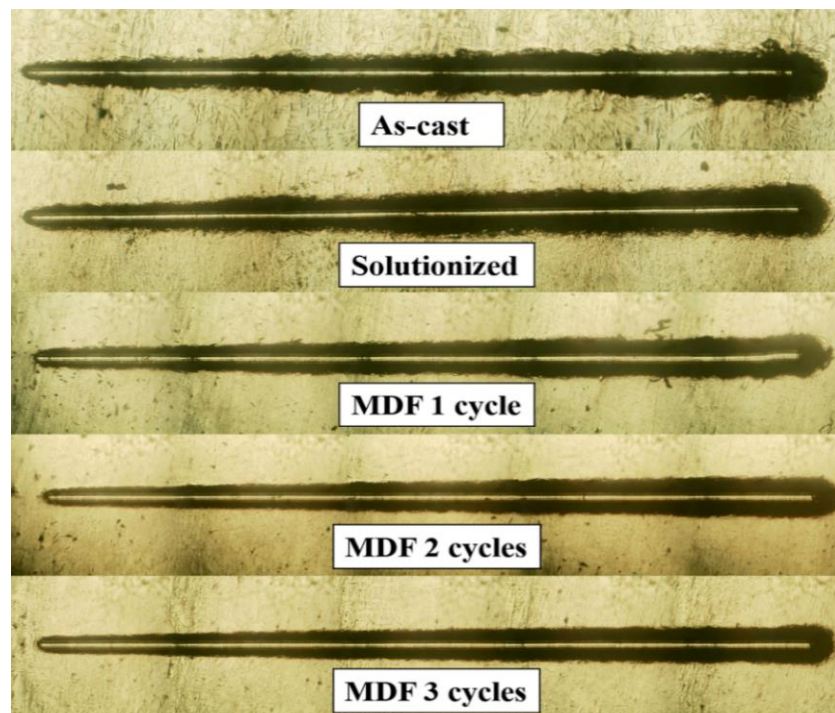


**Figure 4.34: Scratch images of Al-12.1Si alloy in various processing conditions under progressive load scratch test (2–15 N).**

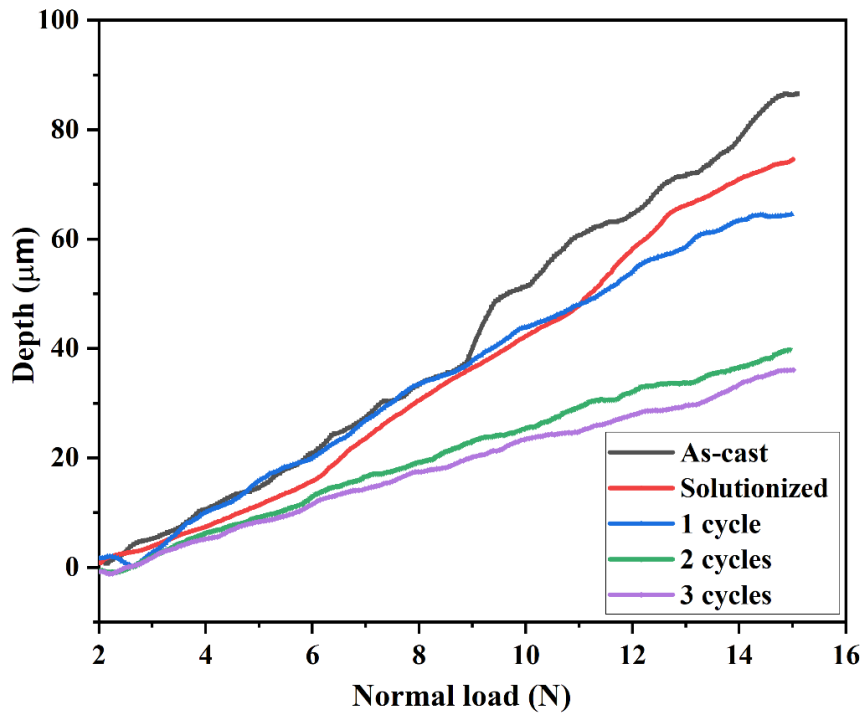
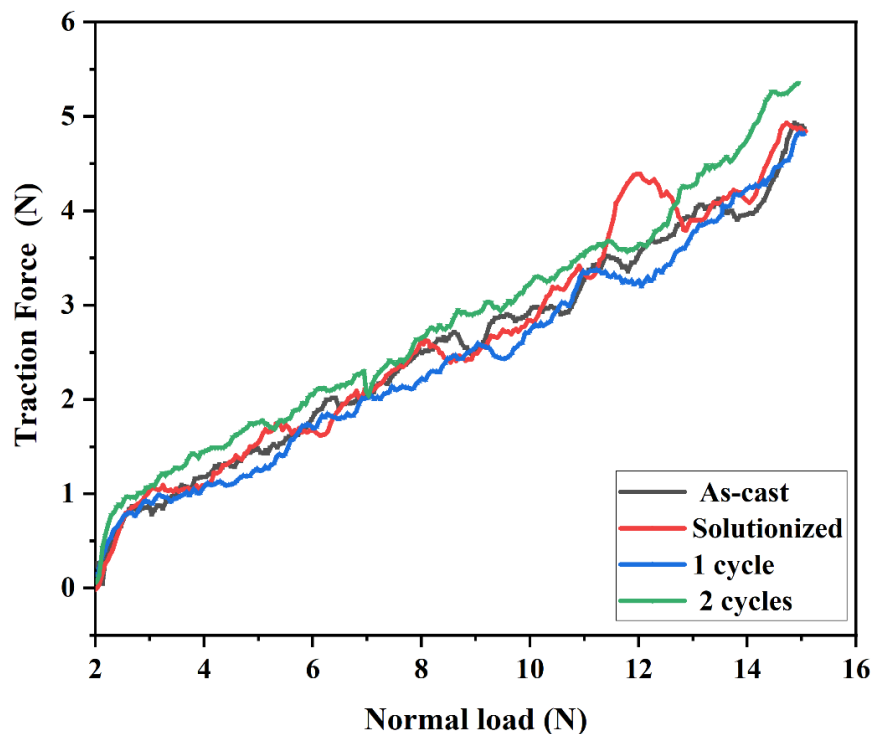


**Figure 4.35: Variation in scratch depth of Al-12.1Si alloy in various processing conditions under progressive load scratch test (2–15 N).**

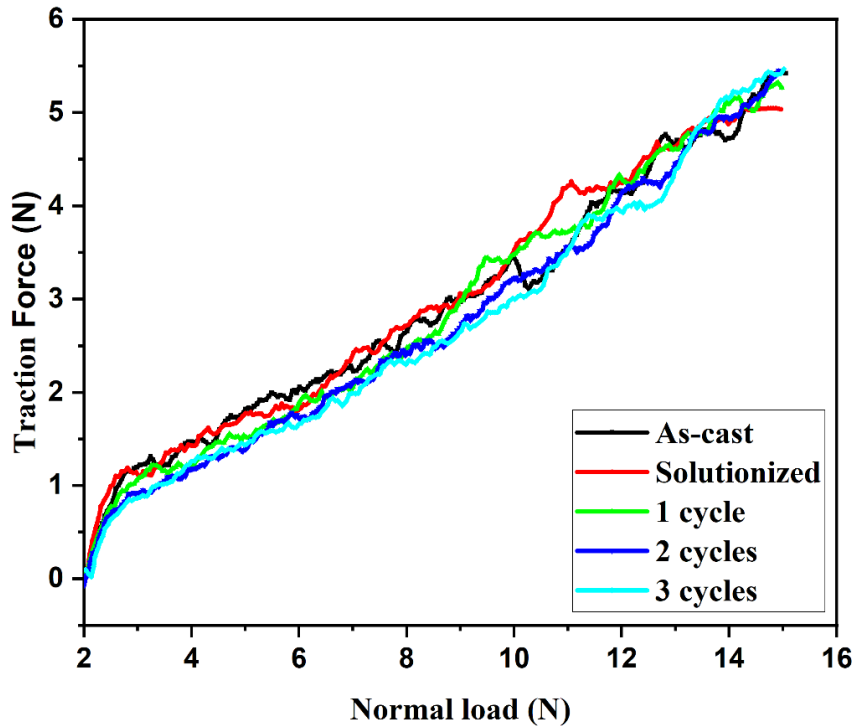
to one and two cycles samples are 42.4  $\mu\text{m}$ , and 26.9  $\mu\text{m}$  respectively, at a maximum progressive load of 15 N. Similarly, Figures 4.34 and 4.35 represents the scratch images and variations in scratch depth of as-cast, solutionized and MDF-processed Al-12.1Si alloys. As can be seen from Figure 4.35, the maximum scratch depth values for as-cast and solutionized are 86.6  $\mu\text{m}$  and 74.5  $\mu\text{m}$ , respectively, at a maximum progressive load of 15 N. MDF-processed samples up to one and two cycles show scratch depths of 64.7  $\mu\text{m}$ , and 39.8  $\mu\text{m}$  at a maximum progressive load of 15 N. After three cycles of MDF processing, the scratch depth is reduced to 36.1  $\mu\text{m}$  at a maximum progressive load of 15 N. It can be observed that the scratch resistance significantly increased after MDF processing. MDF-processed Al-7.3Si alloys with two cycles and Al-12.1Si alloys with three cycles showed higher scratch hardness. In comparison to Al-12.1Si alloys with three cycles, Al-7.3Si alloys with two cycles displayed higher scratch hardness.

Figure 4.36 depicts the variation of scratch traction force of as-cast, solutionized and MDF-processed Al-7.3Si alloys under a progressive load of 2 to 15 N. Similarly, Figure 4.37 depicts the variation of scratch traction force of as-cast, solutionized, and MDF-

processed Al-12.1Si alloys with a progressively increased load of 2 to 15 N. It is evident from Figures 4.36 and 4.37 that traction force mainly depends on the hardness of material and scratch depth at higher load. It can be revealed that MDF-processed samples exhibit higher traction force at maximum progressive load of 15 N, particularly for Al-7.3Si alloy with two cycles of forging as well as Al-12.1Si alloy with two and three cycles of forging at minimum scratch depth. However, initial traction force is lower in MDF with two and three cycles of Al-12.1Si alloys but increases with increasing load. Increasing the traction force of MDF-processed material even at a minimum scratch depth indicates a significant improvement in scratch hardness. Al-7.3Si alloys with two cycles of forging exhibit a slightly higher traction force compared to Al-12.1Si alloys with three cycles of forging. Increased scratch hardness is primarily responsible for higher tractional force in Al-7.3Si alloys with two cycles of MDF. However, there is no significant variation in the tractional forces of one-cycle-processed Al-7.3Si and Al-12.1Si alloys compared to as-cast alloys. On the other hand, as-cast materials exhibit low tractional forces in comparison to scratch depth, which



**Figure 4.36: Traction force of Al-7.3Si alloy in various processing conditions under progressive load scratch test (2–15 N).**



**Figure 4.37: Traction force of Al-12.1Si alloy in various processing conditions under progressive load scratch test (2–15 N).**

indicates low scratch hardness. Figure 4.38 shows variation in the coefficient of friction (COF) for as-cast, solutionized, and MDF-processed Al-7.3Si alloys under progressive load of 2 to 15 N. Similarly, Figure 4.39 shows variation in the COF for as-cast, solutionized, and MDF-processed Al-12.1Si alloys under a progressive load of 2 to 15 N. From Figure 4.38, it can be observed Al-7.3Si alloys with two cycles of MDF processing exhibit a marginally increased coefficient of friction compared to other samples. Increased scratch hardness of Al-7.3Si alloys with two cycles of MDF samples is the reason behind higher coefficient of friction. As the hardness increases, frictional force required to plough and cut the surface also increases, which leads to increased coefficient of friction. Al-12.1Si alloys with two and three cycles of forged samples display low initial COF that gradually increases with increasing load. However, there is no significant variation in the coefficient of friction between the processed and unprocessed samples.

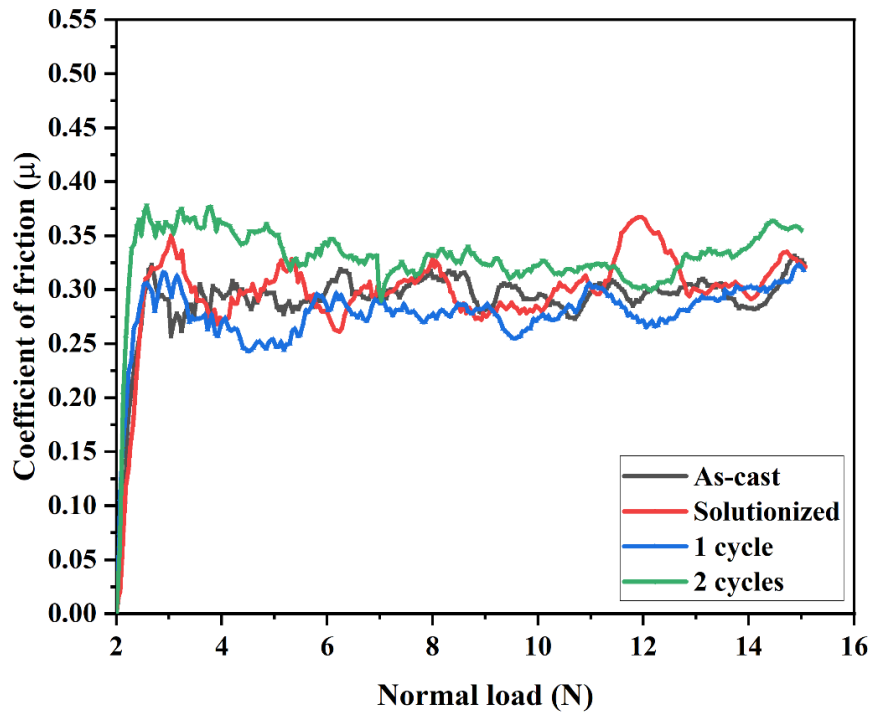


**Figure 4.38: coefficient of friction of Al-7.3Si alloy in various processing conditions under progressive load scratch test (2–15 N).**

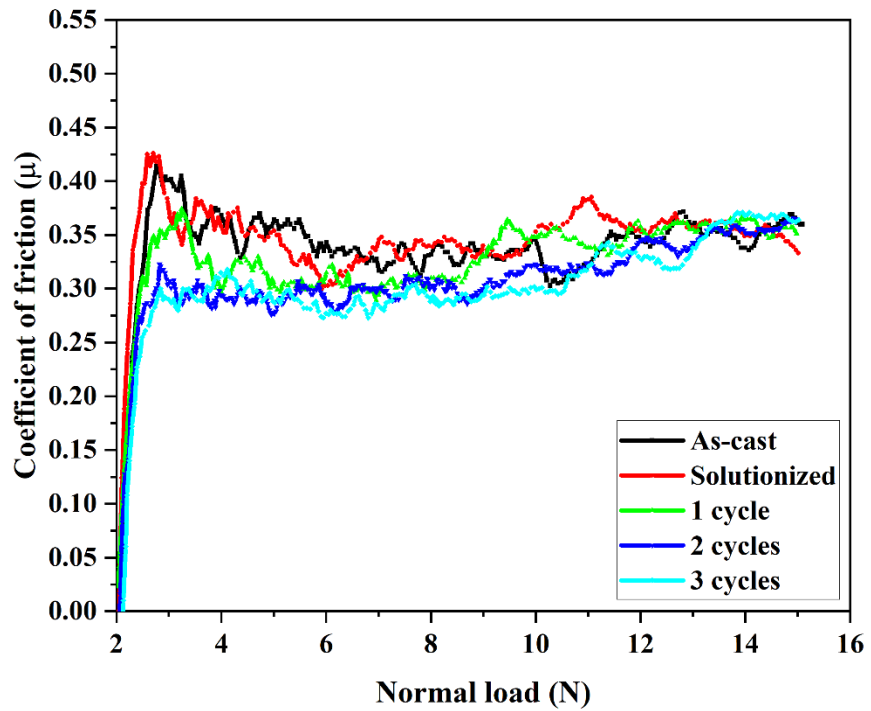


**Figure 4.39: coefficient of friction of Al-12.1Si alloy in various processing conditions under progressive load scratch test (2–15 N).**

## 4.4 Wear properties

### 4.4.1 Wear mass loss

Figures 4.40 and 4.41 display the wear mass loss of Al-7.3Si alloy and Al-12.1Si alloy with varying applied loads (19.61 N and 39.23 N) and sliding speed of 0.7 m/s at a constant sliding distance of 1500 m. It can be noted that weight loss increased with increasing applied load in both Al-7.3Si and Al-12.1Si alloys for all conditions, which is consistent with Archard's law that volume wear loss is proportional to the applied load. As the applied load increases, contact between pin and disc increases, causing more friction and wear. However, the weight loss of MDF-processed samples in both alloys was greatly reduced when compared to as-cast samples. Al-7.3Si alloy with two cycles of MDF processing and Al-12.1Si alloy with three cycles of MDF processing have shown maximum wear resistance for all wear conditions. Reduced wear mass loss of Al-7.3Si alloys after two cycles of MDF under varying applied loads (19.61 N and 39.23 N) and sliding speed of 0.7 m/s is 72.4% and 65.3%, respectively. Similarly, the reduced wear mass loss of Al-12.1Si alloys after three cycles of MDF under varying applied loads (19.61 N and 39.23 N) and sliding speed of 0.7 m/s is 62% and 54%, respectively. Improvement in wear resistance of MDF-processed samples can be attributed to their increased hardness. Improved hardness of MDF-processed Al-Si alloys is due to refinement of eutectic silicon as well as strain hardening of aluminium phase. The anti-friction and wear characteristics of silicon particles are strongly related to their form, size, uniform distribution, and cohesion with the matrix, all of which play significant roles in effectively sustaining the load (Gode et al. 2014). Small Si particles are also less likely to fracture, making them reliable load-bearing components. They consequently lower shear stresses that are transmitted to bulk surface material. These are factors responsible for increased wear resistance of MDF-processed samples. It is shown that cast alloys have greater wear mass loss compared to MDF-processed samples. Presence of porosity and non-uniformly distributed coarse acicular eutectic silicon in as-cast microstructure, as well as the low hardness of Al phase, is the reason behind highest wear mass loss. The needle-like silicon microstructure in cast Al-Si alloys is "network" of more or less interconnected plates. Since some eutectic Si phases break and can spread quickly through the structure, the load-bearing area quickly

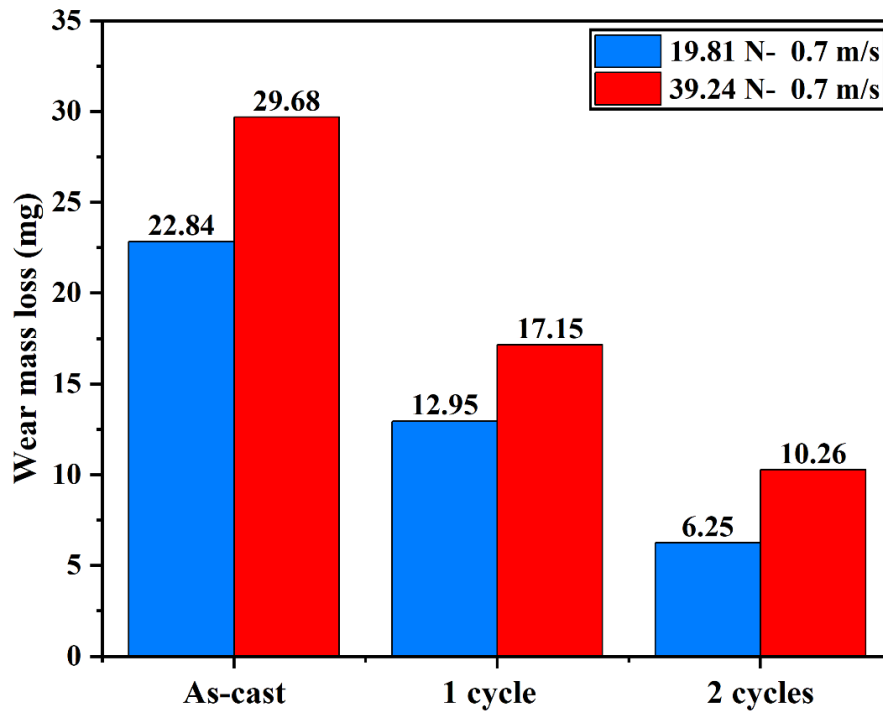


Figure 4.40: Wear mass loss of Al-7.3Si alloy under varying applied loads (19.61 N and 39.23 N) and a sliding velocity of 0.7 m/s.

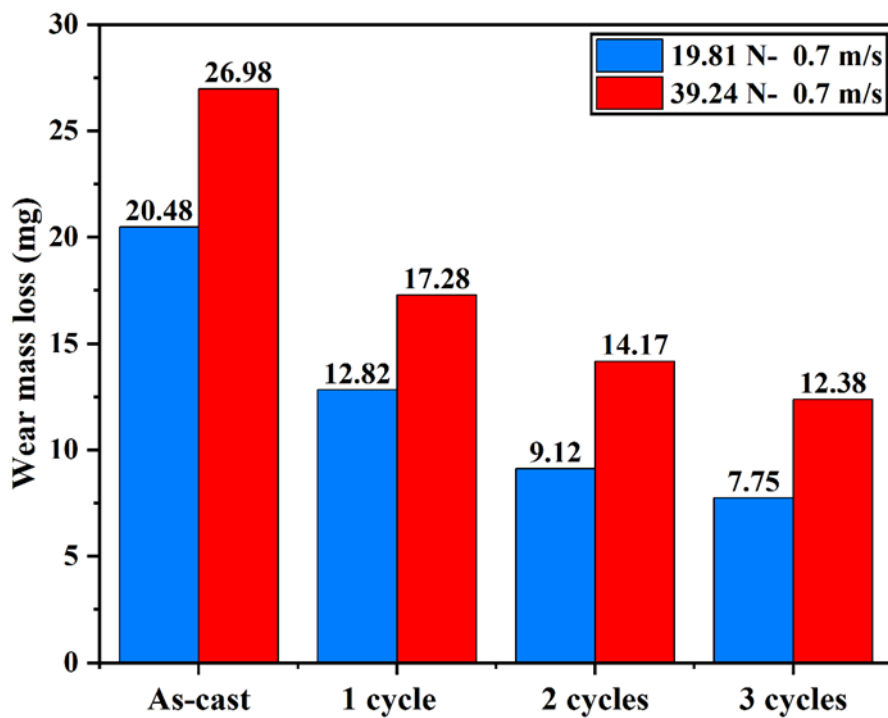


Figure 4.41: Wear mass loss of Al-12.1Si alloy under varying applied loads (19.61 N and 39.23 N) and a sliding velocity of 0.7 m/s.

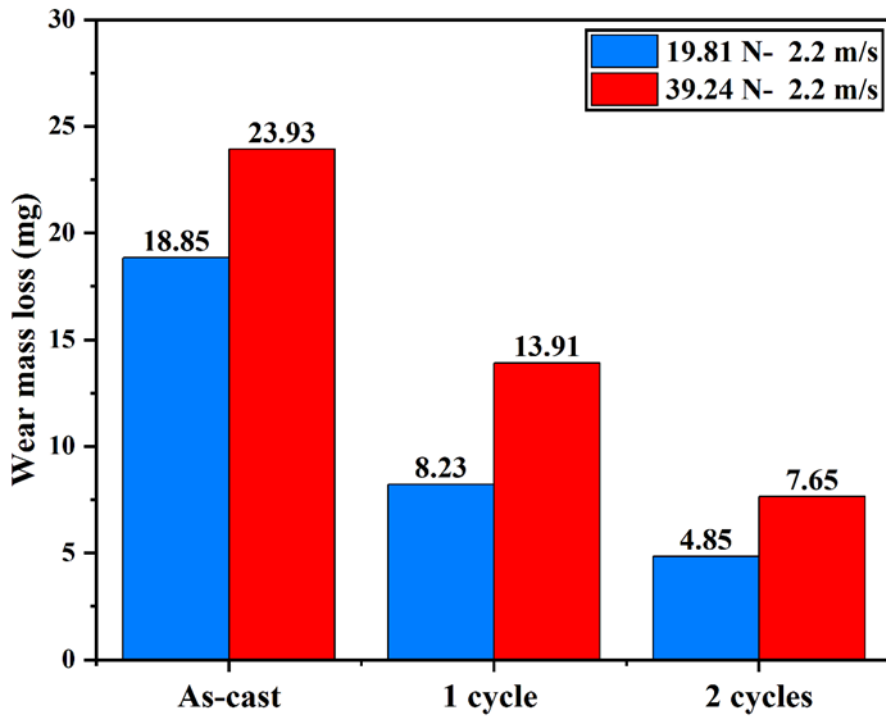


Figure 4.42: Wear mass loss of Al-7.3Si alloy under varying applied loads (19.61 N and 39.23 N) and a sliding velocity of 2.2 m/s.

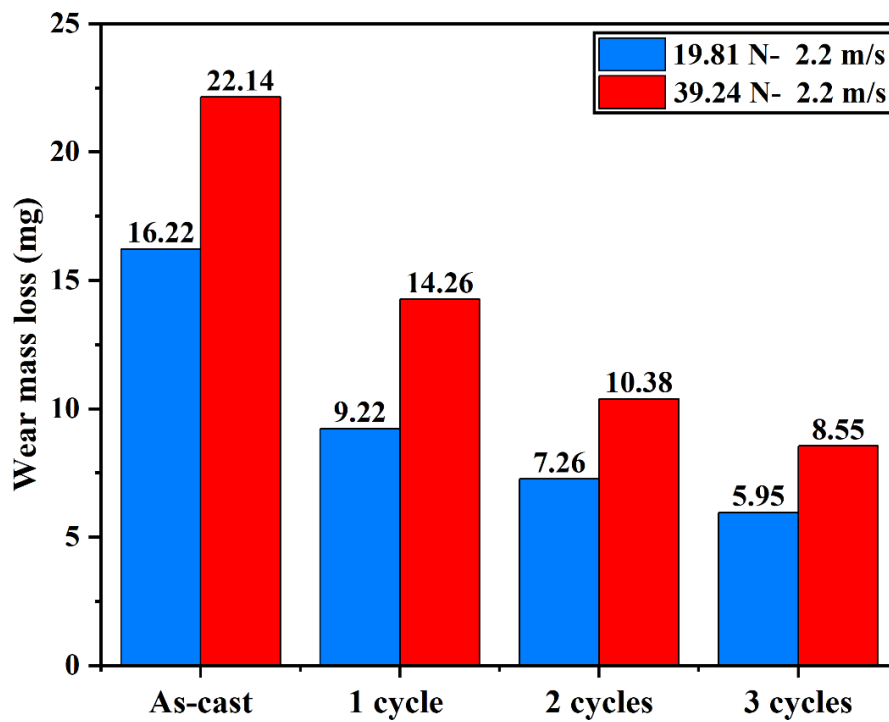


Figure 4.43: Wear mass loss of Al-12.1Si alloy under varying applied loads (19.61 N and 39.23 N) and a sliding velocity of 2.2 m/s.

decreases in the needle-like eutectic Si structure (C. L. Xu et al., 2007). Figures 4.42 and 4.43 show the wear mass loss of Al-7.3Si alloy and Al-12.1Si alloy with varying applied loads (19.61 N and 39.23 N) and sliding speed (2.2 m/s) at constant sliding distance of 1500 m. Results demonstrated that for all normal loads, the mass loss for MDF-processed samples is much lower than for as-cast samples. However, with increase in sliding speed from 0.7 m/s to 2.2 m/s, there is decrease in wear mass loss in all samples under two levels of load, 19.61 N and 39.23 N. Increased formation of oxide could be the result of dressed-wear mass loss at higher sliding speeds. According to wear mass loss analysis, mass loss is decreased at lower applied load and higher sliding speed. Similarly, with higher applied loads and lower sliding speeds, mass loss is increased.

Figures 4.44 and 4.45 depict the friction coefficients of Al-7.3Si alloy and Al-12.1Si alloy with varying applied loads (19.61 N and 39.23 N) and sliding speed of 0.7 m/s at constant sliding distance of 1500 m. The frictional force  $F$  is obtained dynamically during the test from the load cells of test rigs. Furthermore, coefficient of friction is calculated using the expression  $F/N$ , where  $N$  is the normal load applied and  $F$  is the resistive force of friction. It can be noted that the friction coefficient increases with increase in applied load in both Al-7.3Si and Al-12.1Si alloys. However, MDF-processed samples show low coefficient of friction compared to as-cast samples. According to Syukron et al. (2019), increase in hardness causes a decrease in adhesion and delamination, which in turn reduces the formation of asperity junctions and lowers the friction coefficient. According to Dwivedi (2010), other factors influencing a friction coefficient include its hardness, density, shear strength, and ultimate tensile strength. Furthermore, higher hardness might result in less surface contact, which would lower the friction coefficient. Figures 4.46 and 4.47 show the friction coefficients of Al-7.3Si alloy and Al-12.1Si alloy with varying applied loads (19.61 N and 39.23 N) and sliding speed (2.2 m/s) at constant sliding distance of 1500 m. It can be noted from Figures 4.46 and 4.47 that, with increase in sliding speed from 0.7 m/s to 2.2 m/s, the friction coefficient decreases in both Al-7.3Si alloy and Al-12.1Si alloys for all wear conditions. Increased oxide formation at higher speed (Figures 4.57 and 4.59) prevents the surface of sample from direct contact with counter surface (wear disc), resulting in

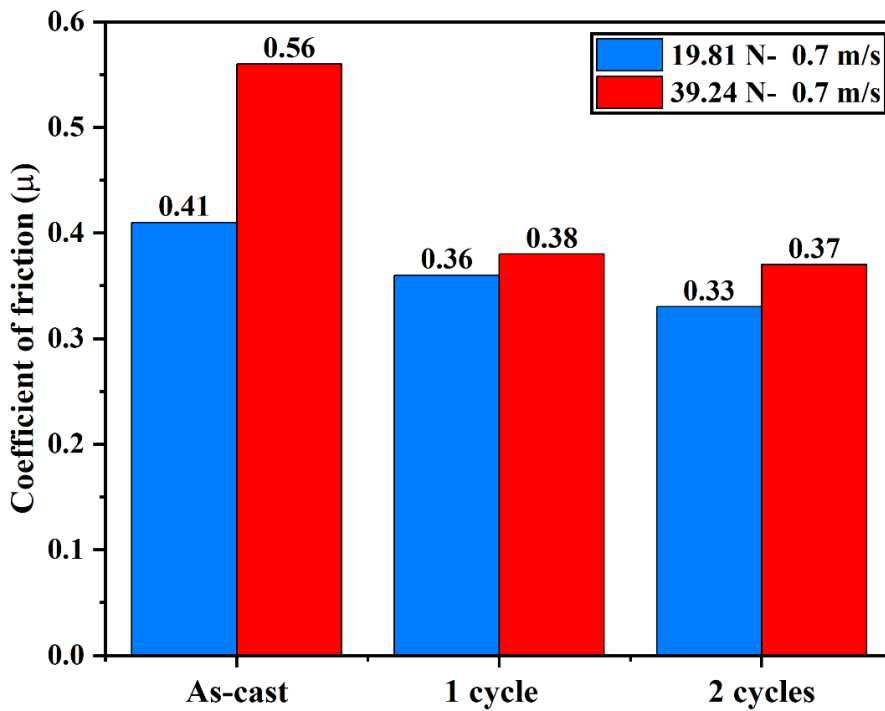


Figure 4.44: Coefficient of friction of Al-7.3Si alloy under varying applied loads (19.61 N and 39.23 N) and a sliding velocity of 0.7 m/s.

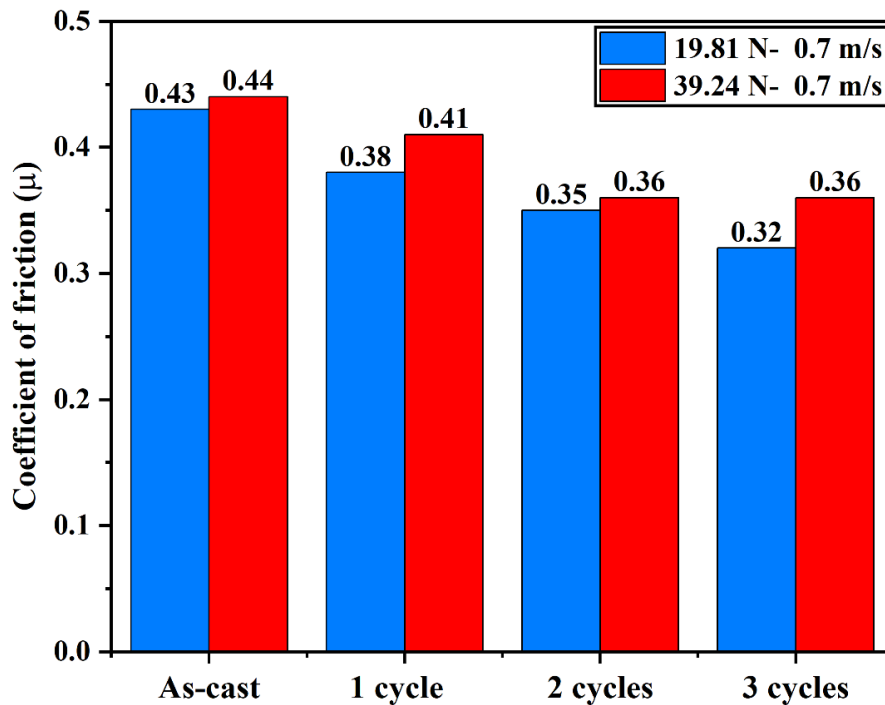


Figure 4.45: Coefficient of friction of Al-12.1Si alloy under varying applied loads (19.61 N and 39.23 N) and a sliding velocity of 0.7 m/s.

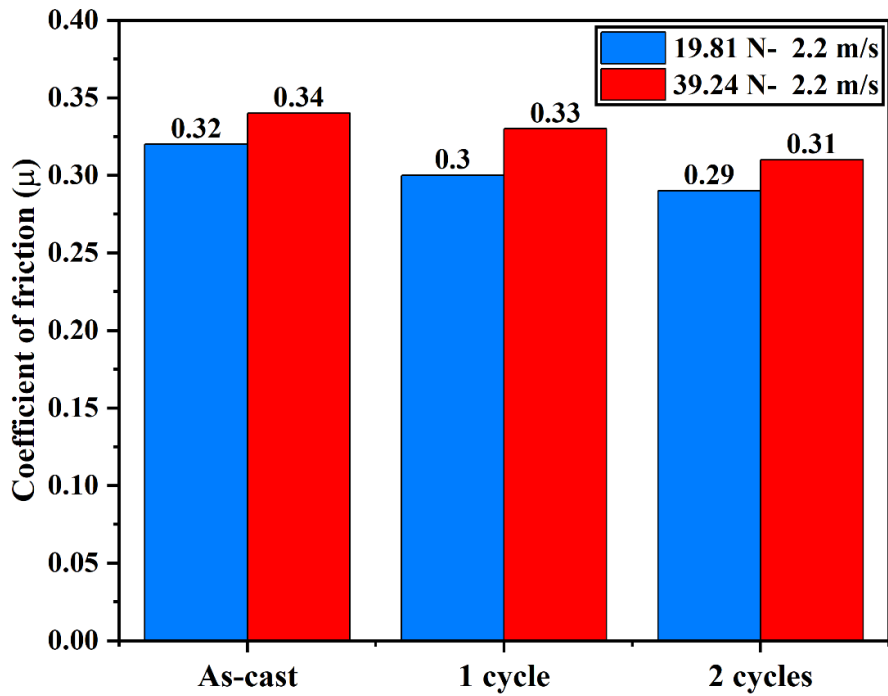


Figure 4.46: Coefficient of friction of Al-7.3Si alloy under varying applied loads (19.61 N and 39.23 N) and a sliding velocity of 2.2 m/s.

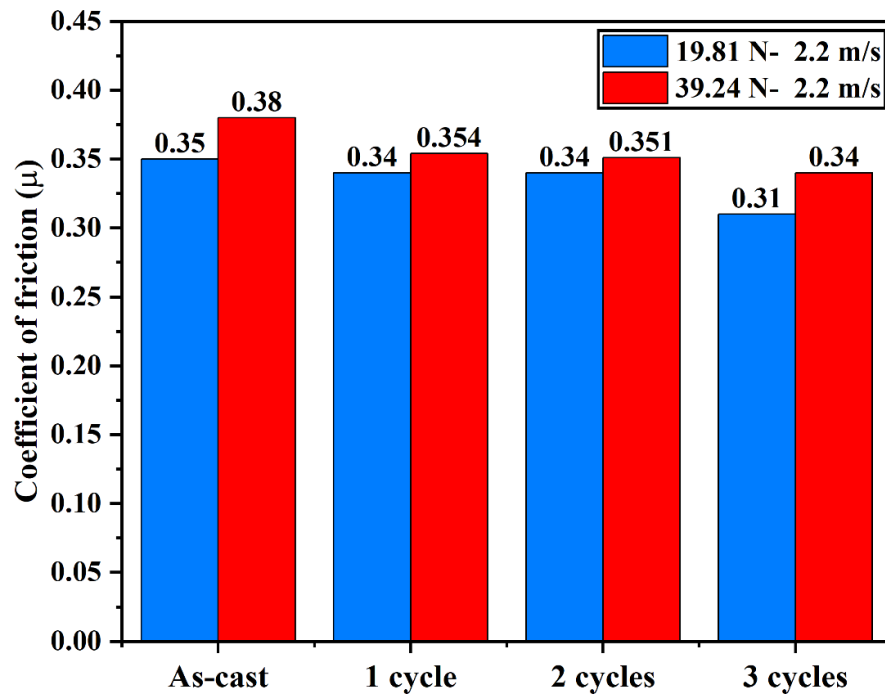
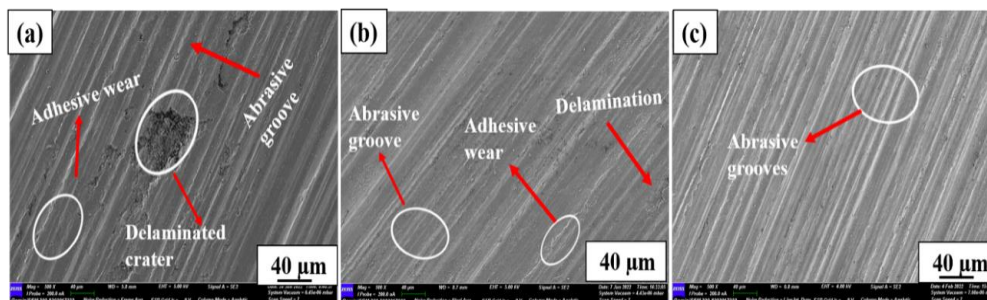


Figure 4.47: Coefficient of friction of Al-12.1Si alloy under varying applied loads (19.61 N and 39.23 N) and a sliding velocity of 2.2 m/s.

decreased coefficient of friction (Dwivedi 2010). Furthermore, as speed increases, growth of micro-welds decreases, lowering the coefficient of friction (Kori & Chandrashekharaiah 2007). It has been shown that the friction coefficients are higher with higher applied load and slower speed. However, the coefficient of friction did not change significantly despite improvements in the wear resistance of MDF-processed Al-7.3Si and Al-12.1Si alloys, particularly at higher speeds.

#### 4.4.2 Wear mechanisms

Figure 4.48 displays the FE-SEM micrographs of worn surface of as-cast and MDF-processed Al-7.3Si alloys under a load of 19.61 N at sliding speed of 0.7 m/s and constant sliding distance of 1500 m. Typically, the worn surface under different loads is observed to be combination of adhesive and abrasive regions. Figure 4.48a shows the worn surface of as-cast sample under applied load of 19.61 N at sliding speed of 0.7 m/s and consists of combination of adhesion, delamination, and abrasive regions. In adhesive wear, material transfer from one surface to another takes place during relative motion due to solid-phase welding. Wear debris that is taken from one surface is either permanently or temporarily attached to another surface. Craters on the worn surface are due to detachment of wear debris during delamination (Thuong et al. 2015). Presence



**Figure 4.48: FE-SEM image of worn surfaces of Al-7.3Si alloy under a load of 19.61 N and at a speed of 0.7 m/s: (a) cast, (b) one cycle, and (c) two cycles.**

of adhesive wear, delamination wear, and abrasive wear regions in as-cast material demonstrates highly scattered hardness distribution inside the as-cast structure. Figure 4.48b depicts the worn surface morphology of one-cycle MDF-processed sample. Wear mechanism is observed to be combination of abrasive and adhesion wear mechanisms. Moreover, it can be observed that the degree of delamination significantly decreased after MDF processing. After two cycles of MDF processing, worn surface displays

abrasive wear, as shown in Figure 4.48c. Increased hardness in MDF-processed samples is attributed to a shift in wear mechanisms from adhesive and delamination wear regions to abrasive wear regions (Gao and Cheng 2007).

Figure 4.49 depicts the surface morphology of worn samples of as-cast and MDF-processed Al-7.3Si alloys under applied load of 39.24 N at sliding speed of 0.7 m/s. As the load increases from 19.61 N to 39.23 N, the degree of wear becomes more severe in the case of as-cast alloy, as depicted in Figure 4.49a. As load increases, more material

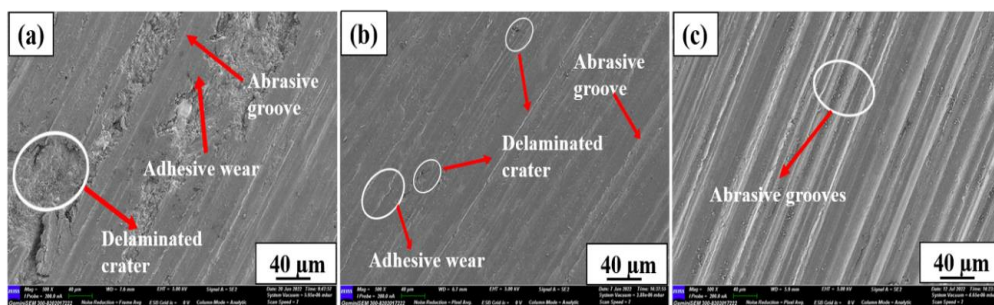
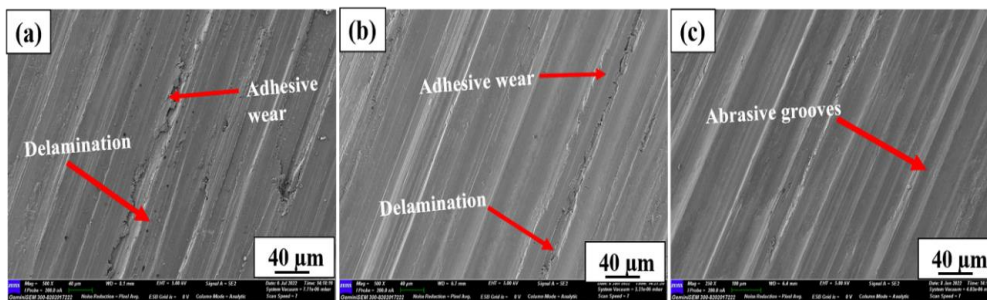


**Figure 4.49: FE-SEM image of worn surfaces of Al-7.3Si alloy under a load of 39.23 N and at a speed of 0.7 m/s: (a) as-cast, (b) one cycle, and (c) two cycles.**

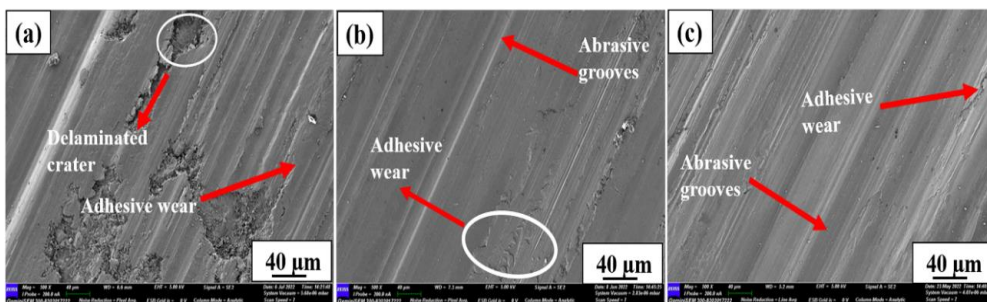
will be welded to the disc. Welding increases the tendency towards delamination. With increased material removal rate from the surface, additional voids are formed by leakage of hard phase particles, which can be observed in the cast material. As a result, craters increased with increasing load, along with adhesive and mild abrasive regions in the as-cast sample. Wear mechanism of one-cycle forged samples can be characterised as combination of adhesion regions with a slightly decreased abrasive region, as shown in Figure 4.49b. After two cycles, the depth of abrasive grooves is found to be little deeper with increased load, as shown in Figure 4.49c. However, it is noted that two cycles of MDF samples still exhibit abrasive wear.

Figure 4.50 shows the worn surface of as-cast and MDF-processed Al-7.3Si alloys under a load of 19.61 N at sliding speed of 2.2 m/s and constant sliding distance of 1500 m. Wear mechanism of as-cast sample is combination of adhesion and delamination regions, which are shown in Figure 4.50a. Wear mechanism of one cycle of MDF samples (Figure 4.50b) is found to be combination of abrasive and adhesion wear. After two cycles of MDF, the worn surface is observed to be free from any voids, and

comparatively more abrasion grooves are observed, as depicted in Figure 4.50c. It can be noted the worn surface is smoother and has fewer abrasive grooves compared to the lower sliding speed wear condition. Worn surface of MDF-processed samples is observed to be free from voids or cracks. Figure 4.51 shows the worn surface morphology of as-cast and MDF-processed Al-7.3Si alloys under load of 39.23 N at sliding speed of 2.2 m/s and constant sliding distance of 1500 m. As the load increased,



**Figure 4.50: FE-SEM image of worn surfaces of Al-7.3Si alloy under a load of 19.61 N and at a speed of 2.2 m/s: (a) cast, (b) one cycle, and (c) two cycles.**

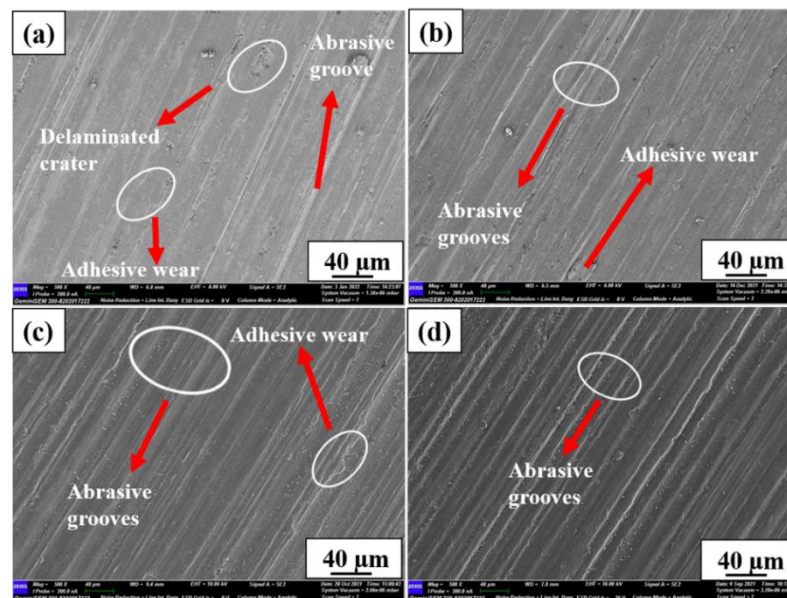


**Figure 4.51: FE-SEM image of worn surfaces of Al-7.3Si alloy under a load of 39.23 N and at a speed of 2.2 m/s: (a) cast, (b) one cycle, and (c) two cycles.**

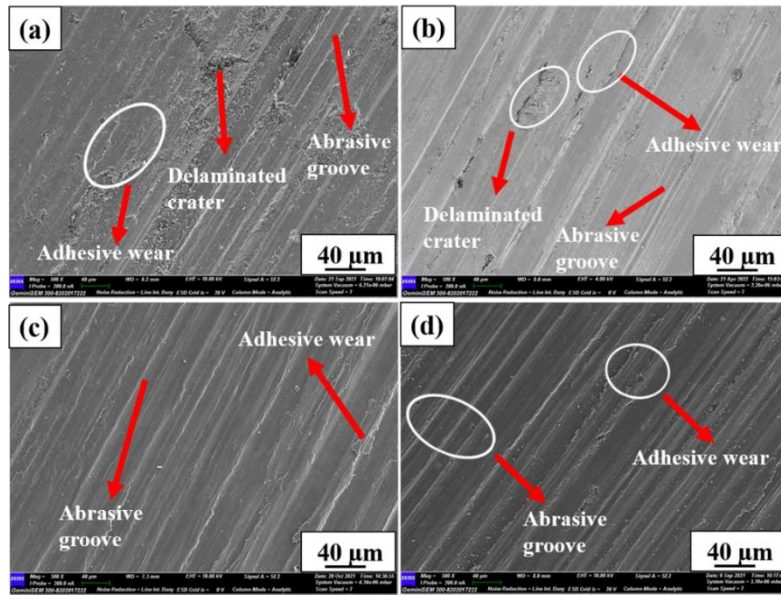
it was observed that a large extent of adhesive and delamination regions existed in as-cast alloy, which is displayed in Figure 4.51a. Similarly, MDF samples exhibit a combination of adhesive wear and fewer abrasive grooves, as shown in Figures 4.51b and c.

Figure 4.52 depicts the worn surface morphology of as-cast and MDF-processed Al-12.1Si alloys under load of 19.61 N at sliding speed of 0.7 m/s. Figure 4.52a depicts wear mechanism of as-cast sample under load of 19.81 N at sliding speed of 0.7 m/s. Wear mechanism is combination of adhesion, abrasive, and mild delamination regions.

Worn morphologies are identical to those perceived in Al-7.3Si as-cast alloys for the same load and sliding speed conditions. However, Al-12.1Si as-cast alloys were subjected to less adhesive and delaminated craters compared to Al-7Si as-cast alloys. Wear mechanism of one-cycle samples is found to be a combination of abrasive and adhesion regions, as shown in Figure 4.52b. Moreover, degree of abrasive wear slightly increased after the MDF process. Worn surface of two cycles of MDF-processed samples exhibits more abrasive grooves, as shown in Figure 4.52c. Furthermore, it can be observed that the delaminated crater significantly decreased. However, three-cycle MDF-processed sample (Figure 4.52d) exhibits abrasive wear mechanisms. Similarly, Figure 4.53 exhibits the worn surface morphology of as-cast and MDF-processed Al-12.1Si alloys under load of 39.23 N at sliding speed of 0.7 m/s. With the increase in the applied load from 19.61 N to 39.23 N, the degree of wear becomes more severe in the case of the as-cast alloy, as exhibited in Figure 4.53a. Wear mechanism of the as-cast sample is a combination of the adhesive, delaminated, and abrasive region. The delaminated craters increased with increasing load in as-cast alloys. It can be noted that with increasing applied load, the amount of adhesive wear and delaminated crater are



**Figure 4.52: FE-SEM image of worn surfaces of Al-12.1Si alloy under a load of 19.61 N and at a speed of 0.7 m/s: (a) cast, (b) one cycle, (c) two cycles, and (d) three cycles.**



**Figure 4.53: FE-SEM image of the worn surfaces of Al-12.1Si alloy under a load of 39.23 N and at a speed of 0.7 m/s: (a) cast, (b) one cycle, (c) two cycles, and (d) three cycles.**

slightly increased in one cycle of the MDF-processed sample, which is shown in Figure 4.53b. Wear mechanisms of MDF-processed two-cycle and three-cycle samples are combination of abrasive and adhesive regions, as shown in Figures 4.53c and d. Moreover, wear mechanisms of MDF-processed two- and three-cycle samples are observed to be mainly abrasive wear. The depth of micro-abrasion grooves is found to be deeper with fewer adhesive wear regions at higher loads. Figure 4.54 depicts worn surface morphology of as-cast and MDF-processed Al-12.1Si alloys under applied loads 19.61 N and sliding speed of 2.2 m/s at constant sliding distance of 1500 m. Figure 4.54a shows worn surface of cast sample, which consists of combination of adhesion regions and delamination regions. Figure 4.54b depicts worn surface of one cycle processed MDF samples. After one cycle, worn surface exhibits the features of adhesive wear and mild abrasive wear. With increasing sliding speed, the worn surface is observed to be smoother with fewer abrasion grooves. MDF-processed two-cycle and three-cycle samples (Figures 4.54 c and d) display adhesive and abrasive regions. After two and three cycles of MDF, the abrasive wear is slightly higher compared to one cycle of MDF. In contrast to the lower sliding speed wear condition, very few abrasive grooves appear at higher sliding speeds. Figure 4.55 displays worn surface morphology

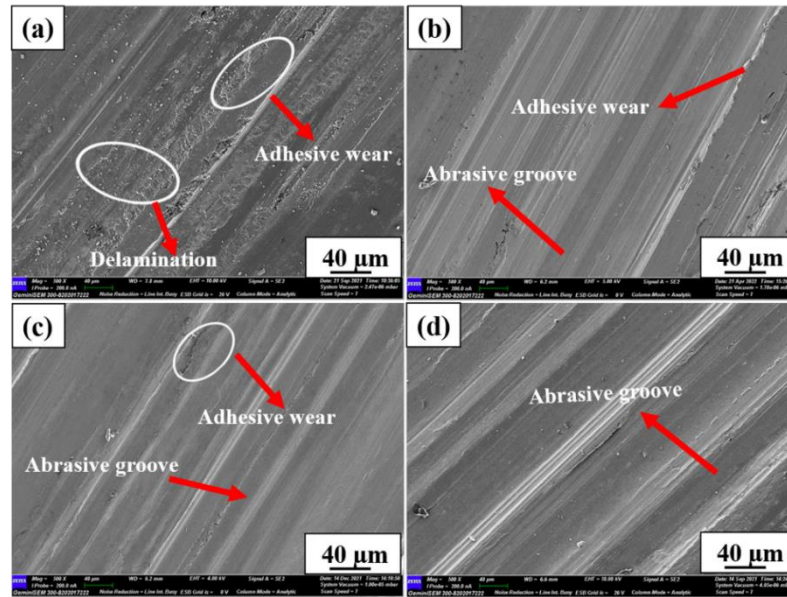


**Figure 4.54: FE-SEM image of the worn surfaces of Al-12.1Si alloy under a load of 19.61 N and at a speed of 2.2 m/s: (a) cast, (b) one cycle, (c) two cycles, and (d) three cycles.**

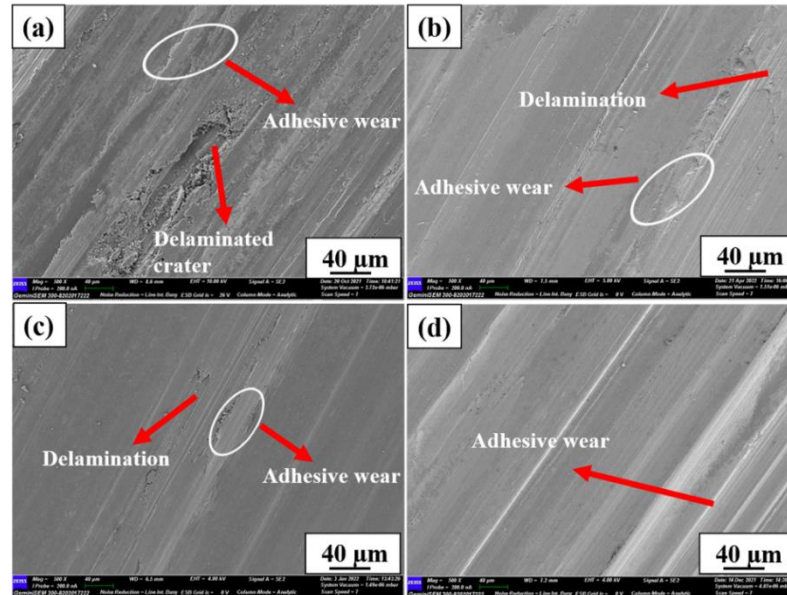


**Figure 4.55: FE-SEM image of the worn surfaces of Al-12.1Si alloy under a load of 39.23 N and at a speed of 2.2 m/s: (a) cast, (b) one cycle, (c) two cycles, and (d) three cycles.**

of as-cast and MDF-processed Al-12.1Si alloys under applied load 39.23 N and sliding speed of 2.2 m/s at constant sliding distance of 1500 m. With increased applied load (39.23 N), the adhesive and delamination regions significantly increased in the as-cast sample, which is depicted in Figure 4.55a. In case of MDF-processed samples, the level of abrasive wear decreases as applied load and speed increase, as shown in Figure 4.55 b–d. However, after two and three cycles of MDF, delaminated craters are significantly reduced in Al-12.1Si alloys.

Figures 4.56a and b show the EDS analysis of worn surfaces of two cycles of MDF-processed Al-7.31Si alloy under varying applied loads (19.61 N and 39.23 N) and sliding speed of 0.7 m/s at constant sliding distance of 1500 m. Presence of oxygen is observed in adherent debris in all wear conditions. It is clear from Figures 4.56a and b that worn surfaces under load of 19.61 N at a sliding speed of 0.7 m/s exhibit slightly more oxide formation compared to the worn surfaces under load of 39.23 N at sliding speed of 0.7 m/s. Average percentage of oxygen is about 21% at a load of 19.81 N and speed of 0.7 m/s. Similarly, after increasing load (39.61 N), average percentage of oxygen is reduced to around 16%. Increase in applied load is sufficient to remove the oxide layer. Similarly, Figures 4.57a and b show the EDS analysis of worn surfaces of two cycles of MDF-processed Al-7.31Si alloy under varying applied loads (19.61 N and 39.23 N) and sliding speed of 2.2 m/s at constant sliding distance of 1500 m. From Figures 4.57a and b, it can be observed that with increase in sliding speed from 0.7 m/s

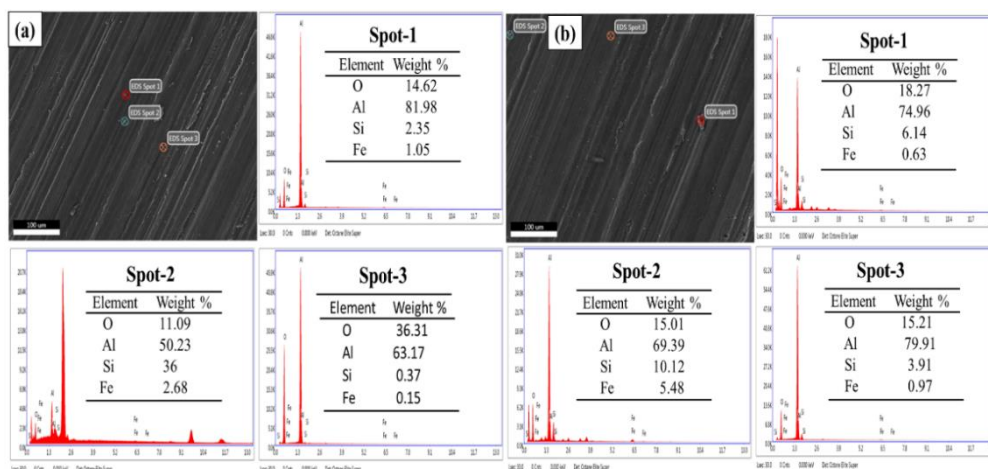


**Figure 4.56: EDS analysis of the worn surfaces of three cycles of Al-7.3Si alloy at a speed of 0.7 m/s: a) Under 19.61 N load; b) Under 39.23 N load.**

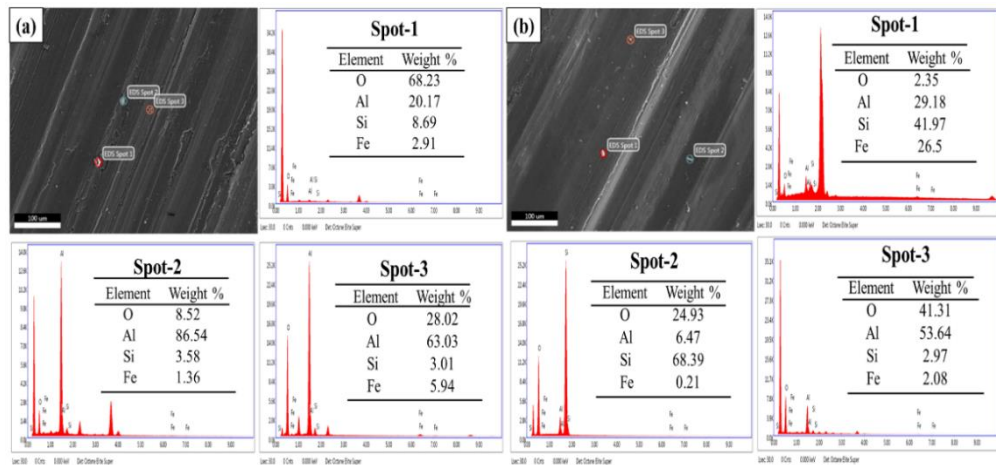


**Figure 4.57: EDS analysis of the worn surfaces of three cycles of Al-7.3Si alloy at a speed of 2.2 m/s: a) Under 19.61 N load; b) Under 39.23 N load.**

to 2.2 m/s, there is increase in the degree of oxide formation. Average percentage of oxygen under load of 19.61 N and sliding speed of 2.2 m/s is around 35%. Increased interference temperatures at higher sliding speeds resulted in increased oxide formation. However, with increasing load from 19.61 N to 39.23 N, average percentage of oxygen is reduced to around 23%. Worn surfaces under the load of 19.61 N at a sliding speed of 2.2 m/s exhibit more oxide formation compared to other wear conditions. Similarly, Figures 4.58a and b show the EDS analysis of worn surfaces of three cycles of MDF-processed Al-12.1Si alloy under two levels of load, 19.61 N and 39.23 N, at a sliding speed of 0.7 m/s and constant sliding distance of 1500 m. From the EDS analysis of worn surfaces (Figure 4.58), it can be noted that worn surfaces under low load show

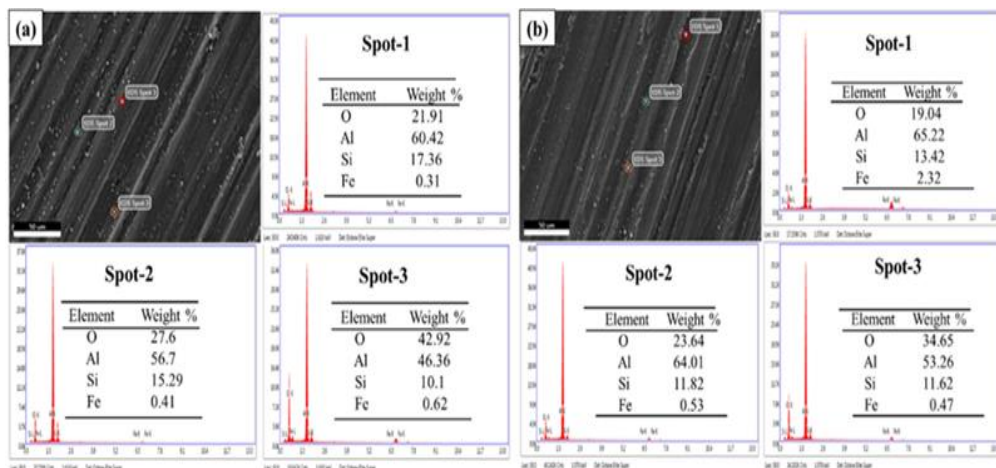


**Figure 4.58: EDS analysis of the worn surfaces of three cycles of Al-12.1Si alloy at a speed of 0.7 m/s: a) Under 19.61 N load; b) Under 39.23 N load.**

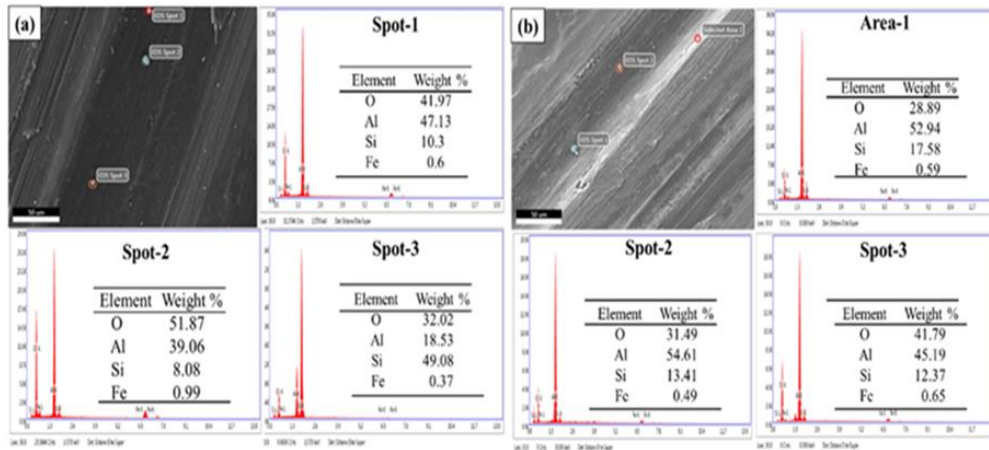


**Figure 4.59: EDS analysis of the worn surfaces of three cycles of Al-12.1Si alloy at a speed of 2.2 m/s: a) Under 19.61 N load; b) Under 39.23 N load.**

higher oxide formation compared to the worn surfaces under high load conditions. Average percentage of oxygen is about 30% under load of 19.61 N, while under load of 39.23 N, it is about 25%. Figure 4.59 shows the EDS analysis of worn surfaces under two levels of load, 19.61 N and 39.23 N, at a sliding speed of 2.2 m/s. With increasing sliding speed, the degree of oxide formation on the worn surface increases. Average percentage of oxide formation on the worn surface is about 42% under low applied loads, while it is about 34% at high loads. Existence of Fe was confirmed, which proves the transfer of Fe from the disc to the pin.

## CHAPTER 5

### DISCUSSION

Multidirectional forging (MDF) was carried out on Al-Si alloys to enhance their mechanical properties. MDF-processed samples were characterised at each cycle of processing. Also, mechanical properties of the MDF-processed samples were assessed. These results are presented in the previous chapter. In this chapter, these results are analysed and discussed in detail. In the present work, Al-7.3Si and Al-12.1Si alloys were processed by MDF at room temperature. Both alloys have been successfully forged by MDF for two cycles and three cycles, respectively. Effects of MDF on microstructural alterations and mechanical properties have also been examined.

MDF-processed samples were characterised by using optical microscope, SEM, and XRD. The material characterization was carried out at each MDF cycle (3 passes). According to microstructure analysis, the as-cast material has dendritic microstructure with needle-shaped sharp and coarse acicular-shaped silicon eutectic particles dispersed in the Al phase. These acicular eutectic silicon particles of Al-7.3Si as-cast alloys changed to spherical shape after solutionizing. Similarly, coarse sharp sharp-edged silicon eutectic particles of Al-12.1Si alloys are blunted after solutionizing. The acicular and sharp edges of silicon are more likely to dissolve/fragmentation during heat treatment (Gupta et al. 2012). The dissolved Si gets precipitated as spherical shape particles once the samples get cooled to ambient temperature after solutionizing. This helps the Si particles undergo the morphological change from long needle-like to spheroidal after heat treatment. Additionally, morphological modification from needle-like to spheroidal after heat treatment, results in increased width. However, only some Si particles are spheroidized, and the remaining have left an elongated morphology with blunted tips. The solution heat treatment followed by multi-directionally forged Al-7.3Si and Al-12.1Si alloys at room temperature showed a significant improvement in microstructure. The coarse eutectic silicon particles are effectively broken into fine particles and uniformly distributed in aluminium phase matrix. With increasing number of cycles, size and inter-particle distance of hard phase (Si) decrease due to continuous fragmentation during MDF processing. The strain imposed on the material during MDF

process is primarily responsible for fine fragmentation of hard silicon phase. Hence, multidirectional room-temperature forging process has remarkable effects on the fragmentation and distribution of Si particles. From the micro-hardness evaluation, as-cast alloys exhibit lower hardness compared to MDF-processed samples in both Al-7.3Si and Al-12.1Si alloys. Furthermore, as-cast Al-Si alloy exhibits more variation in hardness values, which indicates highly scattered hardness distribution inside the as-cast structure. This is mainly due to non-uniform distribution of coarse eutectic Si particles as well as low hardness of Al phase. After solutionizing, hardness is improved in both Al-7.3Si and Al-12.1Si alloys. However, the hardness of Al-7.3Si alloy exhibited better hardness compared to Al-12.1Si alloy after solutionizing. The increased hardness of solutionized Al-7.3Si alloy is result of solid-solution strengthening. In Al-7.3Si alloys, alloying elements like magnesium (0.5%) are dissolved in Al phase during solutionizing because of their higher solubility at elevated temperatures and are retained in aluminium lattice upon rapid cooling. This increases hardness of alloy through solid solution strengthening. Immanuel and Panigrahi (2015) reported that the solid-solution strengthening effect is greatly influenced by the lattice strain. According to Ren et al. (2020), the presence of magnesium in aluminium alloys results in the formation of a solid solution that creates a barrier to dislocation motion. The interaction between solute atoms and dislocations is responsible for the solid solution strengthening effect, which is the result of the lattice distortion caused by the solute atoms. The solute atoms create a local stress field that interacts with the dislocations, making it more difficult for them to move. This results in an increase in the strength and hardness of the material. Therefore, solid-solution strengthening, improved uniformity of hard eutectic silicon distribution in aluminium phase, and morphology of eutectic silicon resulted in increasing hardness in Al-7.3Si alloys (Immanuel & Panigrahi 2015). On the other hand, Al-12.1 Si alloy has very small percentage of magnesium (0.09%) and has lower response to heat treatment compared to Al-7.3Si alloys. However, there is a slight improvement in hardness of solutionized Al-12.1Si alloys due to improved uniformity of eutectic silicon distribution. It is observed that hardness remarkably increases for MDF-processed samples in both Al-7.3Si and Al-12.1Si alloys. Hardness increased with the increasing number of MDF cycles. With increasing number of MDF cycles, hard and brittle eutectic Si particles are

broken into fine particles and redistributed uniformly. Refinement and redistribution of eutectic silicon particles during MDF processing reduce the particle-free zone, which can be observed in microstructure of MDF-processed samples. Also, particle-free zone decreases with increasing MDF cycles. Since hardness is inversely related to free space of particles, hardness values of the samples increase with increasing numbers of passes (Dodanghe et al. 2012). Furthermore, it can be observed that there is no considerable hardness variation from mean value in the examined samples, especially after two forging cycles of Al-7.3Si alloys and three forging cycles of Al-12.1Si alloys, indicating uniformity in the deformation of aluminium phase.

According to tensile properties of Al-7.3Si and Al-12.1Si alloys, as-cast specimen has low ultimate tensile strength (UTS) compared to other alloys. Presence of dendrite formation and large acicular eutectic Si particles in the as-cast microstructure resulted in low ultimate tensile strength. Presence of non-uniformly distributed sharp-edged Si particles in Al-Si alloy acts as a stress riser, leading to localised shearing at an early stage of the plastic deformation, and this could reduce ductility and strength of the specimen. Moreover, large silicon particles tend to break early during plastic deformation of tensile tests, lowering strength and ductility of as-cast alloys (Amirkhanlou et al. 2011). After solutionizing, strength and ductility are increased in both Al-7.3 and Al-12.1Si alloys. Increased strength and ductility in the solutionized sample are due to the change in morphology of sharp-edged eutectic silicon. However, in the case of Al-7.3Si alloys, strength was significantly increased after heat treatment, which resulted from solid-solution strengthening along with morphology of eutectic silicon. Al-12.1Si alloys showed limited morphological modification of eutectic Si particles after solutionizing, resulting in lower tensile strength and ductility (Gupta et al. 2012). Two factors have been considered for the slight increments in ductility and strength of Al-12.1Si alloys after solutionizing. Firstly, morphology of sharp-tipped plate-like eutectic Si particles into blunt particles decreases stress concentration, and secondly, heat treatment reduces the residual stresses (Wang et al. 2015). The change in morphology of sharp-tipped eutectic Si particles to round shape minimises the chance of premature failure, increasing both strength and ductility in solutionized material. It can be noted that tensile strength remarkably increases for MDF-processed specimens

and increases with increasing number of cycles. Progressive fragmentation and better distribution of eutectic Si particles in aluminium phase led to extraordinary improvement in tensile strength after increasing number of cycles. Furthermore, since MDF is conducted at room temperature, high strain was induced in the sample, which led to strain hardening of primary  $\alpha$ -Al phase. Therefore, strain hardening is another factor that affects tensile strength of MDF-processed Al-7.3Si and Al-12Si alloys. Ductility of sample is reduced after the MDF process at room temperature. It is worth to mention that MDF processing significantly strengthens the material without considerable ductility loss compared to the as-cast state.

From the flow properties of Al-7.3Si and Al-12.1, it can be noted that strain hardening exponent ( $n$ ) is increased in both alloys after solutionizing. Furthermore, solutionized sample shows maximum  $n$  value compared to other specimens. Higher strain hardening exponent for these materials shows higher tendency to strain hardening. Materials with higher  $n$ -value are more ductile than those with lower  $n$ -value materials. Therefore, the solutionized samples show comparatively higher ductility than MDF-processed samples. Similarly, strain hardening exponent decreased for MDF specimens and decreased with increasing number of MDF cycles in both Al-7.3Si alloys and Al-12.1Si alloys. Al-7.3Si alloy with two cycles of MDF processing and Al-12.1Si alloy with three cycles of MDF processing shows lower  $n$  value. Lower strain hardening exponent for these materials is indicative of lower tendency to strain hardening. As metals strain harden, their remaining capacity for strain hardening decreases. The strength coefficient of MDF processed materials increased with increasing number of cycles. Al-7.3Si alloy with two cycles of MDF and Al-12.1Si alloy with three cycles of MDF shows higher strength coefficient. In metal forming processes, the strain hardening exponent and strength coefficient are important because they show how a material responds during forging.

From the scratch test standpoint, it is clear that scratch depth increases with increasing load. However, at lower loads, there is no considerable difference between scratch depths of processed and unprocessed materials. As-cast samples exhibit greater scratch depth in both Al-7.3Si and Al-12.1Si alloys. Non-uniform distribution of eutectic silicon and low hardness of Al phase resulted in a higher depth. Improvement in scratch

resistance of solutionized samples is due to improved homogeneity of eutectic silicon distribution in aluminium phase. However, scratch depth of Al-7.3Si alloys significantly decreased after solutionizing. Reduced scratch depth of solutionized Al-7.3Si alloy is the result of solid solution strengthening, the morphology of needle-shaped eutectic Si particles, and their improved uniformity in distribution. MDF-processed Al-7.3Si and Al-12.1Si alloys displayed better scratch resistance compared to as-cast samples. The scratch hardness significantly increased, for Al-7.3Si alloys with two cycles and Al-12.1 alloys with two and three cycles of forging. From the results, MDF-processed materials showed better mechanical properties compared to other samples. Increased mechanical properties of MDF-processed materials are the result of a number of metallurgical parameters, such as breakage of networks of eutectic silicon, breakage of aluminium dendrites, reduction in Si particle size and its uniform distribution, grain refinement, and strain hardening. Size of eutectic silicon and its uniform distribution, as well as the strain hardening of aluminium phase, have a major effect on mechanical properties of MDF-processed materials. Al-7.3Si alloys with two cycles exhibited better mechanical properties than Al-12.1Si alloys with three cycles. Solid-solution strengthening, combined with strain hardening and silicon particle refinement, led to significant improvement in mechanical properties of Al-7.3Si alloy after the heat treatment and MDF process compared to Al-12.1Si alloy (Immanuel & Panigrahi 2015). Since MDF is conducted at ambient temperature, solutes are not thermally activated to diffuse out of Al phase. Hence, solid-solution strengthening also contributed to increasing mechanical properties of the Al-7.3Si alloys.

According to wear properties, wear mass loss decreased with increasing sliding speed in both Al-7.3Si and Al-12.1 Si alloys. It is evident from the EDS examination of worn surfaces of Al-7.3Si and Al-12.1Si alloys that the degree of oxide formation increases due to increased temperature at higher speeds (Dwivedi 2010). This layer will prevent the material surface from further damage, resulting in decreased wear mass loss. Increased temperature of the material due to increased sliding speed leads to oxide formation. Interface temperature (temperatures at contact surfaces of disc and pin) is measured by infrared thermometer. Highest temperatures normally occur at contact surfaces. Interface temperature mainly depends on sliding velocity, normal pressure,

and surrounding temperature. As interface temperature crosses a critical value, mass loss increases due to softening of the sample in subsurface region (Dwivedi 2010). According to Dwivedi (2010), the critical temperature for hypoeutectic and eutectic Al-Si alloys is around 75–80 °C. In the current study, maximum interface temperature was around 40 to 42 °C under maximum load and speed. Furthermore, at low sliding speed, more time is available for formation and growth of micro welds, which increases force required to shear off the micro welds to maintain relative motion and leads to increased wear mass loss. However, at higher speeds, there is less time for growth of micro-welds, leading to lower wear mass loss (Kori & Chandrashekharaiyah 2007). Furthermore, wear caused by abrasive action is due to hard particles that are separated from the sample, as evidenced by the micro-grooves on the worn surface of both materials particularly at lower sliding speeds. There was more loose debris collected on the disc due to lower speed, and this debris gets into the wear zone (the pin-disc interface) and acts as an abrasive particle. Therefore, more micro-grooves formed on worn surfaces at lower sliding speeds. With increasing speed, a worn surface becomes smoother and has fewer abrasive grooves. Also, very little loose debris was collected on the disc, resulting in fewer abrasive grooves. Furthermore, increased oxide formation at higher speeds could also result in a smoother, worn surface (Torabian et al. 1994). Therefore, the formation of oxide and higher sliding speeds could be the reasons for smoother surfaces with fewer abrasive grooves.

## CHAPTER 6

### CONCLUSIONS AND SCOPE OF FUTURE WORK

#### 6.1 Conclusions

The effect of MDF on mechanical and wear properties of Al-7.3Si and Al-12.1Si alloys processed at room temperature was investigated. Al-7.3Si and Al-12.1Si alloys have been successfully forged by MDF for two cycles and three cycles, respectively. Mechanical and wear properties of the material were tested. Based on the obtained results, the following conclusions are drawn:

1. Al-7.3Si and Al-12.1Si alloys exhibit increased ductility after solutionizing. Sharp-tipped Si particles of the as-cast sample are blunted after solution heat treatment.
2. MDF processing at room temperature showed a significant impact on the refinement and distribution of Si particles. The coarse eutectic silicon particles are effectively broken into fine particles and homogeneously distributed. With increased cumulative strain, the size and inter-particle distance of the hard phase (Si) decreased.
3. Based on the XRD pattern, the peak broadening in the XRD pattern of the MDF-treated sample is due to the combined effect of crystallite size and micro-strain.
4. Mechanical properties, such as hardness and tensile strength, are significantly enhanced by MDF at room temperature. After two cycles of MDF, the hardness and tensile strength of the Al-7.3Si as-cast sample increased to 60% and 149%, respectively. Similarly, after three cycles, the hardness and tensile strength of the Al-12.1Si as-cast sample increased to 50% and 98%, respectively. Furthermore, there is less hardness variation as the number of cycles increases.
5. The tensile-tested fracture surfaces of as-cast Al-Si alloys reveal large-sized facets. The fracture surface of the MDF-processed sample is mainly characterised by decreased facets and tearing ridges. However, fracture surfaces of MDF-processed Al-7.3Si alloy exhibit a few dimples with decreased facet size.
6. After solution heat treatment, the strain hardening exponent ( $n$ ) values are increased in both Al-7.3Si and Al-12.1Si alloys. The solution heat treatment

sample has a higher strain hardening exponent compared to the other samples. A higher strain hardening exponent for these materials is indicative of a higher tendency to strain hardening. The strain hardening exponent (n) of Al-7.3Si alloys was increased from 0.19 to 0.22, and similarly, the strain hardening exponent (n) values of Al-12.1Si alloys were increased from 0.14 to 0.16 after solution heat treatment. The strain hardening exponent values of Al-7.3Si alloy with two cycles and Al-12.1Si alloy with three cycles were decreased to 0.05 and 0.06, respectively. However, the Al-7.3Si alloys with two cycles of MDF and the Al-12.1Si alloys with three cycles of MDF showed a higher strength coefficient.

7. Scratch resistance of the MDF-processed material significantly increased with increasing load. Al-7.3Si alloys with two cycles of samples and Al-12.1Si alloys with two and three cycles of samples showed higher scratch resistance, particularly at higher loads.
8. MDF samples showed better wear resistance, which increased with the increased number of cycles. Al-7.3Si alloys with two cycles and Al-12.1Si alloys with three cycles displayed maximum wear resistance. The coefficient of friction of the alloy decreased with an increase in the number of MDF cycles. However, the coefficient of friction did not change significantly despite improvements in the wear resistance of MDF samples, particularly at higher sliding speeds. As-cast samples showed combination delamination, adhesive, and mild abrasive wear, while MDF-processed samples showed abrasive and adhesive wear. Delamination wear is significantly decreased after the MDF process in both alloys.
9. Lower sliding speed results in more abrasion grooves, whereas higher speed results in smoother surfaces with fewer abrasion grooves. Changes in wear mechanisms are caused by the formation of oxide and sliding speed. Abrasive wear is mainly influenced by hard debris that is separated from the sample. Abrasive action is three-body abrasive wear.
10. With the increase in sliding speed from 0.7 m/s to 2.2 m/s, there was a decrease in wear mass loss in all the samples. Reduced wear mass loss at higher sliding speeds could be the result of increased degree of oxide formation and a higher

sliding speed. The degree of oxide formation increased with an increase in speed. However, with increasing speed, worn surface becomes smoother and has fewer abrasive grooves. Moreover, there is less time available for the development of micro welds at higher sliding speeds, which leads to a lower wear mass loss.

11. According to wear mass analysis, wear mass loss is lower at higher sliding speed and lower applied loads, while lower sliding speed and higher applied loads result in more wear mass loss.
12. From the result, Al-7.3Si alloys with two cycles showed slightly better mechanical properties compared to Al-12.1Si alloys with three cycles. The combined effect of solid-solution strengthening, strain hardening, and silicon particle refinement led to a significant increase in the mechanical properties of Al-7.3Si alloy after heat treatment and MDF processing compared to Al-12.1Si alloy.

## 6.2 Scope for the future work

The effect of the multidirectional room temperature forging process on microstructure and mechanical properties of Al-7.3Si and Al-12.1Si alloys with varying cumulative strains was investigated. Microstructural studies were carried out to evaluate how MDF can refine and distribute eutectic silicon in the aluminium phase. Furthermore, the effects of MDF processing on hardness and strength were studied. Fracture analysis was carried out on tensile tested samples. The scratch and wear properties of MDF-processed samples were assessed. Apart from these observations, the following techniques could be studied for further understanding of the effect of MDF on Al-Si alloys:

- 1) Electron back scattered diffraction (EBSD) analysis and texture analysis could be carried out to understand the texture modification involved in the MDF-processed Al-Si alloy.
- 2) The impact and creep behaviour of MDF-processed Al-Si alloy could be studied.
- 3) The corrosion properties of Al-Si alloys before and after MDF processing could be studied.
- 4) The combined effect of chemical modifiers and MDF on the microstructure and mechanical properties of Al-Si alloys can be evaluated.
- 5) The combined effect of annealing and MDF on the mechanical properties of Al-Si alloys can be evaluated.

## LIST OF PUBLICATIONS

### **Journals:**

Kumara B. and Preetham Kumar G. V. (2020). “Investigation on Microstructure and Mechanical Properties of Solution Heat-Treated and Multi Directional Forging-Processed LM-25 Aluminium Alloy”. Transactions of the Indian Institute of Metals 73(6), p 1561–1566.

Kumara B. and Preetham Kumar G. V. (2022). “Influence of Multi-directional Room-Temperature Forging Process on Microstructure and Mechanical Behaviour of Eutectic Al-12Si Alloy”. Metallography, Microstructure, and Analysis (Vol. 11, Issue 2, pp. 175–182). Springer.

Kumara B. and Preetham Kumar G. V. “Effect of Multi-axial Room-Temperature Forging on Scratch Hardness and Wear Properties of Hypoeutectic Al-7.3Si and Eutectic Al-12.1Si Alloys”. Journal of Materials Engineering and Performance, pp.1-11.

### **Conferences presentations:**

Kumara B, &Preetham Kumar, G. V. (2019). “Effect of Multi Directional Forging on the Mechanical properties of Hypoeutectic Aluminium Silicon Alloy” 57th National Metallurgists Day & 73rd Annual Technical Meeting of the Indian Institute of Metals (NMD ATM IIM 2019) 15th to 16th Nov 2019, Thiruvananthapuram Kerala. (Oral)

Kumara B, & Preetham Kumar, G. V. (2019). “Investigation on Microstructure and Mechanical Properties of Solution Heat Treated and MDF Processed LM-25 Aluminium Alloy” 2nd International Conference on Recent Trends in Metallurgy, Materials Science and Manufacturing December 27-28, 2019, NIT Tiruchirappalli Chennai. (Oral)



## REFERENCES

- ASM Handbook Vol 3. (1992). Alloy Phase Diagrams. American Society for Metals.
- Alfred, Z. (2006). "Wear patterns and laws of wear". *J. Theor. Appl. Mech.*, 44(2), 219-253.
- Azushima, A., Kopp, R., Korhonen, A., Yang, D. Y., Micari, F., Lahoti, G. D., Groche, P., Yanagimoto, J., Tsuji, N., Rosochowski, A., & Yanagida, A. (2008). "Severe plastic deformation (SPD) processes for metals". *CIRP Ann. - Manuf. Technol.*, 57, 716–735.
- Ashouri, S., Nili-Ahmadabadi, M., Moradi, M., & Iranpour, M. (2008). "Semi-solid microstructure evolution during reheating of aluminum A356 alloy deformed severely by ECAP". *J. Alloys Compd.*, 466(1-2), 67-72.
- Azmah Hanim, M. A., Chang Chung, S., & Khang Chuan, O. (2011). "Effect of a two-step solution heat treatment on the microstructure and mechanical properties of 332 aluminium silicon cast alloy". *Mater. Des.*, 32, 2334–2338.
- Amirkhanlou, S., Jamaati, R., Niroumand, B., Toroghinejad, M. R. (2011). "Using ARB process as a solution for dilemma of Si and SiCp distribution in cast Al-Si/SiCp composites". *J. Mater. Process. Technol.*, 211(6), 1159–1165.
- Alidokht, S. A., Abdollah-Zadeh, A., Soleymani, S., Saeid, T., Assadi, H. (2012). "Evaluation of microstructure and wear behavior of friction stir processed cast aluminum alloy". *Mater. Charact.*, 63, 90–97.
- Affatato, S., & Brando, D. (2013). "Introduction to wear phenomena of orthopaedic implants". *Wear Orthop. Implant. Artif. Jt.*, pp. 3-26.
- Aal, M. I. A. el, & Kim, H. S. (2014). "Wear properties of high-pressure torsion processed ultrafine grained Al-7%Si alloy". *Mater. Des.*, 53, 373–382.
- Aktarer, S. M., Sekban, D. M., Saray, O., Kucukomeroglu, T., Ma, Z. Y., Purcek, G. (2015). "Effect of two-pass friction stir processing on the microstructure and mechanical properties of as-cast binary Al-12Si alloy". *Mater. Sci. Eng.*, 311–319.

Aktarer, S. M., Sekban, D. M., Yanar, H., & Purcek, G. (2017). “Effect of friction stir processing on tribological properties of Al-Si alloys”. IOP Conference Series: *Mater. Sci. Eng. C* 174(1).

Aoba, T., Kobayashi, M., & Miura, H. (2017). “Effects of aging on mechanical properties and microstructure of multi-directionally forged 7075 aluminium alloy”. *Mater. Sci. Eng. A*, 700, 220–225.

Akbari, M., Shojaeefard, M. H., Asadi, P., & Khalkhali, A. (2017). “Wear Performance of A356 Matrix Composites Reinforced with Different Types of Reinforcing Particles”. *J. Mater. Eng. Perform.*, 26, 4297–4310.

Abdulmalik, S. S., Ahmad, R. (2018). “Influence of friction stir process on microstructure and tensile properties of LM28 hypereutectic Al-Si alloy”. *Int. J. Integr. Eng.*, 10(3), 63–68.

Bhushan, B. (2002). “Introduction to Tribology”. John Wiley & Sons Ltd., United Kingdom.

Bhushan, B. (2012). “Tribology and mechanics of magnetic storage devices”. Springer Science & Business Media.

Cepeda-Jiménez, C. M., García-Infanta, J. M., Zhilyaev, A. P., Ruano, O. A., & Carreño, F. (2011). “Influence of the supersaturated silicon solid solution concentration on the effectiveness of severe plastic deformation processing in Al-7wt.% Si casting alloy”. *Mater. Sci. Eng. A*, 528(27), 7938–7947.

Cho, I. S., Amanov, A., Kwak, D. H., Jeong, B. J., & Park, I. G. (2015). The influence of surface modification techniques on fretting wear of Al-Si alloy prepared by gravity die casting. *Mater. Des (1980-2015)*, 65, 401-409.

Cheng, W., Liu, C. Y., & Ge, Z. J. (2021). “Optimizing the mechanical properties of Al-Si alloys through friction stir processing and rolling”. *Mater. Sci. Eng. A*, 804, 140786.

Dwivedi, D. K. (2004). “Sliding temperature and wear behaviour of cast Al-Si-Mg alloys”. *Mater. Sci. Eng. A*, 382(1–2), 328–334.

- Dwivedi, D. K. (2010). “Adhesive wear behaviour of cast aluminium–silicon alloys: Overview”. *Mater. Des., (1980-2015)*, 31(5), 2517-2531.
- Dodangeh, A., Kazeminezhad, M., & Aashuri, H. (2012). “Severe plastic deformation of rheoforged aluminum alloy A356”. *Mater. Sci. Eng. A*, 558, 371–376.
- Djavanroodi, F., Ebrahimi, M., & Nayfeh, J. F. (2019). “Tribological and mechanical investigation of multi-directional forged nickel”. *Sci. Rep.*, 9(1), 241.
- Damavandi, E., Nourouzi, S., Rabiee, S. M., & Jamaati, R. (2019). “Effect of ECAP on microstructure and tensile properties of A390 aluminum alloy”. *Trans. Nonferrous Met. Soc. China*, (English Edition)29(5), 931–940.
- Estrin, Y., & Vinogradov, A. (2013). “Extreme grain refinement by severe plastic deformation: A wealth of challenging science”. *Acta Mater.*, 61, 782–817.
- García-Infanta, J. M., Zhilyaev, A. P., Cepeda-Jiménez, C. M., Ruano, O. A., Carreño, F. (2008). “Effect of the deformation path on the ductility of a hypoeutectic Al-Si casting alloy subjected to equal-channel angular pressing by routes A, BA, BC and C”. *Scr. Mater.*, 58(2), 138–141.
- Gao, L. L., & Cheng, X. H. (2007). Effect of ECAE on microstructure and tribological properties of Cu–10% Al–4% Fe alloy. *Tribology Letters*, 27, 221-225.
- Gutierrez-Urrutia, I., Muñoz-Morris, M. A., Puertas, I., Luis, C., & Morris, D. G. (2008). “Influence of processing temperature and die angle on the grain microstructure produced by severe deformation of an Al-7% Si alloy”. *Mater. Sci. Eng. A*, 475, 268–278.
- García-Infanta, J. M., Zhilyaev, A. P., Carreño, F., Ruano, O. A., Su, J. Q., Menon, S. K., & McNelley, T. R. (2010). “Strain path and microstructure evolution during severe deformation processing of an as-cast hypoeutectic Al–Si alloy”. *J. Mater. Sci.*, 45, 4613-4620.
- Gupta, A. K., Prasad, B. K., Pajnoo, R. K., & Das, S. (2012). “Effects of T6 heat treatment on mechanical, abrasive and erosive-corrosive wear properties of eutectic Al-Si alloy”. *Trans. Nonferrous Met. Soc. China* (English Edition), 22(5), 1041–1050.

Gode, C., Yilmazer, H., Ozdemir, I., & Todaka, Y. (2014). "Microstructural refinement and wear property of Al-Si-Cu composite subjected to extrusion and high-pressure torsion". *Mater. Sci. Eng. A*, 618, 377–384.

Golafshani, K. B., Nourouzi, S., Jamshidi Aval, H. (2019). "Evaluating the microstructure and mechanical properties of friction stir processed Al–Si alloy". *Mater. Sci. Technol.*, (United Kingdom)35(9), 1061–1070.

Gebril, M. A., Omar, M. Z., Mohamed, I. F., & Othman, N. K. (2019). "Microstructural evaluation and corrosion resistance of semisolid cast a356 alloy processed by equal channel angular pressing". *Metals*, 9(3), 303.

Hokkirigawa, K., & Kato, K. (1988). "An experimental and theoretical investigation of ploughing, cutting and wedge formation during abrasive wear". *Tribol. Int.* 21(1), 51–57.

Hegde, S., & Prabhu, K. N. (2008). "Modification of eutectic silicon in Al–Si alloys". *J. Mater. Sci.*, 43, 3009–3027.

Haghdadi, N., Zarei-Hanzaki, A., Abedi, H. R., Abou-Ras, D., Kawasaki, M., Zhilyaev, A. P. (2016). "Evolution of microstructure and mechanical properties in a hypoeutectic Al-Si-Mg alloy processed by accumulative back extrusion". *Mater. Sci. Eng.*, 651, 269–279

Haghdadi, N., Zarei-Hanzaki, A., Kawasaki, M., Phillion, A. B., & Hodgson, P. D. (2017). "Effect of severe plastic deformation and subsequent silicon spheroidizing treatment on the microstructure and mechanical properties of an Al–Si–Mg alloy". *Adv. Eng. Mater.*, 19(7), 1700064.

Hosseinzadeh, A., Radi, A., Richter, J., Wegener, T., Sajadifar, S. V., Niendorf, T., & Yapici, G. G. (2021). "Severe plastic deformation as a processing tool for strengthening of additive manufactured alloys". *J. Manuf. Process.*, 68, 788–795.

Immanuel, R. J., & Panigrahi, S. K. (2015). "Influence of cryorolling on microstructure and mechanical properties of a cast hypoeutectic Al-Si alloy". *Mater. Sci. Eng. A* 640, 424–435.

- Immanuel, R. J., & Panigrahi, S. K. (2016). "Transformation of cast A356 ingots to wrought sheets with enhanced mechanical and tribological properties by different thermo-mechanical processing routes". *Mater. Des.*, 101, 44-55.
- Jorstad, J., & Apelian, D. (2009). "Hypereutectic Al-Si alloys: practical casting considerations". *Int. J. Met.*, 3, 13-36.
- Jamaati, R., Amirkhanlou, S., Toroghinejad, M. R., & Niroumand, B. (2011). "Significant improvement of semi-solid microstructure and mechanical properties of A356 alloy by ARB process". *Mater. Sci. Eng. A*, 528, 2495–2501.
- Jandaghi, M. R., Pouraliakbar, H., Khalaj, G., Khalaj, M. J., & Heidarzadeh, A. (2016). "Study on the post-rolling direction of severely plastic deformed Aluminum-Manganese-Silicon alloy". *Arch. Civ. Mech. Eng.*, 16, 876–887.
- Kim, J. C., Nishida, Y., Arima, H., Ando, T. (2003). "Microstructure of Al-Si-Mg alloy processed by rotary-die equal channel angular pressing". *Mater. Lett.* 57(11), 1689–1695.
- Kato, K. (2005). "Classification of wear mechanisms/models". *Wear: Mater Mech Pract.*, 9-20.
- Kume, Y., Kobashi, M., & Kanetake, N. (2006). "Microstructure refinement of Al-Si alloy using compressive torsion processing". *Mater. Sci. Forum*, (Vol. 519, pp. 1441-1446).
- Kori, S. A., & Chandrashekharaiah, T. M. (2007). "Studies on the dry sliding wear behaviour of hypoeutectic and eutectic Al-Si alloys". *Wear*, 263, 745–755.
- Kucukomeroglu, T. (2010). "Effect of equal-channel angular extrusion on mechanical and wear properties of eutectic Al–12Si alloy". *Mater. Des.*, 31(2), 782-789.
- Kavosi, J., Saei, M., Kazeminezhad, M., & Dodangeh, A. (2014). "Modeling of dislocation density and strength on rheoforged A356 alloy during multi-directional forging". *Comput. Mater. Sci.* 81, 284–289.

Kandeva-Ivanova, M., Vencl, A., & Karastoyanov, D. (2016). “Advanced tribological coatings for Heavy-duty applications: Case studies”. Sofia: Prof. Marin Drinov Publishing House of Bulgarian Academy of Sciences, pp. 1-147.

Kumar, P., Kawasaki, M., Langdon, T. G. (2017). “Resolving the strength-ductility paradox through severe plastic deformation of a cast Al-7% Si alloy”. *Mater. Sci. Forum*, 879, 1043–1048.

Lowe, T. C., & Valiev, R. Z. (2004). “The use of severe plastic deformation techniques in grain refinement”. *Jom*, 56, 64-68.

Li, X. P., Wang, X. J., Saunders, M., Suvorova, A., Zhang, L. C., Liu, Y. J., ... & Sercombe, T. B. (2015). “A selective laser melting and solution heat treatment refined Al–12Si alloy with a controllable ultrafine eutectic microstructure and 25% tensile ductility”. *Acta Mater.*, 95, 74-82.

Lin, G. Y., Tan, X., Feng, D., Wang, J. L., & Lei, Y. X. (2019). “Effects of conform continuous extrusion and heat treatment on the microstructure and mechanical properties of Al–13Si–7.5 Cu–1Mg alloy”. *Int. J. Miner. Metall.*, 26, 1013-1019.

Ma, A., Saito, N., Takagi, M., Nishida, Y., Iwata, H., Suzuki, K., ... & Watazu, A. (2005). “Effect of severe plastic deformation on tensile properties of a cast Al–11 mass% Si alloy”. *Mater. Sci. Eng. A*, 395(1-2), 70-76.

Ma, Z. Y., Sharma, S. R., & Mishra, R. S. (2006). “Microstructural modification of as-cast Al-Si-Mg alloy by friction stir processing”. *Metall. Mater. Trans.*, 37, 3323-3336.

Morris, M. M., Gutierrez-Urrutia, I., & Morris, D. G. (2008). “The effect of geometrically necessary dislocations on grain refinement during severe plastic deformation and subsequent annealing of Al–7% Si”. *Mater. Sci. Eng. A*, 493(1-2), 141-147.

Mungole, T., Nadammal, N., Dawra, K., Kumar, P., Kawasaki, M., & Langdon, T. G. (2013). “Evolution of microhardness and microstructure in a cast Al–7% Si alloy during high-pressure torsion”. *J. Mater. Sci.*, 48, 4671-4680.

- Mahmoud, T. S. (2013). "Surface modification of A390 hypereutectic Al–Si cast alloys using friction stir processing". *Surf. Coat. Technol.*, 228, 209-220.
- Miura, H., Kobayashi, M., & Benjanarasuth, T. (2016). "Effects of strain rate during multi-directional forging on grain refinement and mechanical properties of AZ80Mg alloy". *Mater. Trans.*, 57, 1418–1423.
- Meenia, S., Khan, F., Babu, S., Immanuel, R. J., Panigrahi, S. K., & Ram, G. J. (2016). "Particle refinement and fine-grain formation leading to enhanced mechanical behaviour in a hypo-eutectic Al–Si alloy subjected to multi-pass friction stir processing". *Mater. Charact.*, 113, 134-143.
- Mahallawy, N. E., Fathy, A., Hassan, M., & Abdelaziem, W. (2017). "Evaluation of mechanical properties and microstructure of Al/Al–12% Si multilayer via warm accumulative roll bonding process". *J. Compos. Mater.*, 0021998317692141.
- Nishida, Y., JIANG, J. H., Saito, N., Shigematsu, I., & Watazu, A. (2007). "Deformation mechanism at impact test of Al-11% Si alloy processed by equal-channel angular pressing with rotary die". *Trans. Nonferrous Met. Soc. China*, 17(1), 104-109
- Natori, K., Utsunomiya, H., & Tanaka, T. (2017). "Improvement in formability of semi-solid cast hypoeutectic Al-Si alloys by equal-channel angular pressing". *J. Mater. Process. Technol.*, 240, 240–248.
- Omran, A. M., Wasly, H. S., & Kh, M. M. (2017). A review on advanced challenges for improvement the mechanical properties of Al-Si alloy automotive parts. *JETIR* Volume 4, Issue 11.
- Pippan, R., Scheriau, S., Hohenwarter, A., & Hafok, M. (2008). "Advantages and limitations of HPT: A review". *Mater. Sci. Forum.*, 584-586 PART I, 16–21.
- Purcek, G., Saray, O., Kul, O. (2010). "Microstructural evolution and mechanical properties of severely deformed Al-12Si casting alloy by equal-channel angular extrusion". *Met. Mater. Int.* 16(1), 145–154.
- Reddy, G. M., Rao, K. S. (2010). "Enhancement of wear and corrosion resistance of cast A356 aluminium alloy using friction stir processing". *Trans. Indian Inst. Met.* (Vol. 63).

Rosochowski, A., & Olejnik, L. (2012). “Severe plastic deformation for grain refinement and enhancement of properties”. *Microstruct. Evol. Met. Form. Process*, pp114–14.

Rao, P. N., Singh, D., & Jayaganthan, R. (2014). “Mechanical properties and microstructural evolution of Al 6061 alloy processed by multidirectional forging at liquid nitrogen temperature”. *Mater. Des.*, 56, 97–104.

Rajender, G., & Giri, P. K. (2016). Strain induced phase formation, microstructural evolution and bandgap narrowing in strained TiO<sub>2</sub> nanocrystals grown by ball milling. *J. Alloys Compd.* . 676, 591-600.

Richmire, S., & Haghshenas, M. (2019). “Friction stir welding of a hypoeutectic Al–Si alloy: microstructural, mechanical, and cyclic response”. *Int. J. Adv. Manuf. Technol*, 101, 3001-3019.

Ramesh, S., Nayaka, H. S., Sahu, S., Gopi, K. R., Shivaram, M. J., & Arya, S. (2019). “Influence of Multiaxial Cryoforging on Microstructural, Mechanical, and Corrosion Properties of Copper-Titanium Alloy”. *J. Mater. Eng. Perform.*, 28, 7629–7641.

Ren, S., Li, J., Fang, Q. and Feng, H., (2020). Effect of solid solution addition on the dislocation emission in aluminium alloys. *Acta Mech* 231(11), pp.4537-4545.

Salishchev, G., Rzaripova, Rgaleev, O., Valiakhmetov. (1995). “Nanocrystalline structure formation during severe plastic deformation in metals and their deformation behaviour”. *Nanostruct Mater.*, 6, 913-916.

Saito, Y., Tsuji, N., Utsunomiya, H., Sakai, T., & Hong, R. G. (1998). “Ultra-fine grained bulk aluminum produced by accumulative roll-bonding (arb) process”. *Scr. Mater.*, 39, 1221-1227.

Selin, M. (2010). Comparing three equations used for modelling the tensile flow behaviour of compacted graphite cast irons at elevated temperatures. *Metall. Mater. Trans. A*, 41(11), pp.2805-2815.

Sharma, S. R., Ma, Z. Y., Mishra, R. S. (2004). “Effect of friction stir processing on fatigue behavior of A356 alloy”. *Scr. Mater.*, 51(3), 237–241.

- Sergici, A. O., & Randall, N. X. (2006). "Scratch testing of coatings". *Adv. Mater. Process*, 164(4), 41-44.
- Sjölander, E., & Seifeddine, S. (2010). "The heat treatment of Al–Si–Cu–Mg casting alloys". *J. Mater. Process. Technol.* 210(10), 1249-1259.
- S. A., Abdollah-Zadeh, A., Soleymani, S., Saeid, Assadi, H. (2012). "Evaluation of microstructure and wear behavior of friction stir processed cast aluminum alloy". *Mater. Charact.*, 90–97.
- Sakai, T., Belyakov, A., Kaibyshev, R., Miura, H., & Jonas, J. J. (2014). "Dynamic and post-dynamic recrystallization under hot, cold and severe plastic deformation conditions". *Prog. Mater. Sci.*, 60, 130–207.
- Syukron, M., Ojima, M., Seman, A. A., Hussain, Z., Koseki, T. (2016). "Mechanical Properties of 1.5wt.% TiB<sub>2</sub>-added Hypoeutectic Al-Mg- Si Alloys Processed by Equal Channel Angular Pressing". *Procedia Chem.*, 19 106–112.
- Shah, P., Bhavsar, V., & Chaudhary, M. (2016). "Feasibility study of nickel-based coating on LM-25 aluminum alloy". *Int J. Eng. Tech. Res.*, 4, 143-146.
- Singh, S. K., Immanuel, R. J., Babu, S., Panigrahi, S. K., & Janaki Ram, G. D. (2016). "Influence of multi-pass friction stir processing on wear behaviour and machinability of an Al-Si hypoeutectic A356 alloy". *J. Mater. Process. Technol.*, 236, 252–262.
- Sun, H., Yang, S., & Jin, D. (2018). Improvement of microstructure, mechanical properties and corrosion resistance of cast Al–12Si alloy by friction stir processing. *Trans. Indian Inst. Met.*, 71, 985-991.
- Syukron, M., Hussein, Z., & Seman, A. A. (2019). "Wear Resistance of Pre-ECAP Annealing A356 Al Alloy with 1.5 Wt.% TiB<sub>2</sub>". *Mater. Sci. Forum.*, 961,118–125.
- Stawiarz, M., Kurtyka, P., Rylko, N., & Gluzman, S. (2019). "Influence of FSP process modification on selected properties of Al-Si-Cu/SiCp composite surface layer". *Compos. Theory Pract*, 19, 161-168.
- Torabian, H., Pathak, J. P., & Tiwari, S. N. (1994). Wear characteristics of Al-Si alloys. *Wear*, 172(1), 49-58.

- Thuong, N. van, Zuhailawati, H., Seman, A. A., Huy, T. D., & Dhindaw, B. K. (2015). "Microstructural evolution and wear characteristics of equal channel angular pressing processed semi-solid-cast hypoeutectic aluminum alloys". *Mater. Des.*, 67, 448–456.
- Ujjwal Kumar., Ajay Kumar Mishra and Rajkumar Ohdar.(2014) "Hot Forging Lubricants", *Int. J. Mech. Eng. & Rob. Res.* Vol. 3, No. 4, ISSN 2278 – 0149.
- Valiev, R. Z., Islamgaliev, R. K., & Alexandrov, I. V. (2000). "Bulk nanostructured materials from severe plastic deformation". *Prog. Mater. Sci.*, 45(2), 103-189.
- Valiev, R. Z., & Langdon, T. G. (2006). "Principles of equal-channel angular pressing as a processing tool for grain refinement". *Prog. Mater. Sci.*, 51(7), 881-981.
- Vencl, A., Manić, N., Popovic, V., & Mrdak, M. (2010). "Possibility of the abrasive wear resistance determination with scratch tester". *Tribol. Lett.* 591–604.
- Venkateswarlu, K., Rajinikanth, V., Sen, M. K., Alhajeri, S. N., Langdon, T. G. (2011). "Application of high-pressure torsion to Al-Si alloys with and without scandium additions". *Mater. Sci. Forum*, 667–669, 743–748.
- Vijeesh, V., & Prabhu, K. N. (2014). Review of microstructure evolution in hypereutectic Al-Si alloys and its effect on wear properties. *Trans. Indian Inst. Met.*, 67(1), 1–18.
- Wang, S. R., Ma, R., Wang, Y. Z., Wang, Y., & Yang, L. Y. (2012). "Growth mechanism of primary silicon in cast hypoeutectic Al-Si alloys". *Trans. Nonferrous Met. Soc. China* (English Edition) (6), 1264–1269.
- Wang, X., Nie, M., Wang, C. T., Wang, S. C., & Gao, N. (2015). "Microhardness and corrosion properties of hypoeutectic Al-7Si alloy processed by high-pressure torsion". *Mater. Des.*, 83, 193–202.
- Wu, Y., Liao, H., & Lü, C. (2019). "Dynamic precipitation and recrystallization in Al-12.5 wt% Si-0.6 wt% Mg-0.1 wt% Ti alloy during hot-rolling and their impacts on mechanical properties". *J. Alloys Compd.*, 788, 125-135.

- Ye, H. (2003). “An overview of the development of Al-Si-alloy based material for engine applications”. *J. Mater. Eng. Perform.*, 12, 288-297.
- Yoon, S. C., Hong, S. J., Hong, S. I., & Kim, H. S. (2007). “Mechanical properties of equal channel angular pressed powder extrudates of a rapidly solidified hypereutectic Al-20 wt% Si alloy”. *Mater. Sci. Eng. A*, 449, 966-970.
- Zhilyaev, A. P., García-Infanta, J. M., Carreño, F., Langdon, T. G., & Ruano, O. A. (2007). “Particle and grain growth in an Al–Si alloy during high-pressure torsion”. *Scr. Mater.*, 57(8), 763-765.
- Zhilyaev, A. P., & Langdon, T. G. (2008). “Using high-pressure torsion for metal processing: Fundamentals and applications”. *Prog. Mater. Sci.*, 53, 893–979.
- Zak, A.K., Majid, W.A., Abrishami, M.E. and Yousefi, R., (2011). X-ray analysis of ZnO nanoparticles by Williamson–Hall and size–strain plot methods. *Solid State Sci.* 13(1), pp.251-256.
- Zhu, Q. F., Lei, L. I., Ban, C. Y., Zhao, Z. H., Zuo, Y. B., & Cui, J. Z. (2014). “Structure uniformity and limits of grain refinement of high purity aluminum during multi-directional forging process at room temperature”. *Trans. Nonferrous Met. Soc. China*, 24(5), 1301-1306.
- Zhuo, X., Xu, H., Wu, Y., Hu, Z., Jiang, J., & Ma, A. (2021). Effect of eutectic Si size on the flow behavior and hot processing map of near eutectic Al–Si alloys. *J. Mater. Res.*, 15, 5694-5705.



## APPENDIX – I

### Multi-directional die design

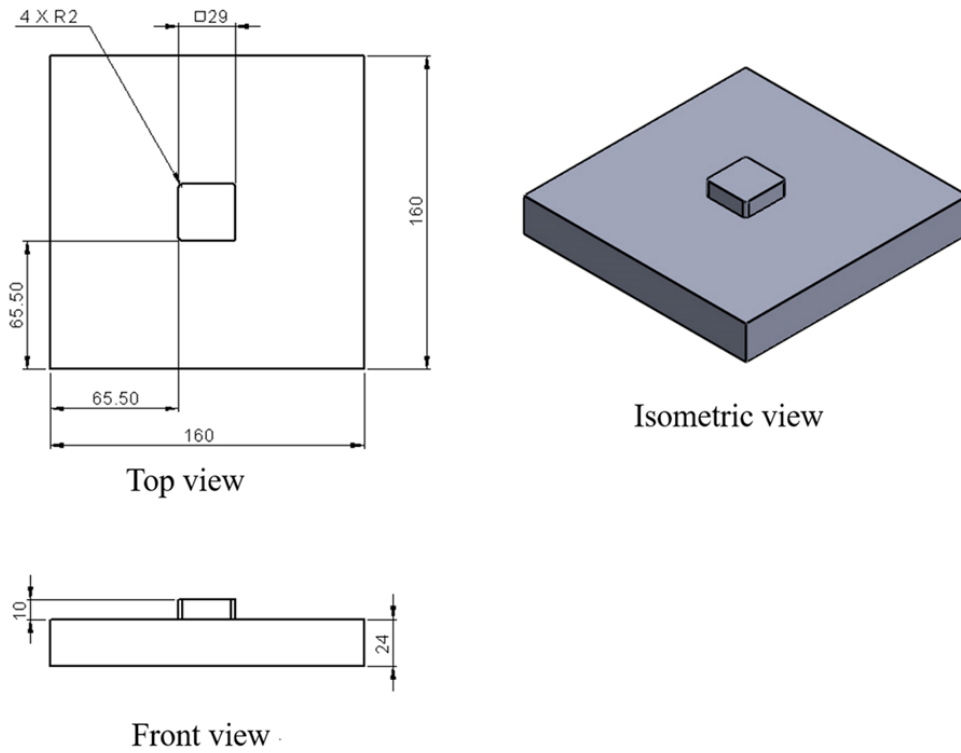


**Figure A1-1: Two-dimensional diagram of MDF base plate in different views (Note: All dimensions are in mm)**

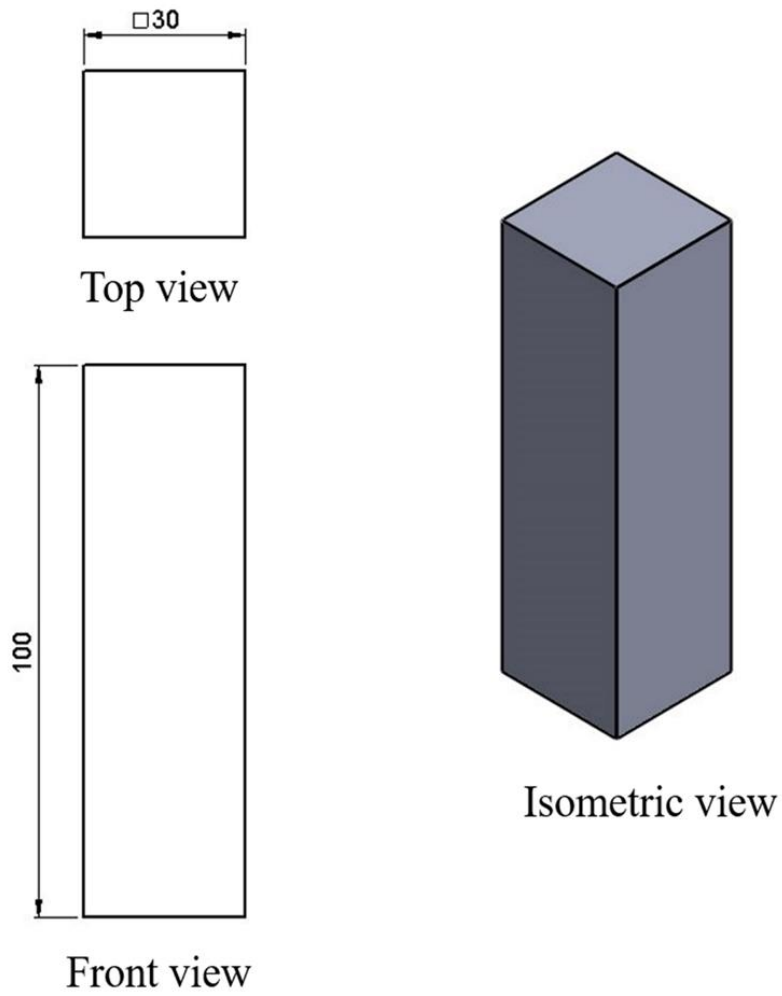


**Figure A1-2: Two-dimensional diagram of MDF Plunger in different views (Note: All dimensions are in mm)**

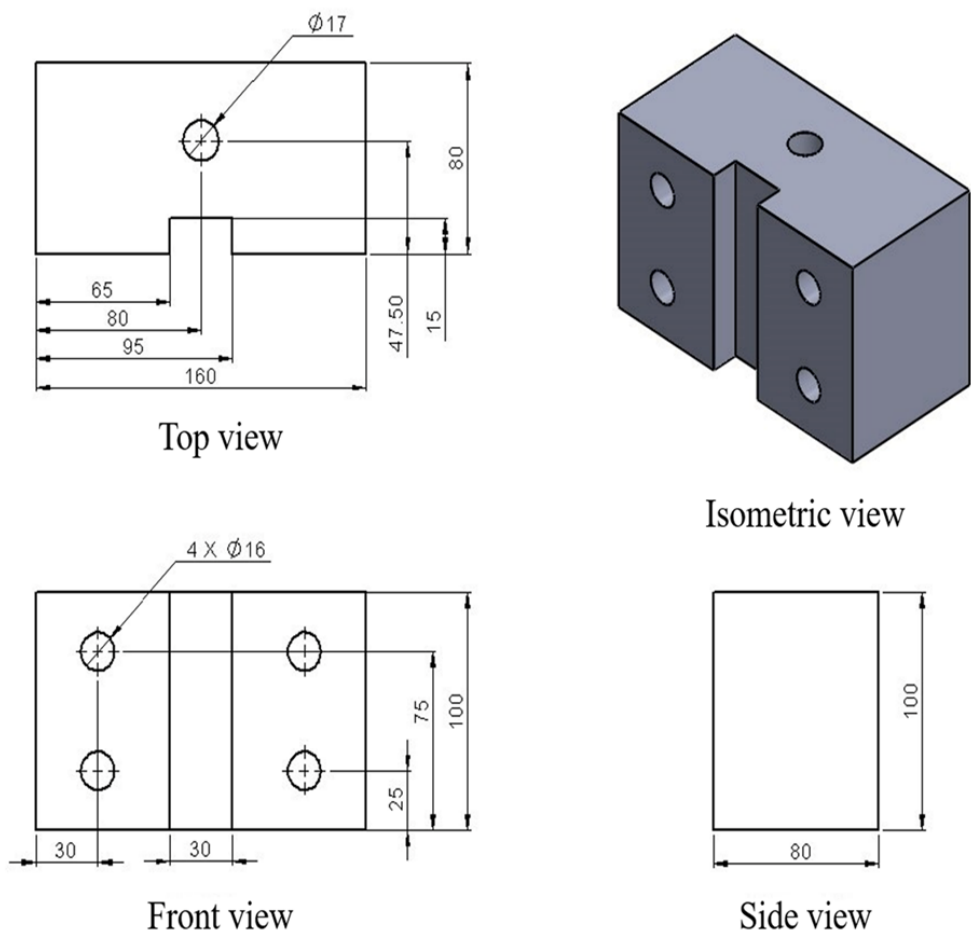
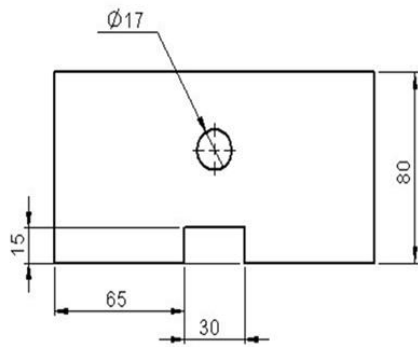
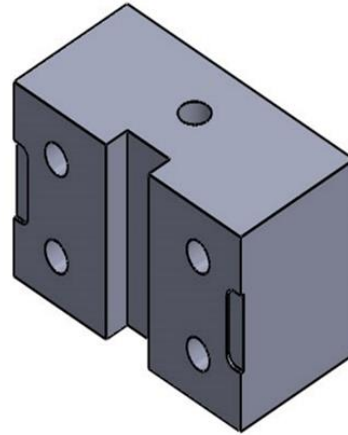


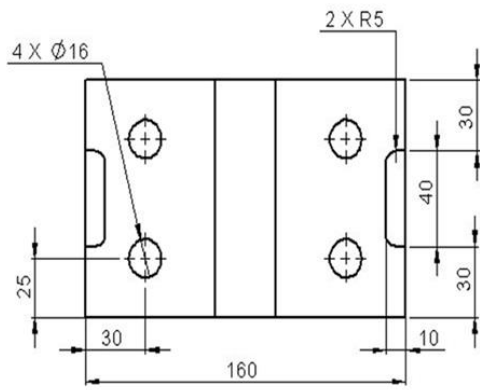
**Figure A1-3: Two-dimensional diagram of MDF split sections (part-1)  
in different views (Note: All dimensions are in mm)**



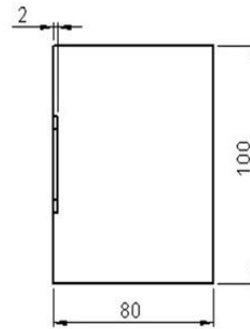
Top view



Isometric view



Front view



Side view

**Figure A1-4: Two-dimensional diagram of MDF split sections(part-2)  
in different views (Note: All dimensions are in mm)**

## APPENDIX – II

### Casting die design

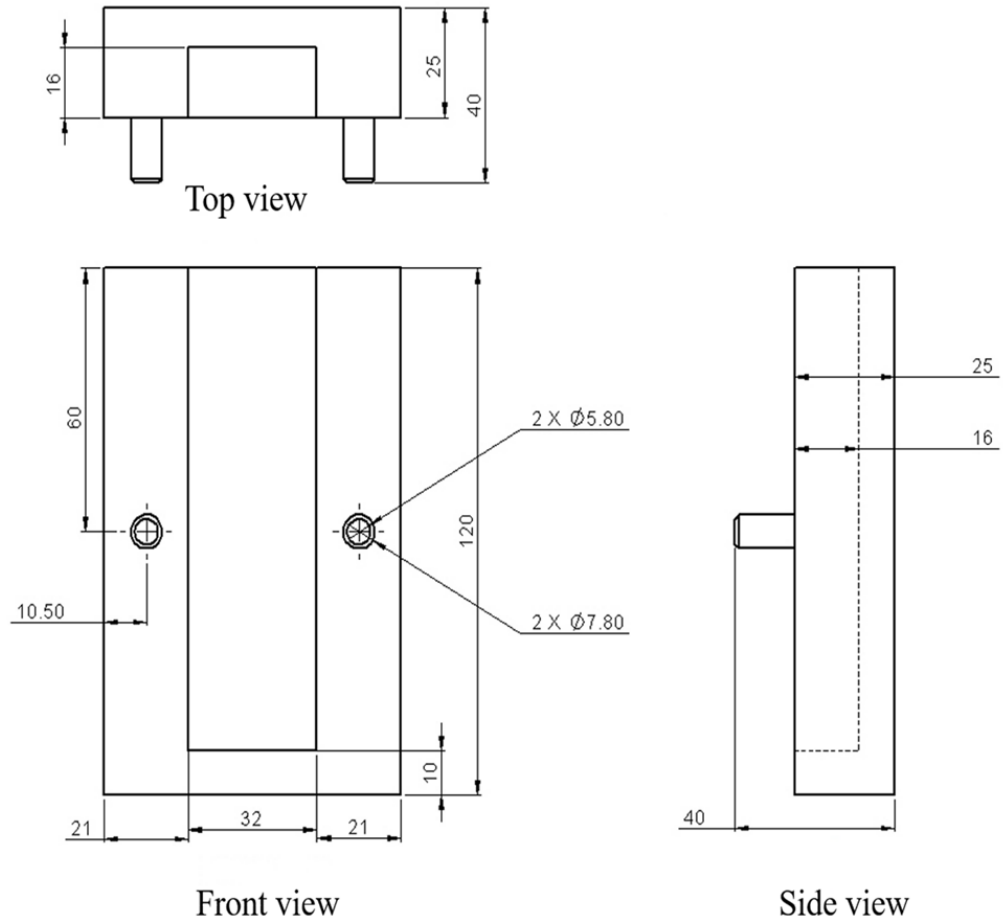


**Figure A2-1: Two-dimensional diagram of Casting die split sections(part-1) in different views (Note: All dimensions are in mm)**

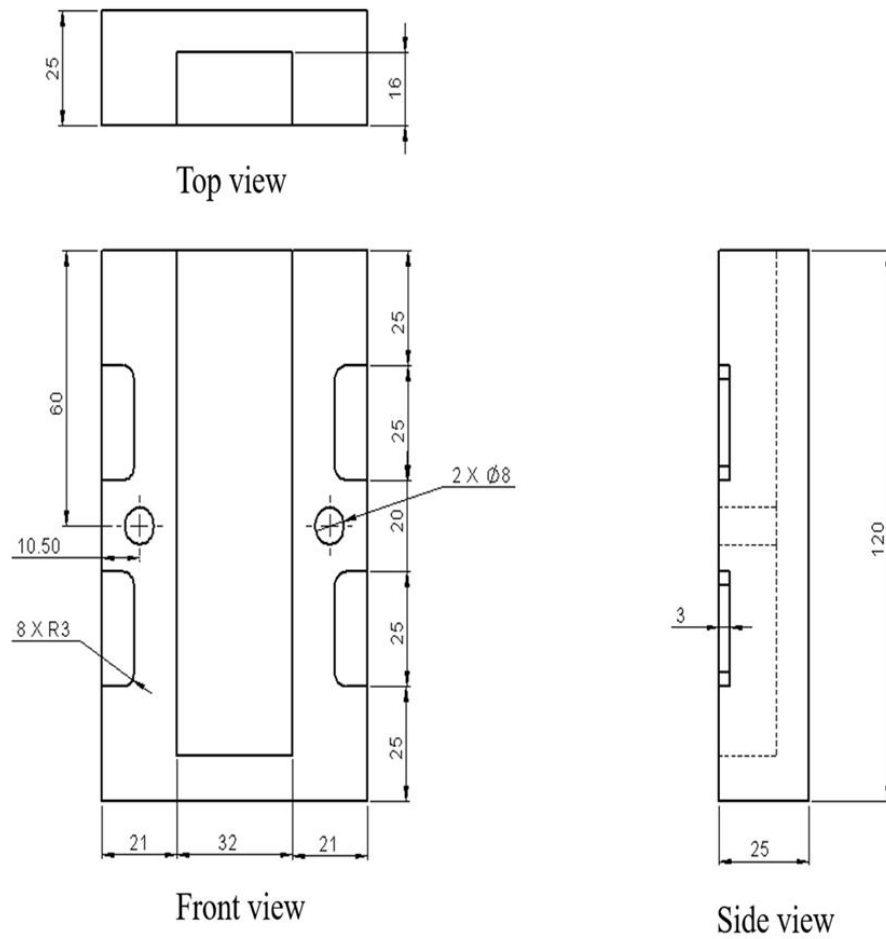


**Figure A2-2: Two-dimensional diagram of Casting die split sections(part-2)  
in different views (Note: All dimensions are in mm)**

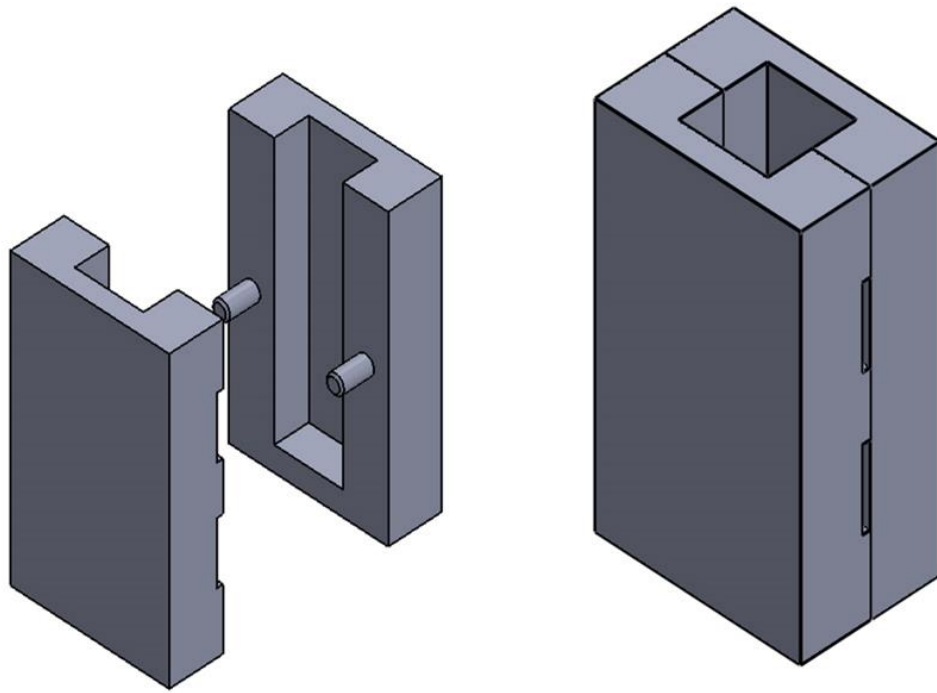


**Figure A2-3: Schematic three-dimensional representation of the casting die**



## APPENDIX – III

### 1. Microstructure of ingot and as-cast al-7.3si alloys

Figure 4.1 depicts an optical micrograph of ingot and as-cast Al-7.3Si alloys. Figure 4.1a and b shows the microstructure of Al-7.3Si ingot samples at lower magnification and higher magnification. Average length of acicular eutectic Si particles is  $24.5\ \mu\text{m}$  and average width is  $3.4\ \mu\text{m}$ . Similarly, Figures 4.1c and d show the microstructure of as-cast sample at lower and higher magnifications. Average length of acicular eutectic Si particles is  $17\ \mu\text{m}$  and average width is  $1.9\ \mu\text{m}$ . It can be observed that coarse eutectic Si particles are reduced to some extent after die casting, which was presented in Al-Si ingots. Further, casting defects like the porosity of the Al-Si ingot alloys were reduced.

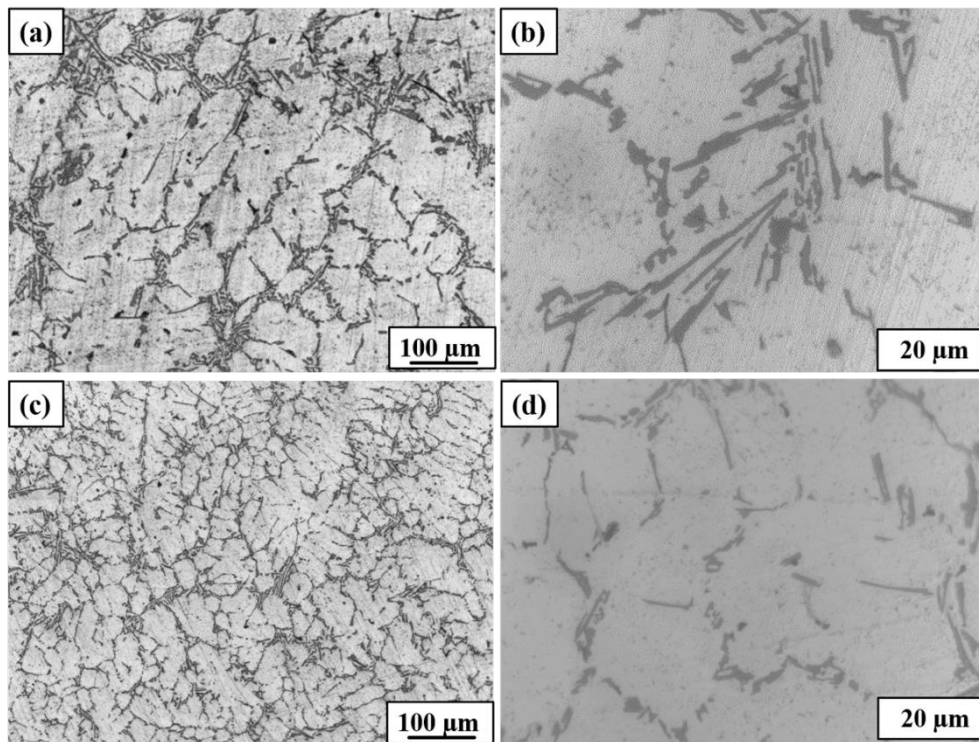


**Figure A3-1: Optical micrograph of Al-7.3Si samples (a, b) Ingot; (c, d) as-cast**

## 2. Microstructure of ingot and as-cast Al-12.1Si alloys

An optical micrograph of ingot and as-cast Al-7.3Si alloys is shown in Figure 4.1. Al-7.3Si ingot samples' microstructure is depicted in Figures 4.1a and b at different magnifications (lower and higher). Average length and width of acicular eutectic Si particles are 24.5  $\mu\text{m}$  and 3.4  $\mu\text{m}$ , respectively. Figures 4.1c and d show the microstructure of an as-cast sample at lower and higher magnifications, respectively. Average length and width of acicular eutectic Si particles are 17  $\mu\text{m}$  and 1.9  $\mu\text{m}$ , respectively. Similarly, in Al-12.1Si alloys, the coarse eutectic Si particles of Al-Si ingots are reduced after die casting.

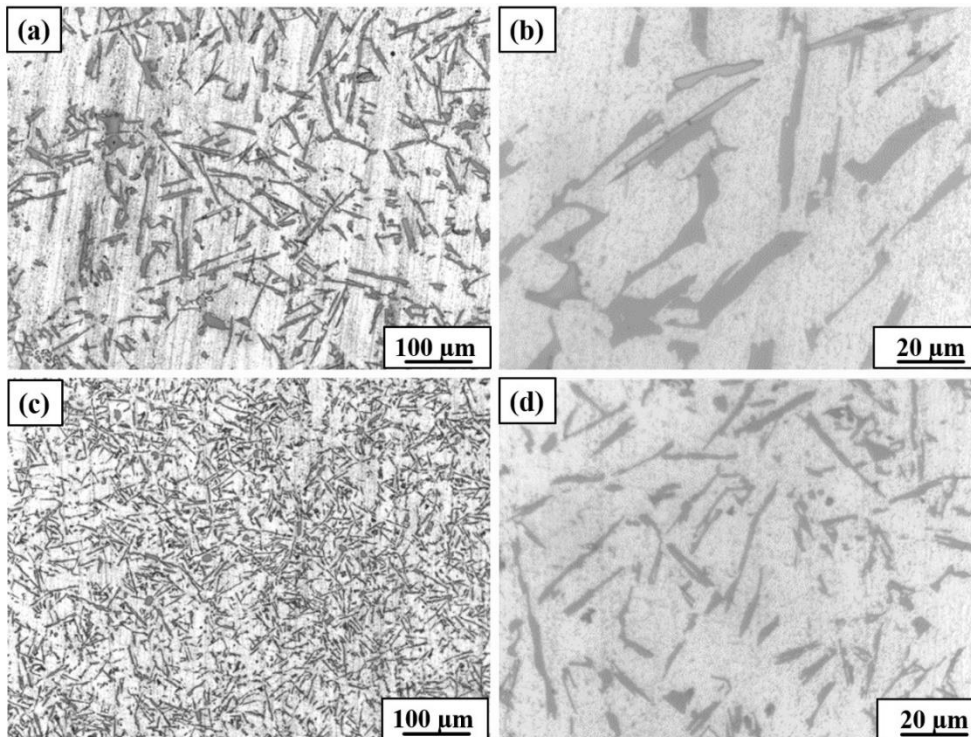


**Figure A3-2: Optical micrograph of Al-12.1Si samples (a, b) Ingot;  
(c, d) as-cast**

## APPENDIX – IV

### Mechanical property tables

**Table A4-1: Summary of hardness and tensile strength of Al-7.3Si alloys in various conditions**

<b>Processing condition</b>	<b>Microhardness (Hv)</b>	<b>Ultimate tensile strength (MPa)</b>	<b>Elongation to Failure (percentage )</b>
<b>As-cast</b>	78.4±6.2	177	7.5
<b>Solutionized</b>	89±2.9	298	11.7
<b>MDF 1 cycle</b>	95±1.6	373	5.5
<b>MDF 2 cycles</b>	125±1.3	441	5.6

**Table A4-2: Summary of hardness and tensile strength of Al-12.1Si alloys in various conditions**

<b>Processing condition</b>	<b>Microhardness (Hv)</b>	<b>Ultimate tensile strength (MPa)</b>	<b>Elongation to Failure (percentage)</b>
<b>As-cast</b>	66.6 ± 3.6	192	5.6
<b>Solutionized</b>	68.6 ±2.3	208	7.7
<b>MDF 1 cycle</b>	87.5 ±2	285	5.5
<b>MDF 2 cycles</b>	95.5 ±1.7	353	5.3
<b>MDF 3 cycles</b>	66.6 ± 3.6	192	5.6

**Table A4-3: Summary of strength coefficient and strain hardening exponent of Al-7.3Si alloys in various conditions**

<b>Processing condition</b>	<b>Strain hardening exponent (n)</b>	<b>Strength coefficient (K), MPa</b>
As-cast	0.19	337
Solutionized	0.22	412
MDF 1 cycle	0.08	424
MDF 2 cycles	0.05	443

**Table A4-4: Summary of strength coefficient and strain hardening exponent of Al-12.1Si alloys in various conditions**

<b>Processing condition</b>	<b>Strain hardening exponent (n)</b>	<b>Strength coefficient (K), MPa</b>
As-cast	0.14	257
Solutionized	0.16	260
MDF 1 cycle	0.081	305
MDF 2 cycle	0.062	337
MDF 3 cycles	0.061	347

**Table A4-5: Summary of scratch depth of Al-7.3Si alloys in various conditions**

<b>Processing condition</b>	<b>Scratch depth(<math>\mu\text{m}</math>) at load of 3 N</b>	<b>Scratch depth(<math>\mu\text{m}</math>) at load of 9 N</b>	<b>Scratch depth(<math>\mu\text{m}</math>) at load of 15 N</b>
As-cast	4.9	51.5	99.5
Solutionized	3.1	24.3	50.1
MDF 1 cycle	3.3	22.9	42.4
MDF 2 cycle	0.1	9.8	26.9

**Table A4-6: Summary of scratch depth of Al-12.1Si alloys in various conditions**

<b>Processing condition</b>	<b>Scratch depth(<math>\mu\text{m}</math>) at load of 3 N</b>	<b>Scratch depth(<math>\mu\text{m}</math>) at load of 9 N</b>	<b>Scratch depth(<math>\mu\text{m}</math>) at load of 15 N</b>
As-cast	5.4	40.2	86.6
Solutionized	4.1	36.5	74.5
MDF 1 cycle	3.1	37.7	64.7
MDF 2 cycle	2.2	23.1	39.8
MDF 3 cycles	2.2	20.206	36.1

**Table A4-7: Summary of scratch traction force of Al-7.3Si alloys in various conditions**

<b>Processing condition</b>	<b>traction force (<math>\mu\text{m}</math>) at load of 3 N</b>	<b>traction force (<math>\mu\text{m}</math>) at load of 9 N</b>	<b>traction force (<math>\mu\text{m}</math>) at load of 15 N</b>
As-cast	0.78	2.54	4.89
Solutionized	1.06	2.48	4.87
MDF 1 cycle	0.89	2.59	4.82
MDF 2 cycle	1.09	2.91	5.35

**Table A4-8: Summary of scratch traction force of Al-12.1Si alloys in various conditions**

<b>Processing condition</b>	<b>traction force (<math>\mu\text{m}</math>) at load of 3 N</b>	<b>traction force (<math>\mu\text{m}</math>) at load of 9 N</b>	<b>traction force (<math>\mu\text{m}</math>) at load of 15 N</b>
As-cast	1.22	2.97	5.42
Solutionized	1.10	3.06	5.03
MDF 1 cycle	1.09	2.99	5.32
MDF 2 cycle	0.92	2.69	5.45
MDF 3 cycle	0.90	2.65	5.47

**Table A4-9: Summary of wear mass loss of Al-7.3Si alloys in various conditions**

<b>Processing condition</b>	<b>Condition-1 Load-2kg Speed-0.7m/s</b>	<b>Condition-2 Load-4kg Speed-0.7m/s</b>	<b>Condition-3 Load-2kg Speed-2.2m/s</b>	<b>Condition-4 Load-2kg Speed-2.2m/s</b>
As-cast	22.84 mg	29.68 mg	18.85	23.93
MDF 1 cycle	12.95 mg	17.15 mg	8.23	13.91
MDF 2 cycle	6.25 mg	10.26 mg	4.85	7.65

**Table A4-10: Summary of wear mass loss of Al-12.1Si alloys in various conditions**

<b>Processing condition</b>	<b>Condition-1 Load-2kg Speed-0.7m/s</b>	<b>Condition-1 Load-4kg Speed-0.7m/s</b>	<b>Condition-1 Load-2kg Speed-2.2m/s</b>	<b>Condition-1 Load-2kg Speed-2.2m/s</b>
As-cast	20.48	26.98	16.22	22.14
MDF 1 cycle	12.82	17.28	9.22	14.26
MDF 2 cycle	9.12	14.17	7.26	10.38
MDF 3 cycle	7.75	12.38	5.95	8.55

**Table A4-11: Summary of COF of Al-7.3Si alloys in various conditions**

<b>Processing condition</b>	<b>Condition-1 Load-2kg Speed-0.7m/s</b>	<b>Condition-2 Load-4kg Speed-0.7m/s</b>	<b>Condition-3 Load-2kg Speed-2.2m/s</b>	<b>Condition-4 Load-2kg Speed-2.2m/s</b>
As-cast	0.41	0.56	0.32	0.34
MDF 1 cycle	0.36	0.38	0.3	0.33
MDF 2 cycle	0.33	0.37	0.29	0.31

**Table A4-12: Summary of COF of Al-12.1Si alloys in various conditions**

<b>Processing condition</b>	<b>Condition-1 Load-2kg Speed-0.7m/s</b>	<b>Condition-2 Load-4kg Speed-0.7m/s</b>	<b>Condition-3 Load-2kg Speed-2.2m/s</b>	<b>Condition-4 Load-2kg Speed-2.2m/s</b>
As-cast	0.43	0.44	0.35	0.38
MDF 1 cycle	0.38	0.41	0.34	0.354
MDF 2 cycle	0.35	0.36	0.34	0.351
MDF 3 cycle	0.32	0.36	0.31	0.34



## BIO-DATA

**Name:** Kumara B

**Father's Name:** K Babu

**Mother's Name:** Meena

**Date of Birth:** 01-08-1983

**Nationality:** Indian

**Marital Status:** Married

### Address:

Koddyadka House Mithabile post

Puthige village, Mangalore -574226

Mobile Number: 8971631644

E-mail id: kumarnie619@gmail.com

<b>Educational Qualification: Course</b>	<b>Institution</b>	<b>University</b>	<b>Batch</b>
Ph. D. (Metallurgical and Materials Engineering)	National Institute of Technology Karnataka, Surathkal	NITK	2023
M. Tech. (Production Engineering)	The National Institute of Engineering-Mysore	VTU	2014
B. E. (Mechanical Engineering)	The National Institute of Engineering-Mysore	VTU	2008
Diploma (Automobile Engineering)	Karnataka Polytechnic Mangalore	Board of Technical Examination	<b>2003</b>